

**Microwave Radiative Transfer Calculations  
with Multiple Scattering Effects  
by Nonspherical Hydrometeors**

**Dissertation**

zur

Erlangung des Doktorgrades (Dr. rer. nat.)

der

Mathematisch-Naturwissenschaftlichen Fakultät

der

Rheinischen Friedrich-Wilhelms-Universität Bonn

vorgelegt von

**Harald Czekala**

aus

Hamburg

Bonn 1999

Angefertigt mit Genehmigung der Mathematisch-Naturwissenschaftlichen  
Fakultät der Rheinischen Friedrich-Wilhelms-Universität Bonn

1. Referent: Prof. Dr. Clemens Simmer
2. Referent: Prof. Dr. Klaus Künzi

Tag der Promotion:

# Contents

<b>Table of Contents</b>	<b>i</b>
<b>List of Figures</b>	<b>iii</b>
<b>List of Tables</b>	<b>ix</b>
<b>1 Introduction</b>	<b>1</b>
1.1 Forward modeling and retrieval . . . . .	2
1.2 Current problems . . . . .	4
1.3 Focus of the study . . . . .	6
1.3.1 Model development . . . . .	7
1.3.2 Model calculations . . . . .	7
1.3.3 Model validation . . . . .	8
<b>2 Radiative Transfer Theory</b>	<b>9</b>
2.1 Formulation of the problem . . . . .	9
2.2 Definition of terminology . . . . .	10
2.3 Polarization . . . . .	12
2.3.1 Wave formalism . . . . .	12
2.3.2 Intensity formalism . . . . .	13
2.3.3 Transformation of Stokes vectors . . . . .	14
2.3.4 Global coordinates . . . . .	14
2.4 Vector radiative transfer equation . . . . .	16
2.4.1 The three-dimensional problem . . . . .	16
2.4.2 One-dimensional solution . . . . .	17
2.5 Interaction parameters . . . . .	18
2.5.1 Gas absorption . . . . .	18
2.5.2 Single scattering by hydrometeors . . . . .	21
2.6 Boundary conditions . . . . .	24
<b>3 Numerical Solution of Radiative Transfer</b>	<b>29</b>
3.1 Definition of environment . . . . .	30
3.1.1 Discretization grid . . . . .	30
3.1.2 Surface definition . . . . .	30
3.1.3 Vertical profiles . . . . .	31
3.1.4 Drop size distributions . . . . .	31

3.1.5	Hydrometeor shapes . . . . .	32
3.2	Calculation of interaction parameters . . . . .	35
3.2.1	Refractive index of water . . . . .	35
3.2.2	Gas absorption . . . . .	36
3.2.3	Single scattering calculations . . . . .	36
3.2.4	Scattering database . . . . .	37
3.3	Radiative transfer . . . . .	39
3.3.1	Solving method . . . . .	39
3.3.2	Examples of convergence . . . . .	40
<b>4</b>	<b>Effects of Nonspherical Particles</b>	<b>43</b>
4.1	Oblate spheroid shape . . . . .	43
4.2	Angular dependence . . . . .	44
4.3	Rain rate dependence . . . . .	48
4.4	Sensitivity to drop size . . . . .	50
4.5	Comparison of different shape approximations . . . . .	53
4.5.1	Intensity results . . . . .	53
4.5.2	Polarization results . . . . .	56
<b>5</b>	<b>Validation</b>	<b>61</b>
5.1	Measurements . . . . .	61
5.2	Data processing . . . . .	63
5.3	Comparison with the model . . . . .	65
5.4	Conclusions . . . . .	68
<b>6</b>	<b>Implications for Remote Sensing of Precipitation</b>	<b>69</b>
6.1	Ground-based observations . . . . .	69
6.1.1	Sensitivity to cloud and rain particles . . . . .	70
6.1.2	Proposed method . . . . .	72
6.2	Observation of upwelling radiation . . . . .	74
6.2.1	Current methods . . . . .	75
6.2.2	Polarization as an additional atmospheric signal . . . . .	76
6.2.3	Application to three-dimensional problems . . . . .	80
<b>7</b>	<b>Summary</b>	<b>81</b>
	<b>Acknowledgments</b>	<b>83</b>
	<b>Bibliography</b>	<b>85</b>

# List of Figures

1.1	<i>Contribution of atmosphere and boundary to the total signal received by the satellite. Emission from all parts of the atmosphere and the contributions from the upper and lower boundaries propagate through the atmosphere. This radiation will be affected by absorption, reflection and scattering prior to observation by a spaceborne or ground-based sensor system. . . . .</i>	5
2.1	<i>Definition of the specific intensity. . . . .</i>	11
2.2	<i>Illustration of an elliptically polarized electromagnetic wave. . . . .</i>	12
2.3	<i>Directions of incoming and outgoing radiation with notation of angles. . .</i>	15
2.4	<i>One-dimensional coordinate system for radiative transfer. . . . .</i>	18
2.5	<i>Spectrum of microwave optical thickness produced by atmospheric gases for the atmosphere with US-standard atmosphere conditions at nadir direction.</i>	19
2.6	<i>Spectrum of microwave transmission by the gaseous atmosphere with US-standard conditions at nadir direction. . . . .</i>	20
2.7	<i>Spectrum of microwave emission by the gaseous atmosphere with US-standard conditions at nadir direction: Upwelling (solid line) and downwelling (dash-dotted line) radiation at top of atmosphere and bottom of atmosphere. Vertical lines show some of the observing frequencies of ADEOS-II (10.7 GHz), SSM/I (22.235, 37 and 85.5 GHz) and AMSU-B (150 and 183 GHz). . .</i>	21
2.8	<i>Spectrum of downwelling microwave radiation emitted by the gaseous atmosphere with US-standard conditions at nadir direction: The height of observation is varied, the highest brightness temperatures correspond to observations from surface. Higher observation altitudes result in lower brightness temperatures and a more pronounced line spectrum of trace gases. (The uppermost line corresponds to observation at the sea level, the lowest line shows the obserbation at 8 km altitude, the line in between is for 4 km observing height. . . . .</i>	22
2.9	<i>Elements R1 (left, solid), R2 (left, dashed), R3 (right, solid) and R4 (right, dashed) of the reflection matrix eq. (2.45) for different refractive indices: (a) <math>m = 5 + 2i</math>, (b) higher absorption: <math>m = 5 + 3i</math>, (c) smaller real part of refractive index: <math>m = 1.7 + 2i</math>. The Brewster angle close to 80 degree is visible in the vertical polarisation (R1) and in determinant of the <math>2 \times 2</math> sub-matrix of R3 and R4 as well. . . . .</i>	26
3.1	<i>Cross sections of falling drops (solid line) according to Chuang and Beard (1990). Equivalent volume spheres (dashed line) and spheroids (dotted line) are given for reasons of comparison. . . . .</i>	33

3.2	<i>Aspect ratio of falling drops: The modeled equilibrium shapes from Chuang and Beard (1990) (solid line), the equilibrium dropshapes measured by Andsager et al. (1998) (dotted line) and the averaged values for oscillating drops (dashed line, only valid up to 4.1 mm diameter, from Andsager et al.(1998)). . . . .</i>	34
3.3	<i>Real part and imaginary part of refractive index. . . . .</i>	35
3.4	<i>Hierarchical structure of the database information source tree. Each node is represented by a filled dot, the sub-nodes ("childs") of each node are connected to the above node ("parent") by lines. The tree itself is ordered in the meaning that every list of sub-nodes below one node is ordered. . .</i>	38
3.5	<i>Convergence of brightness temperature (at a zenith angle of 54 degrees) with order of scattering (iteration number). . . . .</i>	41
3.6	<i>Convergence of polarization difference with iteration number (at a zenith angle of 54 degrees). . . . .</i>	41
3.7	<i>Convergence of polarization difference with iteration number for downwelling radiation at 97 degrees zenith angle (7 degrees elevation angle). . .</i>	41
3.8	<i>Convergence of polarization difference with iteration number for downwelling radiation at 111 degrees zenith angle (21 degrees elevation angle). . .</i>	41
4.1	<i>Total intensity versus zenith angle of propagation at different frequencies for 20 mm/h rain rate for different situations: (a) case B, emissivity is set to <math>\epsilon = 1.0</math>, (b) case BD, <math>\epsilon = 1.0</math>, (c) case B, but with polarizing sea surface below. The upwelling radiation (angles 0 to 90 degree) is taken at the top of the atmosphere, downwelling radiation (90 to 180 degree propagation direction) at the bottom of the atmosphere. . . . .</i>	45
4.2	<i>Brightness temperature for 37 GHz (case BD, <math>\epsilon = 1.0</math>) versus zenith angle and vertical position. The rain layer with 20 mm/h rain rate reaches up to 2 km height, the ice layer is placed between 2 km and 3 km. . . . .</i>	46
4.3	<i>Polarization difference (corresponding to Fig. 4.2). . . . .</i>	46
4.4	<i>Angular dependence of PD for case A (upper left), B (upper right), AC (lower left) and BD (lower right). . . . .</i>	47
4.5	<i>Change in PD when using oblate shape for both phases instead of spherical rain and oblate ice particles (case BD minus AD). . . . .</i>	48
4.6	<i>Change in PD (cases BD minus AC) when using oblate shapes for both phases instead of spheres for both. The rain rate is set to 20 mm/h (as in all previous figures), but the surface emissivity is set to Fresnel reflection. . . . .</i>	48
4.7	<i>PD versus rain rate for different frequencies (case B, rain layer with oblate spheroids). . . . .</i>	49
4.8	<i>Change in PD versus rain rate when using oblate raindrops and ice particles instead of spheres for both (case BD minus AC). . . . .</i>	49
4.9	<i>PD versus rain rate over water surface. Oblate raindrops and oblate ice particles are used (case BD). . . . .</i>	50
4.10	<i>Change in PD versus rain rate when using oblate raindrops and ice particles instead of spheres for both (case BD minus AC, similar to Fig. 4.8, but with sea surface emission). . . . .</i>	50

4.11	<i>Change in brightness temperatures (using spheroid particles and a zenith angle of 56 degrees) as a function of maximum radius in the DSD integration (for details see text).</i>	51
4.12	<i>Difference of brightness temperatures obtained by different drop shapes (spheroids minus spheres) as a function of maximum radius in the DSD integration (using a zenith angle of 56 degrees).</i>	51
4.13	<i>Change in polarization differences (using spheroid particles) as a function of maximum radius in the DSD integration (using a zenith angle of 56 degrees).</i>	51
4.14	<i>Difference of polarization differences obtained by different drop shapes (spheroids minus spheres) as a function of maximum radius in the DSD integration (using a zenith angle of 56 degrees).</i>	51
4.15	<i>Scattering, absorption, extinction efficiencies (dashed, dotted, and solid) and asymmetry parameter for DSD at 85 GHz.</i>	52
4.16	<i>Scattering, absorption, extinction efficiencies (dashed, dotted, and solid) and asymmetry parameter for DSD at 19 GHz.</i>	52
4.17	<i>Brightness temperature vs zenith angle of propagation for six frequencies at 25 mm/h rain rate (no ice particles) and three different surface conditions: (a) blackbody emission (<math>\epsilon = 1.0</math>), (b) sea surface (Fresnel), (c) lowered emissivity (<math>\epsilon = 0.5</math>, Lambertian surface).</i>	54
4.18	<i>Brightness temperature differences vs zenith angle (rain only and blackbody emission at the surface): (a) Spheroids minus Spheres, (b) Chebyshev drops minus spheres, (c) Chebyshev drops minus spheroids.</i>	54
4.19	<i>All settings as in Fig. 4.18, but with the ice particle layer only (no rain).</i>	55
4.20	<i>All settings as in Fig. 4.18, but with the ice particle layer additional to the rain layer (both layers present).</i>	55
4.21	<i>All settings as in Fig. 4.20 (both layers, rain and ice), but with sea surface conditions at the lower boundary.</i>	56
4.22	<i>PD vs zenith angle of propagation for six frequencies at 25 mm/h rain rate (no ice particles) and three different surface conditions: (a) blackbody emission (<math>\epsilon = 1.0</math>), (b) sea surface (Fresnel), (c) lowered emissivity (<math>\epsilon = 0.5</math>). Note that the large PD values in (b) for a nearly transparent atmosphere are not connected to the hydrometeor shape, so that the results have been clipped.</i>	57
4.23	<i>Difference of PD (Chebyshev drops minus spheres) vs zenith angle of propagation for three different surface conditions: (a) blackbody emission (<math>\epsilon = 1.0</math>), (b) sea surface (Fresnel), (c) lowered emissivity (<math>\epsilon = 0.5</math>).</i>	57
4.24	<i>PD differences vs zenith angle (rain only and blackbody emission at the surface): (a) Spheroids minus Spheres, (b) Chebyshev drops minus spheres, (c) Chebyshev drops minus spheroids.</i>	57
4.25	<i>All settings as in Fig. 4.24, but with the ice particle layer only (no rain).</i>	58
4.26	<i>All settings as in Fig. 4.20 (both layers, rain and ice), but with sea surface conditions at the lower boundary.</i>	58

5.1	<i>The 19 GHz radiometer ontop of the roof: The antenna is aligned to southward direction with an elevation of 30 degree. On the right hand side the meteorological sensors can be seen. . . . .</i>	62
5.2	<i>Time series of TB, PD and RR at July 12, 1999. . . . .</i>	64
5.3	<i>Two examples correlation between TB and RR as a function of time shift (solid line). Example (a) gives a clear maximum with an symmetric shape of the peak correlation. The absolute maximum of example (b) may be misleading, so the center of the peak width at a certain threshold value is used for the determination of the time lag. . . . .</i>	65
5.4	<i>Measured brightness temperature as function of surface rain rate for 60 selected days. Observations were made at 30 degrees elevation and 19 GHz frequency. The standard deviation of the averaged value is indicated with error bars. . . . .</i>	66
5.5	<i>Measured polarization difference as function of surface rain rate (same observations as in Fig. 5.4). . . . .</i>	66
5.6	<i>Measured polarization difference as function of brightness temperature (same observations as in Fig. 5.4). . . . .</i>	66
5.7	<i>Measured polarization difference as function of brightness temperature (same observations as in Fig. 5.6, but with histogram function with respect to TB instead of RR). . . . .</i>	66
5.8	<i>Modeled TB versus rain rate. The size of the plot symbols indicates the rain layer height (from 1 to 3 km). The colour gives the atmospheric temperature at lowest level from 0 (dark green) to 25 degree centigrade (red). . . . .</i>	67
5.9	<i>Modeled PD versus rain rate. Squares (upper branch) indicate spherical particles, diamonds (lower branches) indicate oblate raindrops. . . . .</i>	67
5.10	<i>Modeled PD versus TB. The variation in PD for nonspherical particles due to rain layer height is cancelled out, the remaining difference is simply the variability in atmospheric temperature and a more pronounced saturation due to increased optical thickness with warmer atmospheres. . . . .</i>	68
6.1	<i>Brightness temperature versus total LWP of cloud and rain mixtures. The symbol size indicates the rain LWP fraction of the total LWP. . . . .</i>	70
6.2	<i>Brightness temperature versus LWP caused by rain water. At high rain rates the sensitivity to cloud LWP is decreased. . . . .</i>	71
6.3	<i>PD versus total LWP for different fractions of rain LWP: With increasing rain water fractions the PD signal is increased. . . . .</i>	71
6.4	<i>PD versus rain LWP: At low rain amounts the PD is determined by the rain LWP with no impact from the cloud LWP. At higher rain fractions the saturation caused by the rain liquid water is dominant and the additional saturation by cloud liquid water leads to a variation of PD with cloud LWP. . . . .</i>	72
6.5	<i>Sensitivity of PD and TB to rain LWP, cloud LWP and total LWP. Along solid lines the total LWP is constant, dashed lines indicate constant rain LWP and dash-dotted lines indicate constant cloud LWP. . . . .</i>	73
6.6	<i>PD as a function of rain LWP at a fixed total LWP of 1.2 kg/m<sup>2</sup> for six different elevation angles. . . . .</i>	74



---

6.7	<i>Rain rate retrieval with six different algorithms (see text for details) for a simulated rain layer (without ice): Results obtained by using spherical raindrops are indicated by small plot symbols, oblate raindrops by large plot symbols. . . . .</i>	77
6.8	<i>Rain rate retrieval in the presence of rain and ice particles. Large symbols indicate nonspherical particles (Type-I), small symbols indicate spherical shape. . . . .</i>	77
6.9	<i>Rain rate retrieval in the presence of rain and ice particles. Large symbols indicate nonspherical particles (Type-II), small symbols indicate spherical shape. . . . .</i>	78
6.10	<i>Rain rate retrieval in the presence of rain and ice particles. Large symbols indicate nonspherical particles (Type-III), small symbols indicate spherical shape. . . . .</i>	78
6.11	<i>Polarization difference versus rain rate over a calm water surface for the rain layer without ice (corresponding to the results of Fig. 6.7). . . . .</i>	79
6.12	<i>Polarization difference versus rain rate over a calm water surface for the rain layer and Type-I ice particles (corresponding to the results of Fig. 6.8). . . . .</i>	79
6.13	<i>Polarization difference versus rain rate over a calm water surface for the rain layer and Type-II ice particles (corresponding to the results of Fig. 6.9). . . . .</i>	80
6.14	<i>Polarization difference versus rain rate over a calm water surface for the rain layer and Type-III ice particles (corresponding to the results of Fig. 6.10). . . . .</i>	80



# List of Tables

3.1	<i>Coefficients for shape definition . . . . .</i>	33
4.1	<i>Definition of test cases. All cases include a water cloud between 1 and 3 km height with an altitude constant LWC of <math>0.5 \text{ kg/m}^3</math> and a MGD particle size spectrum with a modal radius of <math>5.5 \mu\text{m}</math>. The raining layer is positioned between 0 and 2 km height, the ice particle layer starts at 2 km and ends at 3 km. . . . .</i>	44
5.1	<i>Temporal coverage of the data available from the 19 GHz radiometer of the DLR Oberpfaffenhofen. . . . .</i>	62
5.2	<i>Radiometer description. . . . .</i>	63
5.3	<i>Description of sensors. . . . .</i>	63



# Chapter 1

## Introduction

More than 30 years after the first microwave observations of the earth by the Soviet satellite Cosmos-243 in 1968 (*Basharinov et al.*, 1971) remote sensing of precipitation for meteorological and climatological applications is still a challenge. Technical limitations and shortcomings of sensors — ground-based, airborne and spaceborne — are one reason that prevents better results for precipitation retrieval techniques. One other reason is imperfect modeling of the relevant radiation processes. One of several simplifications is the assumption that cloud and precipitation particles can be considered to be spherical particles. In the past this approach was justified by the insufficient mathematical methods and computing capabilities, but both problems are currently overcome. The nonspherical nature of ice and snow particles is obvious but highly variable and usually unknown during the retrieval process. The shape of raindrops resembles a sphere more closely and can be reasonably described by models. Observations of convective precipitation systems (*Spencer et al.*, 1983b, 1989; *Heymsfield and Fulton*, 1994) show residual polarization differences originating from some parts of the raining area. Scattering by nonspherical ice particles was suggested to be the origin of this polarization signal. However, up to now the precise mechanism of polarizing microwave radiation by nonspherical hydrometeors is not investigated with sufficient accuracy.

Passive microwave (MW) observations of the Earth's atmosphere are widely used for the retrieval of meteorological data. A variety of sensors have been developed for remote measurements of atmospheric humidity and temperature profiles from the surface (e.g. *Crewell et al.* (1999a); *Solheim et al.* (1998)). The liquid water content is subject of ground-based and airborne retrieval methods (*Wilheit et al.*, 1977; *Rodgers et al.*, 1979; *Prabhakara et al.*, 1986; *Spencer et al.*, 1989; *Löhnert et al.*, 1999). When considering clouds and precipitation the radiation emitted by the surface and the atmosphere itself will be scattered, absorbed, and re-emitted by the hydrometeors. The microwave frequencies below 100 GHz (e.g. those used by the Special Sensor Microwave/Imager (SSM/I, *Hollinger et al.* (1987)) onboard the Defence Meteorological Satellite Program (DMSP)) have a great potential for precipitation retrieval and are widely used. On SSM/I the center frequencies are 19.35, 22.235, 37.0, and 85.5 GHz. The Scanning Multifrequency Microwave Radiometer (SMMR, which operated only for a short period in 1978 onboard the Seasat satellite and for more than eight years onboard the Nimbus-7 satellite (*Gloersen and Barath* (1977); *Wilheit and Chang* (1980); *Cavalieri et al.* (1984))) had additional

channels at 6.6 and 10.7 GHz, which are also considered in this study because they will be used on the ADEOS-II satellite (ADEOS: Advanced Environmental Observation Satellite). Those low frequencies are of high interest in remote sensing of the earth's surface (e.g. soil moisture).

Measurements at higher MW frequencies, as well as visible and infrared measurements, suffer from the effects of very high optical thickness. Therefore, such observations are only capable of obtaining information from the upper or lower boundary of the cloud and rain events, depending on the location of the sensor (airborne or ground-based).

Especially the lower MW frequencies have the capability to penetrate through the atmosphere with only little interaction with the atmosphere. Under clear-sky conditions the radiation at 6.6 GHz remains nearly unaffected by the atmosphere. Even 3 km thick layers of moderate rain rates do not produce sufficient optical thickness to prevent radiation at 19.35 GHz from propagating from the surface up to the top of the atmosphere. Thus, these frequencies gather information along the whole path through the atmosphere rather than only from a boundary between low and high optical thickness. It will be shown that especially these situations of semi-transparent atmospheres need to consider the particle shape in order to obtain correct scattering results.

## 1.1 Forward modeling and retrieval

Many algorithms have been developed for liquid water path (LWP) and rain rate (RR) retrieval since different research groups had shown the possible use of passive microwave observations for these applications (*Basharinov et al., 1971; Akvilonov et al., 1973; Wilheit et al., 1977*). The applied retrieval techniques can be divided into two major categories: empirical and physical retrievals. Empirical algorithms estimate a relation between MW measurements and the ground truth, as obtained from mostly surface-based measurements (*Grody, 1991; Ferraro and Marks, 1995; Stogryn et al., 1994; Conner and Petty, 1998; Müller, 1997*).

These methods do not need numerical modeling of the physical processes involved and therefore offer the advantage of easy implementation. However, the results of such retrieval schemes will be restricted to the situations, which are represented by the input data. The quality of the retrieval algorithm depends on the quality of the data set used for the construction of the retrieval scheme.

On the global scale the combination of statistical methods and physical retrieval algorithms might be more applicable. A radiative transfer model (RTM) can be used to perform forward calculations, leading to a transfer function connecting a set of atmospheric parameters (especially precipitation) with resulting brightness temperatures (TB). The inversion of this function, which forms the retrieval algorithm, can be obtained by a variety of different methods reaching from simple regressions (*Spencer et al., 1983a; Bauer and Schlüssel, 1993*) to optimal estimation methods (*Rodgers, 1990*). While most rain algorithms focus on the ice particle scattering signal at 85 GHz (*Adler et al., 1994*), some algorithms use all available frequencies in a multi-channel physical retrieval (*Petty, 1994*). Since these physical retrievals heavily rely on the quality of the forward calculations, large effort has to be made to assure the correct design of the RTM.

The dependence of MW radiation on surface conditions is well known for water surfaces even in the presence of rough sea surface, swell, and foam (e.g. *Schrader (1995); Liu et al. (1998)*). The basic effect can be understood as a partly reflecting Fresnel surface, leading to high amounts of linear polarization especially near the Brewster angle (which is between 65 and 84 degrees for microwave radiation, completely determined by the inverse tangent function of the refractive index). Horizontally polarized intensity ( $I_h$ ) is less emitted than vertically polarized intensity ( $I_v$ ). Aside from the total intensity ( $I_{tot} = I_v + I_h$ ), expressed as equivalent brightness temperature  $T_B$ , the polarization difference (PD) is of special interest. It is defined as  $PD = (T_{B,v} - T_{B,h})$  and reaches up to 100 K over calm water surfaces at 53° zenith angle and a frequency of 19 GHz (*Ulaby et al., 1981*). The average emissivity of water surfaces for total intensity is close to 0.5 and produces the cold signature of water areas in the MW brightness temperature observations from satellites.

In general, land surfaces show higher emissivities for both polarizations (approximately ranging from 0.7 to 1.0 in the MW spectral region) and thus less polarization than water. However, the behaviour of land surface emissivity strongly depends on soil moisture, surface roughness, surface inclination, vegetation, and the specific frequency.

Atmospheric effects on the MW radiation consist of the well understood emission and absorption process by various gas species on one hand and the emission, absorption, and scattering process by hydrometeors on the other hand. While the gas interaction is unpolarized with no angular variation, the effects of hydrometeors exhibit a strong dependence on direction and polarization of radiation. Furthermore, they have an impact on the angular pattern of the intensity and the state of polarization by themselves (*Liu and Simmer, 1996; Czekala and Simmer, 1998; Czekala, 1998*).

Since rain retrieval on the global scale often involves satellites, this study will focus on some commonly used satellite frequencies. Because low frequency radiation (e.g., below 37 GHz) tends to penetrate clouds and even moderate rain, it has proved to be a suitable indicator for the water amount along the line of sight. These frequencies are mostly used for emission based retrieval techniques over radiatively cold ocean surfaces: The emission of liquid water tends to screen the cold background with higher TB values. The amount of emitted radiation is quite directly linked to the liquid water path (LWP).

With the 85 GHz channels of the Special Sensor Microwave/Imager (SSM/I), onboard the DMSP satellites since 1987, a considerably larger frequency is supplied for the remote sensing of rain (*Prabhakara et al., 1992; Adler et al., 1993; Bauer and Grody, 1995*). Due to the larger size parameters (particle size compared to wavelength) the absorption by liquid water is much larger than in the low frequency range and saturates the emission signal already at the onset of rainfall. A retrieval of rain rate (RR) is still possible through indirect effects: Large RR are often associated with a significant ice mass above the raining cloud (Bergeron-Findeisen theory). These ice particles have an absorption coefficient two orders of magnitude lower than water and act like nearly non-absorbing scatterers. Their size, which is comparable to the wavelength at 85 GHz, makes scattering very efficient. The brightness temperature depression caused by the ice scattering above rain layers is used to derive the corresponding rain rate. Such methods require accurate modeling of the scattering process, which is also affected by shape and orientation of the hydrometeors. Despite of the well known fact that the shape of hydrometeors can

be highly nonspherical the interaction parameters are mostly calculated according to the Lorenz-Mie theory, which assumes spherical shape. This is an appropriate approximation in case of liquid non-precipitating cloud droplets. Solid hydrometeors in ice clouds significantly differ from spherical shape but are small enough to justify the application of the Rayleigh approximation for all frequencies under consideration: The size parameter  $\chi = 2\pi r/\lambda$  (with  $r$  a typical particle dimension and  $\lambda$  the wavelength) and the real part  $n$  of the refractive index together obey the relations  $\chi \ll 1$  and  $n\chi \ll 1$ , respectively (*van de Hulst*, 1981). In the case of Rayleigh scattering the shape is of no importance.

Precipitating hydrometeors show significant deviation from spherical geometry, revealing complex (and mostly oblate) shapes that have been both modeled and measured (*Pruppacher and Beard*, 1970; *Pruppacher and Pitter*, 1971; *Chuang and Beard*, 1990).

While some effort has been made to use nonspherical ice particles the effect of the liquid phase has mostly been neglected. The attenuation of radio waves by realistically shaped raindrops had been considered by *Oguchi* (1960, 1964) more than 30 years ago and later by *Asano and Yamamoto* (1975). The full nonspherical scattering solution, restricted to ice particles with approximated scattering properties, were carried out by *Wu and Weinman* (1984). Recently, there has been a growing number of microwave radiative transfer models exactly taking nonspherical particles into account. However, they still focus either on randomly orientated particles (*Haferman et al.*, 1997) or on the ice particles above rain layers and cirrus particles at high frequencies such as 220 GHz and above (*Evans and Stephens*, 1995a; *Evans et al.*, 1998). A recent review of modeling efforts in the microwave region (nonspherical and three-dimensional) can be found in *Haferman* (1999).

Most algorithms use only the brightness temperature depression due to scattering and the depolarizing effects of hydrometeors on the polarization which originates from the sea surface. It will be shown that both, ice particles and also rain, produce a significant amount of polarization that will lead to different polarization signatures above raining atmospheres. This is valid for highly polarizing surfaces as well as for nearly non polarizing surfaces.

As already described, the retrieval scheme that links the observed intensity and polarization to physical parameters (such as temperature, humidity, rain rate, path integrated water or ice mass etc.) is often set up by utilization of forward calculations. Numerical models are used to compute the MW radiation below, atop, and sometimes also within a well defined atmosphere. The inversion of such calculations gives the retrieval algorithm. Obviously, the quality of the retrieval algorithm is directly connected with the quality of the forward calculations.

## 1.2 Current problems

Although there have been many improvements of forward modeling attempts over the last two decades, there still exist a number of problems which need to be solved in order to gain better numerical results. From the European Union a COST<sup>1</sup> action (COST-712:

---

<sup>1</sup>COST: European Cooperation in the Field of Scientific and Technical Research, see also: <http://www.cordis.lu/cost/home.html>, <http://www.kp.dlr.de/COST/cost.html>



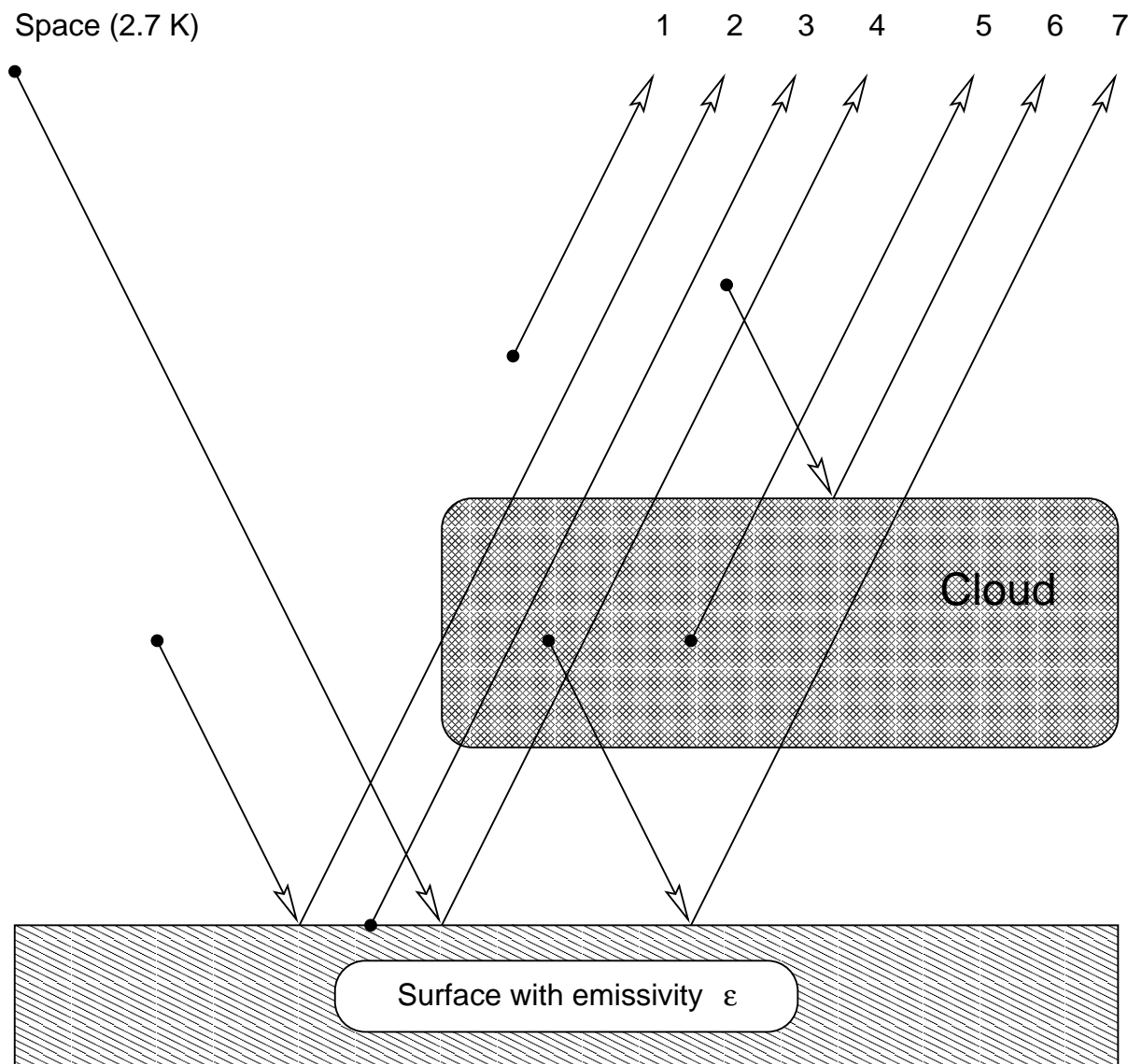


Figure 1.1: *Contribution of atmosphere and boundary to the total signal received by the satellite. Emission from all parts of the atmosphere and the contributions from the upper and lower boundaries propagate through the atmosphere. This radiation will be affected by absorption, reflection and scattering prior to observation by a spaceborne or ground-based sensor system.*

*Microwave Radiometry*) was implemented to identify and address these problems. The subgroup 1 of COST-712 is dedicated to the three major components in the process of forward modeling:

- gaseous atmosphere (absorption and emission)  
(*Bauer et al., 1999*),
- hydrometeors (absorption, emission and scattering)  
(*Czekala et al., 1999a*),

- surface (absorption, emission and reflection).

Detailed reports on recent efforts in measurements and modeling of surface properties can be found in *Mätzler (1999)*. The mixing of the effects of these three components on the total signal observed by passive microwave radiometry is illustrated in Fig. 1.1. Thermal radiation is emitted by the atmosphere (gaseous atmosphere as well as hydrometeor constituents) and the boundaries of the atmosphere (outer space with 2.7 K equivalent temperature and the surface below the earth's atmosphere). After emission the radiation may interact either with the surface or with the atmosphere. The latter results in absorption or scattering. Multiple scattering of radiation (not shown in Fig. atmos.contrib) is likely to occur when hydrometeors are present in form of clouds or precipitation.

While the influence of certain surface conditions (at least for the sea surface) and the gaseous atmosphere on the radiation is quite well known and can be modeled with sufficient accuracy, the interaction with hydrometeors is still a problem. The MW radiation within clouds or precipitation is affected by the temperature (determining the refractive index for a certain frequency), phase, size distribution, and shape of the hydrometeors. While some parameters cannot be modeled with desirable accuracy due to the lack of knowledge of their behaviour in nature (e.g. the variability in time and space of the size distribution of rain is still subject of ongoing research), other parameters rise practical problems in the formulation of the mathematical and numerical model that prevent their exact treatment.

Trace gas absorption, which takes place mostly above 100 GHz, is still not completely known and tabulated for the use within radiative transfer models. The same is true for the so-called continuum absorption by water vapor and nitrogen at all frequencies regardless of resonance lines within the spectrum. This process is identified as collision induced absorption (CIA): Colliding molecules form dimers which have a completely different resonance spectrum than the single molecules before and after the collision process.

Surface modeling research efforts concentrate on snow and ice surfaces and land surfaces (combination of soil and vegetation canopy). Since the emission and reflection characteristics of these surface types serve as lower boundary conditions for airborne or spaceborne measurements, they have to be known with high accuracy in order to obtain good retrieval results.

### 1.3 Focus of the study

The subject of this study is the detailed and accurate radiative transfer modeling of nonspherical hydrometeors. The comparison of the results with calculations based on the assumption of spherical hydrometeor shape enables the assessment of the effects introduced by shape and orientation of the hydrometeors.

Upon the knowledge of the radiative transfer mechanisms in the presence of nonspherical particles the possible error of retrieval schemes that are based on less accurate model calculations will be estimated. A new method for the rain and cloud water retrieval from ground-based measurements is proposed. If the information content of the upwelling radiation due to interaction with the nonspherical hydrometeors is sufficient new algorithms

for satellite remote sensing of hydrometeors need to be developed. Furthermore, the analysis of the obtained radiative transfer results offers further insight into the radiative transfer mechanisms and the origin of polarization induced by the atmosphere.

### 1.3.1 Model development

The changes in the radiative transfer equation when switching from spherical to non-spherical particles with a fixed orientation will be outlined in chapter 2. Based on this theory of vector radiative transfer, chapter 3 will present the modification of an existing one-dimensional radiative transfer model (MWMOD, *Simmer*, 1994) which uses Mie scattering phase functions to a fully polarized model capable of handling nonspherical hydrometeors with non-random orientation. An extended boundary condition T-Matrix code (*Mishchenko and Travis*, 1994; *Mishchenko et al.*, 1996a,b) for scattering on rotationally symmetric ellipsoids is implemented to replace the Mie scattering routines.

### 1.3.2 Model calculations

The differences in the calculated brightness temperatures for a variety of rain rates and the key finding that low frequencies (6 to 22 GHz) are most sensitive to the nonsphericity of liquid raindrops are reported in *Czekala and Simmer* (1998) and *Czekala et al.* (1998) and summarized in chapter 4.

The impact of the precise shape of hydrometeors is investigated by introducing the Discretized Mie Formalism (*Rother and Schmidt*, 1997; *Rother*, 1998) into the radiative transfer model (*Czekala et al.*, 1999b). While the approximation of liquid drops by rotational symmetric ellipsoids seems to be sufficient, the precise knowledge of the shape of ice particles is important for radiative transfer modeling.

At the Deutsches Zentrum für Luft- und Raumfahrt (DLR) in Oberpfaffenhofen studies were performed (in parallel to the presented work) that focussed on the attenuation of satellite transmission links by rain. Downwelling microwave radiation was modeled and compared with measurements (*Hornbostel and Schroth*, 1995; *Hornbostel et al.*, 1995). For the shapes of rain drops oriented oblate spheroids were used. The results were used for the determination of propagation parameters for the satellite communication link.

In this study a detailed comparison of the model results for spherical and nonspherical particles including ice particles above the rain layer will be given. The origin and variability of the polarization signal due to nonspherical particle shape will be thoroughly discussed in this chapter.

The possible effects of oblate ice particles on the MASTER microwave limb sounding experiment at frequencies between 200 and 500 GHz are investigated in *Reburn et al.* (1998) and *Czekala* (1998). Although the horizontal viewing geometry cannot be calculated with a one-dimensional model the discussion of the results obtained infinitely close to the horizontal clearly shows the main effects that are to be expected and reveals the problems that arise from the tangent viewing geometry.

### 1.3.3 Model validation

In cooperation with the Deutsches Zentrum für Luft- und Raumfahrt (DLR) in Oberpfaffenhofen the predictions made by the numerical model will be partly validated.

Ground-based measurements from DLR Oberpfaffenhofen will be used for a comparison of the modeled results in this study. The observations presented in chapter 5 will clearly confirm the model results, which are obtained with oblate particle shape and obviously differ from the spherical assumption. Furthermore, the relevance of the model calculations for rain retrieval from different platforms will be discussed in chapter 6. The findings will be utilized to propose a new method of LWP measurements in the presence of rain by polarimetric observations (*Czekala et al., 1999c*).

## Chapter 2

# Radiative Transfer Theory

The radiative transfer equation, which will be discussed in this chapter with respect to its different forms, is a heuristically derived equation for the transport of energy within a medium (*Tsang et al.*, 1985). It may be deduced from fundamental physical concepts (such as Maxwell's equations when dealing with wave theory) in a rigorous mathematical way. However, most times it is set up as a balance equation to account for all gains and losses within the medium, depending on the characteristics of the medium. This general approach may also be applied to other transport phenomena as well, so that the same kind of differential equation is used for heat transport, mass transport, neutron fluxes, and other physical transport or propagation processes.

### 2.1 Formulation of the problem

The common part in transport (or "transfer") equations is the description of loss and gain in terms of extinction and source expressions. The extinction is split up into an actual loss portion (e.g., due to absorption) and a redistribution term caused by scattering, reflection, and resonant processes. The latter may also include excitation and re-emission or even fission processes (in nuclear physics).

In general, all processes depend on the local conditions of the medium at the position  $(x, y, z)$ , the cosines of propagation direction with the major coordinate axes  $(\gamma, \delta, \mu)$ , and the attributes (intensity, polarization, wavelength) of the propagated physical phenomenon itself. Different coordinate systems may also be applied to solve the transfer equations for a specific problem under consideration. Expressed in terms of intensity the scalar radiative transfer equation (RTE) for a three-dimensional cartesian grid and a specified wavelength reads as follows:

$$\begin{aligned} \frac{d^3 I(x, y, z, \theta, \phi)}{\frac{1}{\gamma} dx \frac{1}{\delta} dy \frac{1}{\mu} dz} = & - \sigma_e(x, y, z, \theta, \phi) I(x, y, z, \theta, \phi) \\ & + \sigma_a(x, y, z, \theta, \phi) J(x, y, z, \theta, \phi) \\ & + \int_0^{2\pi} \int_0^{\pi} P(x, y, z, \theta, \phi, \theta', \phi') I(x, y, z, \theta', \phi') \sin \theta' d\theta' d\phi' . \end{aligned} \quad (2.1)$$

The differential change of intensity  $I$  with respect to the position in space  $(x, y, z)$  is fully described by the extinction, a source function  $J$  within the medium itself (in case of thermal radiation the temperature dependent Planck function  $J = B(T(x, y, z))$ ), and the scattering source term. Extinction and scattering source functions are proportional to the present intensity  $I$  and the extinction coefficient  $\sigma_e$  or scattering phase function  $P$ , respectively. The contribution of intensity scattered into the direction  $(\theta, \phi)$  is integrated over all incoming directions  $(\theta', \phi')$ . Under the assumption of thermodynamic equilibrium the emission can be determined by the absorption coefficient  $\sigma_a$  according to Kirchhof's law and the local conditions within the medium, which is the temperature  $T$  for thermal radiation. The emission of a medium not in thermodynamic equilibrium (such as a laser) cannot be obtained in the same manner.

Note that (2.1) is given for a specific frequency  $\nu$  and therefore all properties of the medium may depend on the frequency. However, throughout this study radiative transfer equations in which the intensity directly (in contrast to the above mentioned implicit form) depends on frequency are not considered. This simplification implies that no conversion of radiation between different frequencies takes place. Energy balance of the radiation field is obtained by the thermodynamic temperature in an equilibrium state: Emission is described by Planck's function, absorbed radiation is assumed to contribute to the local temperature. Active remote sensing techniques like LIDAR (light detection and ranging) using laser beams may lead to frequency dependent radiation and require other forms of radiative transfer equations.

## 2.2 Definition of terminology

When dealing with radiation fluxes one has to consider the radiant energy (*Chandrasekhar, 1960*)

$$dE_\nu = I_\nu \cos \theta d\nu d\sigma d\omega dt \quad (2.2)$$

expressed in terms of the specific intensity  $I_\nu$  (from now on just called "the intensity"). Equation (2.2) links the radiation originating from a solid angle  $d\omega$  (see Fig. 2.1) and passing a surface  $d\sigma$  under the angle  $\vartheta$  to the direction of the outward normal  $z$  to the surface  $d\sigma$  within a time interval  $dt$  to the intensity of a monochromatic pencil beam

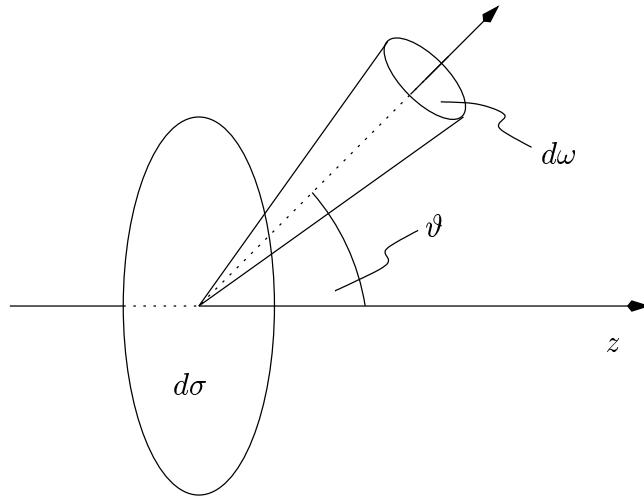
$$I_\nu \equiv I_\nu(x, y, z, \gamma, \delta, \mu, t) \quad (2.3)$$

and therefore depends on position, direction, and time. The intensity is given in units of  $\text{Wm}^{-2}\text{sr}^{-1}\text{Hz}^{-1}$ .

Keeping in mind that only thermal radiation emitted by the earth and its atmosphere will be considered we can assume a thermal equilibrium in the troposphere and lower stratosphere and neglect any time dependence: The radiation distribution will react to changes of atmospheric conditions much faster than these changes actually take place.

In the absence of effects that depend on direction the medium is said to be *isotropic* and the intensity only depends on position:

$$I_\nu \equiv I_\nu(x, y, z). \quad (2.4)$$

Figure 2.1: *Definition of the specific intensity.*

If the conditions within the atmosphere are the same at every point the scene is described as homogeneous:

$$I_\nu \equiv I_\nu(\gamma, \delta, \mu). \quad (2.5)$$

A common simplification for radiative transfer calculations assumes a plane parallel stratified atmosphere with horizontal homogeneity in each layer. This results in

$$I_\nu \equiv I_\nu(z, \theta, \phi). \quad (2.6)$$

with directions mostly represented by polar angles  $\theta$  and  $\phi$  instead of directional cosines  $(\gamma, \delta, \mu)$ . The typical one-dimensional solution is given for azimuthal symmetry, which reduces the coordinates of  $I_\nu$  to only two:

$$I_\nu \equiv I_\nu(z, \theta). \quad (2.7)$$

Since the specific intensity  $I_\nu$  itself is an uncommon variable the intensity is transformed into a brightness temperature. According to Planck's law (2.8) a blackbody (defined as idealized absorber with an emissivity of  $\epsilon = 1$ ) emits an intensity

$$B(T) \equiv \frac{2h\nu^3}{c^2} \frac{1}{\exp\left(\frac{h\nu}{k_B T}\right) - 1} \quad (2.8)$$

where  $T$  is the temperature of the blackbody,  $\nu$  the frequency,  $k_B$  Boltzmann's constant,  $h$  Planck's constant and  $c$  the speed of light. Natural media are seldomly perfect blackbodies and therefore emit less radiation. The brightness temperature  $T_B$  is defined as the temperature at which the blackbody emission  $B(T_B)$  exactly matches the measured intensity  $I$ :

$$I = B(T_B). \quad (2.9)$$

By inverting Planck's function for a measured intensity one obtains the corresponding brightness temperature

$$T_B = B^{-1}(I). \quad (2.10)$$

## 2.3 Polarization

### 2.3.1 Wave formalism

By definition, elliptically polarized electromagnetic waves are described by the time dependent electric field  $\mathbf{E}$ . The magnetic components may be derived from this information. The field components can be projected to two perpendicular vectors in the plane orthogonal to the direction of propagation (*Chandrasekhar, 1960; Liou, 1980*):

$$\hat{\mathbf{E}}(t) = \hat{\mathbf{E}}_l(t) + \hat{\mathbf{E}}_r(t) = a_l(t) \cdot \hat{\mathbf{e}}_l + a_r(t) \cdot \hat{\mathbf{e}}_r. \quad (2.11)$$

The unit vectors  $\hat{\mathbf{e}}_l$  and  $\hat{\mathbf{e}}_r$  are chosen to be orthogonal and may be arbitrary at this time. Their subscripts originate from the local frame of reference when considering a scattering process of this specific wave: The *parallel* (subscript l) and the *perpendicular* (subscript r) directions to the scattering plane are chosen for decomposition of the electromagnetic wave into orthogonal components.

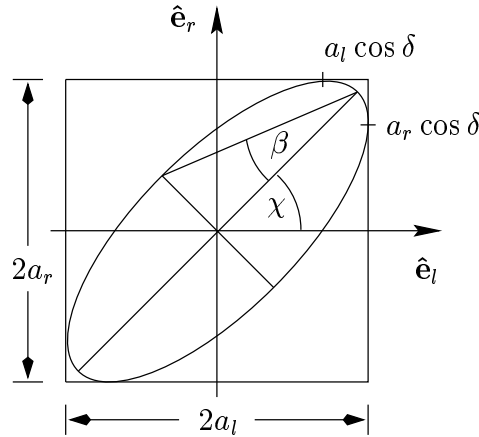


Figure 2.2: *Illustration of an elliptically polarized electromagnetic wave.*

The elliptically polarized wave with circular frequency  $\omega = 2\pi\nu = kc$  (with  $k = 2\pi/\lambda$  the wavenumber,  $c$  the speed of light and  $\nu$  the frequency) can be expressed with four constants ( $a_l, a_r, \epsilon_l, \epsilon_r$ ) for the amplitudes and phases:

$$\begin{aligned} a_l &= a_l^0 \sin(\omega t - \epsilon_l) \\ a_r &= a_r^0 \sin(\omega t - \epsilon_r). \end{aligned} \quad (2.12)$$

These equations give the real numbers that define the amplitude within the local  $(l, r)$  system (Fig. 2.2). The complex electric field components of an electromagnetic wave travelling in  $z$ -direction may also be written as

$$\begin{aligned} E_l &= a_l^0 e^{-i\delta_l} e^{-kz+i\omega t} \\ E_r &= a_r^0 e^{-i\delta_r} e^{-kz+i\omega t} \end{aligned} \quad (2.13)$$

with the phase lag  $\delta = \epsilon_l - \epsilon_r$  between both components of the wave. It is obvious that the two amplitudes and a phase difference are sufficient to describe the state of polarization for an arbitrary elliptical wave.



### 2.3.2 Intensity formalism

With the intensity given as the square of the electromagnetic field the Stokes parameters of the Stokes vector  $\bar{\mathbf{I}} = (I, Q, U, V)$  are defined (*Chandrasekhar, 1960; Liou, 1980*) by the field components:

$$\begin{aligned} I &= E_l E_l^* + E_r E_r^* \\ Q &= E_l E_l^* - E_r E_r^* \\ U &= E_l E_r^* + E_r E_l^* \\ V &= -i(E_l E_r^* - E_r E_l^*). \end{aligned} \quad (2.14)$$

The Stokes vector can be expressed with the real amplitudes ( $a_l$  and  $a_r$ ) and the phase difference  $\delta$  in the more suitable way

$$\begin{aligned} I &= a_l^2 + a_r^2 = I_l + I_r \\ Q &= a_l^2 - a_r^2 = I_l - I_r = I \cos 2\beta \cos 2\chi \\ U &= 2a_l a_r \cos \delta = I \cos 2\beta \sin 2\chi \\ V &= 2a_l a_r \sin \delta = I \sin 2\beta \end{aligned} \quad (2.15)$$

which links the Stokes parameters to the angles  $\beta$  and  $\chi$  from Fig. 2.2. The first Stokes parameter  $I$  gives the total intensity while  $Q$  indicates the degree of linear polarization. The plane of polarization (with respect to the frame of reference  $\hat{\mathbf{e}}_l$  and  $\hat{\mathbf{e}}_r$ ) is described by the parameter  $U$  according to

$$\tan 2\chi = \frac{U}{Q}, \quad (2.16)$$

while the ellipticity is given by  $V$ :

$$\sin 2\beta = \frac{V}{\sqrt{Q^2 + U^2 + V^2}}. \quad (2.17)$$

For a single wave and fully polarized light the total intensity obeys the relation

$$I^2 = Q^2 + U^2 + V^2. \quad (2.18)$$

A natural beam of light consists of a very large number of single waves so that time averages of the definition (2.15) have to be used. Equation (2.18) is no longer valid due to the mixture of unpolarized and fully polarized light within the beam. Instead, the relation

$$I^2 \geq Q^2 + U^2 + V^2. \quad (2.19)$$

still remains valid. The degree of polarization  $P$  can be defined as the ratio of polarized intensity to the total intensity:

$$P = \frac{\sqrt{Q^2 + U^2 + V^2}}{I}. \quad (2.20)$$

The state of polarization is fully described by means of intensity, which makes the Stokes vector the ideal concept for the representation of polarized electromagnetic waves

in a combination with the transfer equation (2.1). Sums and differences of Stokes vectors are justified by the fact that there does not exist a well-defined phase relation between single waves originating from thermal emission on the macroscopic scale. Incoherent addition of intensities is sufficient, phase information is neglected during this addition.

An alternative representation of the Stokes vector with some re-ordering in the first two components will be used from now on. Instead of  $I$  and  $Q$  we will use  $I_l$  and  $I_r$ , the intensities for two orthogonal directions, as a fully equivalent formulation.

### 2.3.3 Transformation of Stokes vectors

When changing the local coordinate system by rotating the  $\hat{\mathbf{e}}_l$  and  $\hat{\mathbf{e}}_r$  axes clockwise by an angle  $\phi$  the electric field components are transformed to the new system by

$$\begin{pmatrix} E'_l \\ E'_r \end{pmatrix} = \begin{pmatrix} \cos \phi & \sin \phi \\ -\sin \phi & \cos \phi \end{pmatrix} \begin{pmatrix} E_l \\ E_r \end{pmatrix}. \quad (2.21)$$

For the Stokes vector  $\bar{\mathbf{I}} = (I_l, I_r, U, V)$  the transformation matrix

$$\mathbf{L}(\phi) = \begin{pmatrix} \cos^2 \phi & \sin^2 \phi & \frac{1}{2} \sin 2\phi & 0 \\ \sin^2 \phi & \cos^2 \phi & -\frac{1}{2} \sin 2\phi & 0 \\ -\sin 2\phi & \sin 2\phi & \cos^2 \phi & 0 \\ 0 & 0 & 0 & 1 \end{pmatrix} \quad (2.22)$$

performs the corresponding linear transformation. Using the previous notation  $\bar{\mathbf{I}}' = (I, Q, U, V)$  the transformation reads

$$\mathbf{L}'(\phi) = \begin{pmatrix} 1 & 0 & 0 & 0 \\ 0 & \cos^2 \phi & \sin^2 \phi & 0 \\ 0 & \sin^2 \phi & \cos^2 \phi & 0 \\ 0 & 0 & 0 & 1 \end{pmatrix} \quad (2.23)$$

from which it is obvious that the total intensity and the ellipticity are invariant to rotation along the direction of propagation. Depending on the frame of reference the same radiation reveals different degrees of polarization. Polarization itself has a meaning together with the additional information about the directions under consideration only.

### 2.3.4 Global coordinates

Since single scattering processes are described in the natural or local coordinate system denoted by the indices  $l$  and  $r$ , while the atmospheric radiative transfer schemes uses a cartesian grid  $(x, y, z)$  for position and the spherical coordinates  $(\theta, \phi)$  for directions (see Fig. 2.3) the Stokes vectors are used in the latter coordinate system. Scattering processes change the direction of propagation and therefore require a transformation between the different notations.

The directions to which the polarization refers in the global coordinate system are given by the direction of propagation and the vertical, which is the  $z$  axis: Subscripts

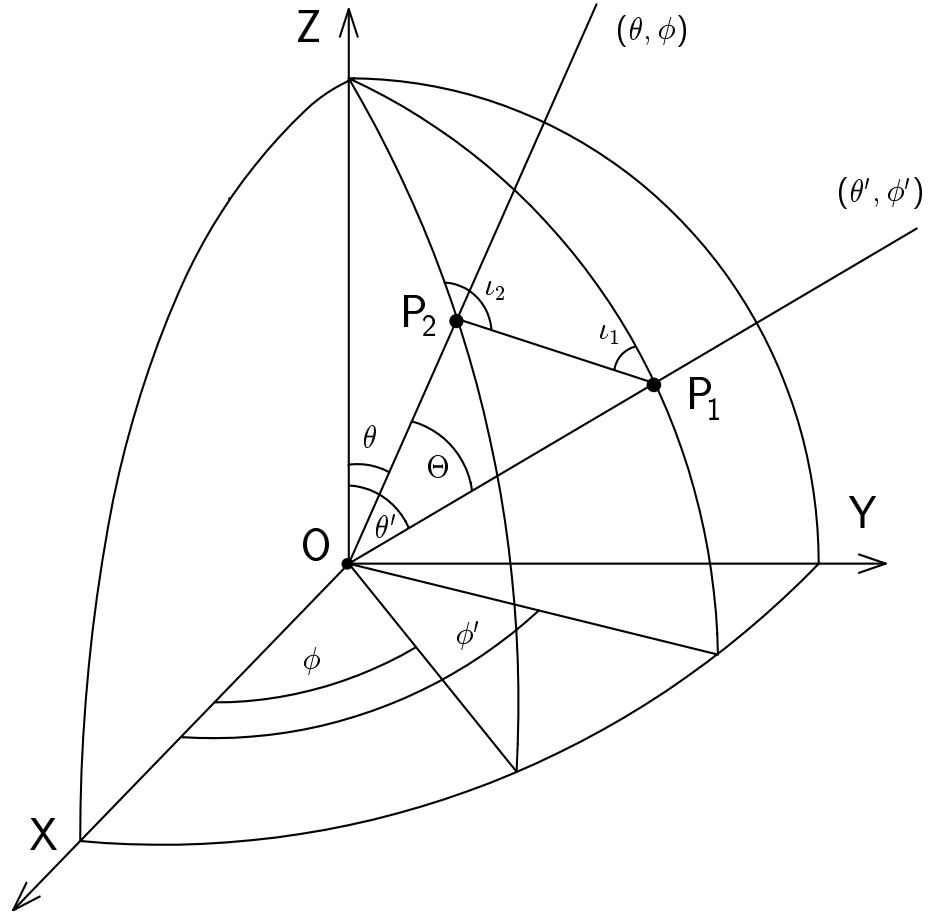


Figure 2.3: *Directions of incoming and outgoing radiation with notation of angles.*

$v$  and  $h$  are used instead of  $l$  and  $r$  when the directions within the plane of incidence (vertical) and perpendicular to this plane (horizontal) are referred to.

Assuming that the incident beam ( $P_1$  in Fig. 2.3) is scattered at the origin  $O$  to  $P_2$ , the local coordinate system is set up by the scattering plane  $P_1OP_2$ . With a scattering phase function  $\mathbf{R}(\Theta)$  that describes the scattering process with respect to the scattering angle  $\Theta$  in the local frame the Stokes vector of the incident light has to be transformed from the  $P_1OZ$  plane to the scattering plane  $P_1OP_2$  in order to apply the phase function. The angle of clockwise rotation is  $(-\iota_1)$ . After evaluating the scattering process, a transformation to the  $P_2OZ$  plane with an rotation angle  $(\pi - \iota_2)$  completes the procedure. For the scattered and reprojected result one obtains

$$\mathbf{I}(\theta, \phi) = \mathbf{L}(\pi - \iota_2)\mathbf{R}(\cos \Theta)\mathbf{L}(-\iota_1)\mathbf{I}(\theta', \phi'). \quad (2.24)$$

The phase function  $\mathbf{P}(\theta, \phi, \theta', \phi')$  is now transformed from the local system (depending only on the scattering angle) to the global system by

$$\mathbf{P}(\theta, \phi, \theta', \phi') = \mathbf{L}(\pi - \iota_2)\mathbf{R}(\cos \Theta)\mathbf{L}(-\iota_1). \quad (2.25)$$

For a set of discrete angles  $(\theta, \phi, \theta', \phi')$  we can calculate the angles  $\iota_1$  and  $\iota_2$  with  $\mu = \cos \theta$

and  $\mu' = \cos \theta'$  from

$$\cos \iota_1 = \frac{-\mu + \mu' \cos \Theta}{\pm(1 - \cos^2 \Theta)^{1/2}(1 - \mu'^2)^{1/2}} \quad (2.26)$$

and

$$\cos \iota_2 = \frac{-\mu' + \mu \cos \Theta}{\pm(1 - \cos^2 \Theta)^{1/2}(1 - \mu^2)^{1/2}}. \quad (2.27)$$

For  $\pi < (\phi - \phi') < 2\pi$  the plus sign is used in the denominator of eqs. (2.26) and (2.27), while the minus sign is used whenever  $0 < (\phi - \phi') < \pi$ . The scattering angle  $\Theta$  is linked to the global coordinates by

$$\begin{aligned} \cos \Theta &= \mu\mu' + (1 - \mu^2)^{1/2}(1 - \mu'^2)^{1/2} \cos(\phi - \phi') \\ &= \cos \theta \cos \theta' + \sin \theta \sin \theta' \cos(\phi - \phi'). \end{aligned} \quad (2.28)$$

An important fact to mention here is that regardless of how the scattering process itself may change the state of polarization there will be a change in linear polarization and the plane of polarization solely due to geometrical reprojection of the Stokes vector.

## 2.4 Vector radiative transfer equation

The radiative transfer equation for polarized light uses the Stokes vector instead of the scalar intensity. Since the components of the Stokes vector are intensities themselves the formulation is straightforward: Scalar intensities are exchanged with vectors of intensities, the parameters describing loss, gain and redistribution are modified to account for the vectorial nature of the radiation.

### 2.4.1 The three-dimensional problem

Starting with the most general equation (2.1) we obtain the three-dimensional vector radiative transfer equation (VRTE):

$$\begin{aligned} \frac{d^3 \bar{\mathbf{I}}(x, y, z, \theta, \phi)}{\frac{1}{\gamma} dx \frac{1}{\delta} dy \frac{1}{\mu} dz} &= - \bar{\sigma}_e(x, y, z, \theta, \phi) \bar{\mathbf{I}}(x, y, z, \theta, \phi) \\ &+ \bar{\sigma}_a(x, y, z, \theta, \phi) B(T(x, y, z)) \\ &+ \int_0^{2\pi} \int_0^\pi \bar{\mathbf{P}}(x, y, z, \theta, \phi, \theta', \phi') \bar{\mathbf{I}}(x, y, z, \theta', \phi') \sin \theta' d\theta' d\phi'. \end{aligned} \quad (2.29)$$

This is a set of four integro-differential equations, one for each component of the Stokes vector: The differential change for each intensity component of  $I_v, I_h, U, V$  depends on the intensity itself and an integral expression of the intensity. Scattering and extinction initiate mixing among the Stokes components. As a result the extinction of one component depends on all four elements of the actual Stokes vector; the differential equations do not decouple and have to be solved simultaneously.

Without making simplifying assumptions about the atmosphere and its constituents (e.g., one-dimensional stratified, azimuthal isotropic, random-orientation of particles,

symmetry of particles) the scattering phase matrix  $\mathbf{P}$  and the extinction matrix  $\overline{\overline{\sigma}}_e$  are non-diagonal and thus coupling all components. The emission source is a vector: four different and non-zero emission coefficients, one for each Stokes component, are multiplied by the temperature dependent Planck function for thermal emission of a blackbody.

Furthermore, the extinction, emission, and scattering matrices do not only depend on polarization but also on the specific direction. In case of scattering even two directions in space have to be considered (incoming and outgoing beam), ending up in differential equations of 7 dimensions in total: 3 dimensions for position in space and 4 for the propagation directions of incident and scattered radiation. In practice, this set of coupled equations needs to be solved with boundary conditions applied.

In the present form of the VRTE one cannot define the often used single scattering albedo  $\omega_0 = \sigma_s/\sigma_e$  as the ratio of scattering cross section to total extinction cross section since the scalar quantities do not exist. An important consequence is the absence of a well defined optical thickness and of an exponential attenuation law for the transmission of the four component Stokes vector. Attenuation along every path length  $\Delta s$  therefore cannot be calculated according to

$$I(s + \Delta s) = I(s) e^{-\sigma_e \Delta s}. \quad (2.30)$$

Instead, the differences in Stokes vector components due to the extinction matrix  $\overline{\overline{\sigma}}_e$  have to be computed at a series of sufficiently small intervals  $ds$  so that the change in intensity  $d\overline{I} = \overline{I} \overline{\overline{\sigma}}_e ds$  is still linear in the path length coordinate. This will result in much higher computational effort unless averages of extinction and absorption are defined, which could be done for spherical or randomly oriented particles only.

## 2.4.2 One-dimensional solution

Solving (2.29) is simplified Under the assumption of a plane parallel azimuthally isotropic and horizontally homogenous atmosphere (Fig. 2.4) solving (2.29) is simplified since radiation becomes a function of  $z$  and  $\theta$  and no longer depends on the full set of variables  $(x, y, z, \theta, \phi)$ .

Due to the assumed azimuthal symmetry of the problem there is no interaction between the first two components and the last two components of the Stokes vector: In case of constant radiation within azimuthal direction the phase matrix can be integrated over the range of  $2\pi$  first and then be applied to the radiation. Integration over azimuthal directions produces vanishing interaction terms between the first and last two components. As a consequence, results for total intensity and linear polarization can be derived without considering the  $U$  and  $V$  component of the Stokes vector. Equation (2.29) is therefore reduced to the vertical and horizontal polarized intensities  $I_v$  and  $I_h$ , respectively. Equation (2.31) is the simplified form of the full four component VRTE for three-dimensional applications: (Tsang et al., 1985; Haferman et al., 1997; Evans and Stephens, 1995a):

$$\frac{d\overline{\mathbf{I}}(z, \theta)}{\frac{1}{\mu} dz} = - \overline{\overline{\sigma}}_e(z, \theta) \overline{\mathbf{I}}(z, \theta) + \overline{\sigma}_a(z, \theta) B(T(z))$$

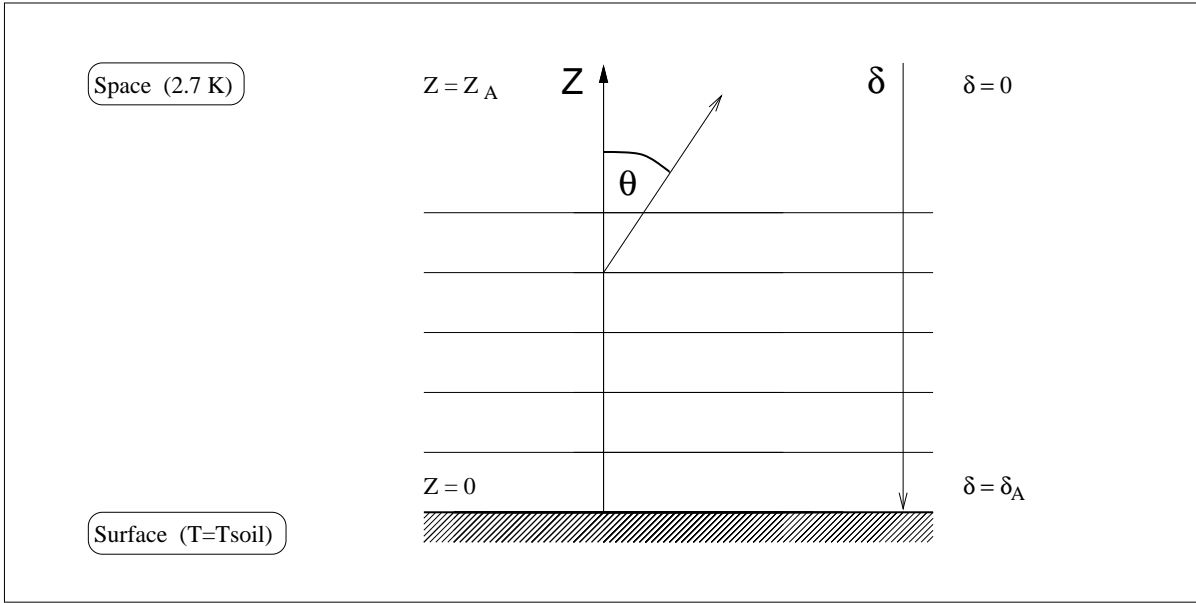


Figure 2.4: One-dimensional coordinate system for radiative transfer.

$$+ \int_0^{\pi} \overline{\mathbf{P}}(z, \theta; \theta') \overline{\mathbf{I}}(z, \theta') \sin \theta' d\theta' . \quad (2.31)$$

For this two-component equation the extinction matrix is now diagonal and thus allowing for the definition of absorption number and single scattering albedo for each polarization and the calculation of transmission according to the exponential law of Bouguer-Lambert. However, these numbers still depend on the direction and the polarization: For particles with preferred orientation the extinction (for example) will be different for vertical and horizontal polarization with an additional variation depending on the zenith angle of propagation.

## 2.5 Interaction parameters

The numerical quantities which determine how much of the radiation within the atmosphere is emitted, scattered, and absorbed are called *interaction parameters* since they describe the interaction processes of electromagnetic waves with matter. For the various constituents of the atmosphere these parameters are calculated with regard to the corresponding different physical processes that are involved. These important processes are not the same for liquid, solid, and gaseous matter. The total quantities at every location of the atmosphere then will be calculated by adding the results for all constituents.

### 2.5.1 Gas absorption

In general, gas molecules are capable of all three major interaction processes of radiation with matter: Absorption, emission, and scattering. However, due to the small size

of the particles, there will not be any significant scattering of microwaves (which have wavelengths larger than a few millimeters) by the gas molecules.

The parameter of interest when dealing with gas and radiation is the absorption coefficient. It depends on frequency, pressure, temperature, and the gas species. Transitions between rotational and vibrational resonance states take place at certain frequencies, which are determined by the molecule on one hand and its environment on the other hand: Temperature and pressure define the population of the energetic levels as well as the lifetime of these molecular states.

From the position dependent absorption coefficient  $\sigma_a(z)$  we can define the optical depth (or optical thickness)

$$\delta(z) = \int_z^{z_{top}} \sigma_a(z') dz' \quad (2.32)$$

by integrating the absorption coefficient  $\sigma_a$  along the line of sight  $z$  up to the total height of the atmosphere  $z_{tot}$ . The corresponding transmission

$$T = \frac{I(z)}{I_0} = \frac{I_0 \exp(-\delta(z))}{I_0} = \exp(-\delta(z)) \quad (2.33)$$

is given by the ratio of attenuated intensity to incident intensity.

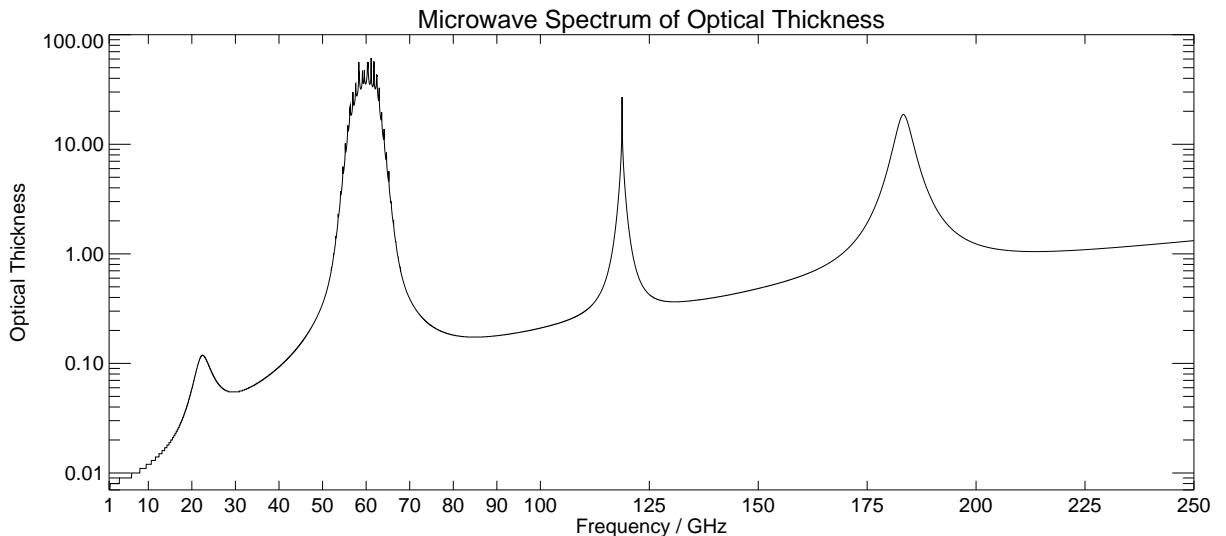


Figure 2.5: *Spectrum of microwave optical thickness produced by atmospheric gases for the atmosphere with US-standard atmosphere conditions at nadir direction.*

The gas species of relevance for the lower portion of the MW spectrum (1 to 200 GHz) are oxygen ( $O_2$ ), water vapour ( $H_2O$ ), and nitrogen ( $N_2$ ). At frequencies below 200 GHz the most important contributions to the total gas absorption are the water vapor line at 22.235 GHz, the oxygen absorption band around 60 GHz, the oxygen line at 118 GHz, and the 183 GHz water vapour line. Figure 2.5 gives the resulting total optical depth at nadir direction over frequency for a specific atmosphere.

These resonant frequencies produce a total optical thickness between 1 and 100 and therefore a total transmission close to zero (Fig. 2.6). The resonant regions are separated

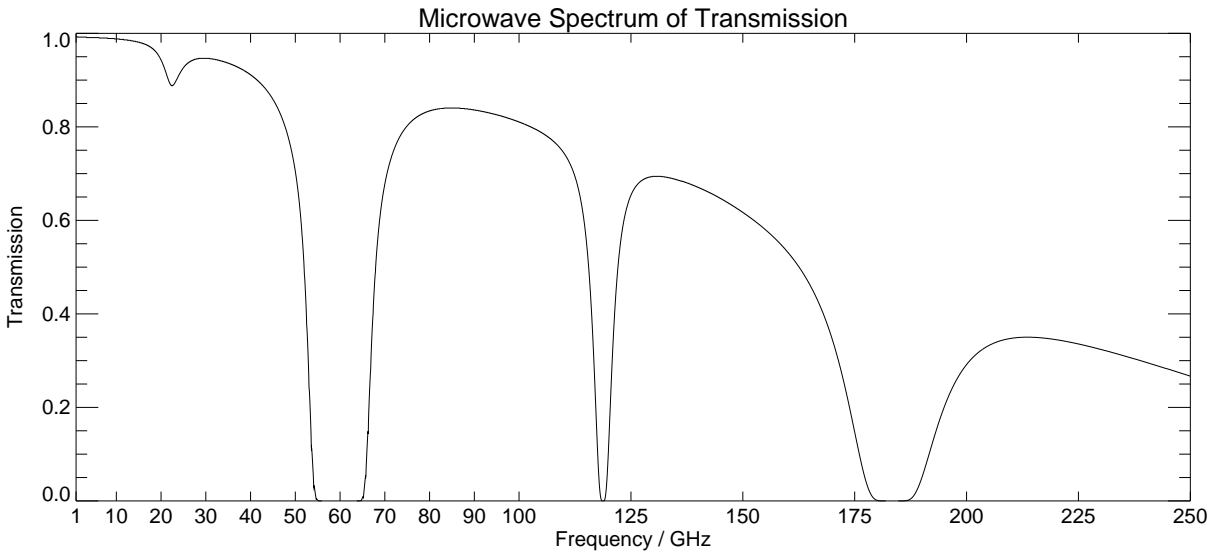


Figure 2.6: *Spectrum of microwave transmission by the gaseous atmosphere with US-standard conditions at nadir direction.*

by transparent window regions with optical thicknesses below 0.1, thus enabling the remote sensing of the lower atmosphere and surface conditions by satellite instruments.

Since the vertical stratification of the atmosphere is not homogeneous — resulting in highly variable vertical profiles of the absorption coefficient and the thermodynamic temperature — the total brightness temperature (2.10) depends on the direction of propagation and the position of the sensor. Figure 2.7 shows the upwelling brightness temperature at the top of the atmosphere (solid line) and the downwelling brightness temperature at the bottom of the atmosphere (dash-dotted line). The computed intensity is emitted by the atmosphere itself, the boundary condition was set to a perfect reflecting (non-emitting) mirror.

The reflecting boundary condition causes the upwelling radiation to have (approximately) twice the intensity of the downwelling radiation. This is true for the window regions only where the self-absorption within the medium is small. At frequencies with higher optical thickness the emitted radiation is not capable of leaving the region of emission. As a consequence, the downwelling radiation simply represents the ambient temperature whereas the upwelling radiation originates from high and cold regions of the upper atmosphere.

This phenomenon has a high impact on TB in the 60 GHz oxygen absorption band: When the upwelling microwave radiation from the lower atmosphere (either emission or reflected downwelling radiation) is absorbed before leaving the atmosphere the total intensity drops in the middle of the line. With only the contributions from the upper atmosphere the brightness temperature is significantly smaller than the downwelling part. Furthermore, the line broadening (pressure and collision broadening) is reduced in the upper atmosphere, leading to sharp peaks in the spectral curves. These "spikes" may only be observed above saturated lines and originate from layers above 20 km in case of the oxygen lines.

Additional background absorption (also called *continuum absorption*) arises from the far wings of water vapor lines and the so called collision induced absorption of nitrogen.



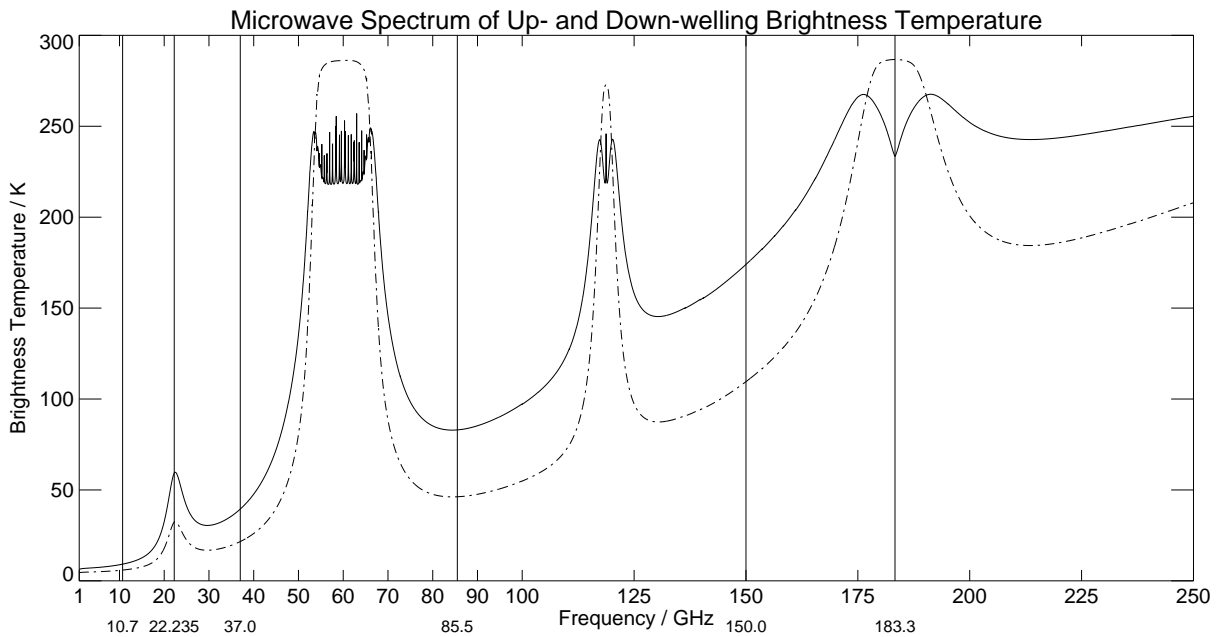


Figure 2.7: *Spectrum of microwave emission by the gaseous atmosphere with US-standard conditions at nadir direction: Upwelling (solid line) and downwelling (dash-dotted line) radiation at top of atmosphere and bottom of atmosphere. Vertical lines show some of the observing frequencies of ADEOS-II (10.7 GHz), SSM/I (22.235, 37 and 85.5 GHz) and AMSU-B (150 and 183 GHz).*

This contribution does not exhibit a strong frequency dependence and is difficult to calculate. Current research is dedicated to this topic (*Bauer et al., 1999; Borysov and Frommhold, 1986; Rosenkranz, 1998*).

Figure 2.8 illustrates the limitations for the Liebe model at frequencies above 90 GHz. The results of this graph were calculated by Feist (*Feist and Kämpfer, 1998; Feist, 1999*) using all known trace gas emission spectra according to the natural volume mixing ratios within a standard atmosphere.

For surface observations the optical thickness due to water vapor and oxygen is high enough for a saturation of the observed temperature at the ambient temperature. At higher altitudes the line spectrum caused by a large number of trace gases (such as ozone, BrO, etc.) can be observed. This spectrum is not contained in the Liebe model and may be of importance for observations from space or observations in very cold and dry atmospheres, especially at high altitudes.

### 2.5.2 Single scattering by hydrometeors

Depending on size and shape of the scattering particles different methods can be applied to calculate the single scattering parameters, which describe the extinction, emission, and scattering process. The size parameter  $\chi = 2\pi r / \lambda$  gives the ratio of particle radius  $r$  to wavelength  $\lambda$  and allows some classification. If  $\chi \ll 1$  the Rayleigh approximation is valid and the exact shape of the particle is of no importance. For particles that are large compared to wavelength ( $\chi \gg 1$ ) the geometric optics approximation, also known as ray tracing technique, might be applied (e.g., *Macke et al. (1996)*). In the range of particle

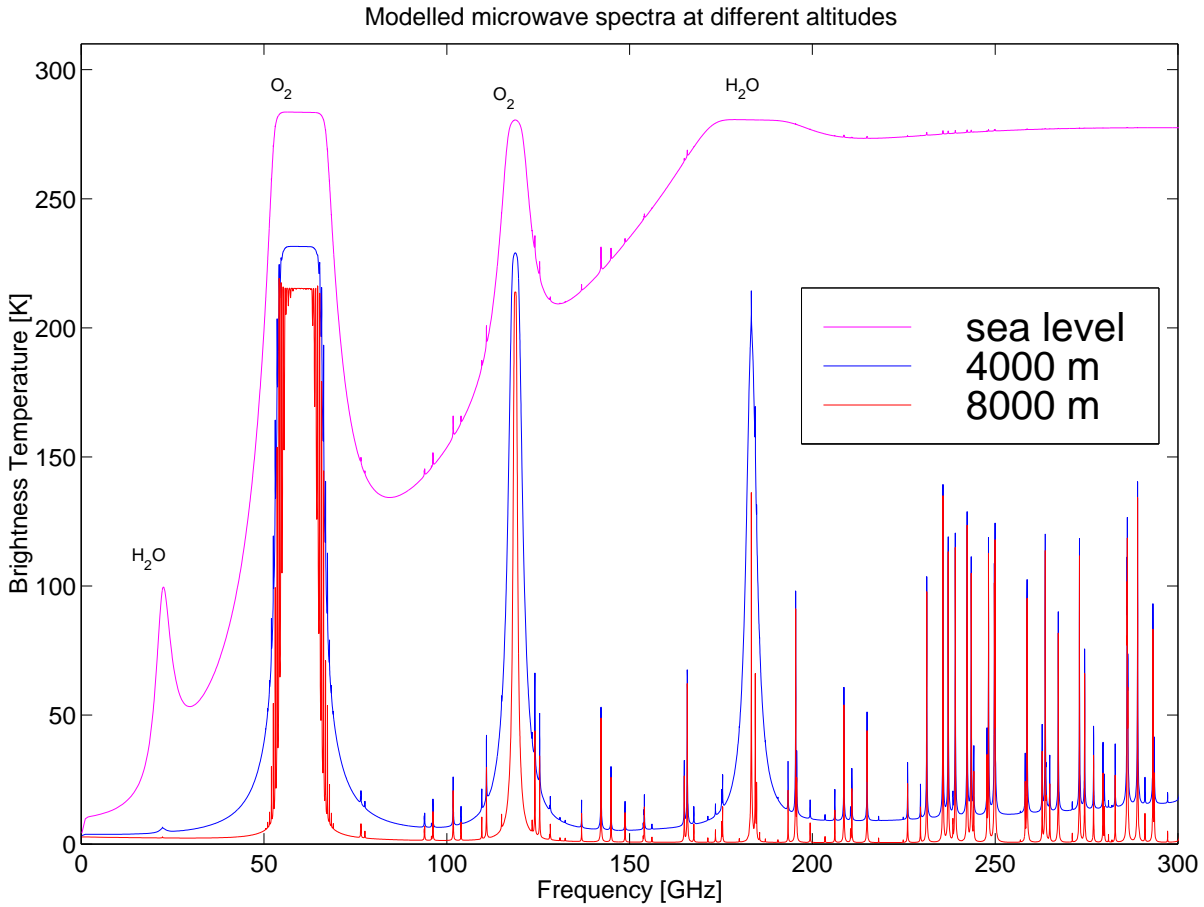


Figure 2.8: *Spectrum of downwelling microwave radiation emitted by the gaseous atmosphere with US-standard conditions at nadir direction: The height of observation is varied, the highest brightness temperatures correspond to observations from surface. Higher observation altitudes result in lower brightness temperatures and a more pronounced line spectrum of trace gases. (The uppermost line corresponds to observation at the sea level, the lowest line shows the observation at 8km altitude, the line in between is for 4 km observing height.*

sizes comparable to wavelength exact solutions of Maxwell's equations have to be used taking into account the shape of the particle.

For spherical shapes — an assumption that is only valid for small cloud droplets but often used for all hydrometeors — there exists a rigorous solution by *Mie* (1908). The amplitude scattering function ASF links the incident polarized plane wave  $(E_{vi}, E_{hi})$  to the scattered wave  $(E_{vs}, E_{hs})$  in the following form:

$$\begin{pmatrix} E_{vs}(\theta, \phi) \\ E_{hs}(\theta, \phi) \end{pmatrix} = \begin{pmatrix} f_{vv}(\theta, \phi; \theta', \phi') & f_{vh}(\theta, \phi; \theta', \phi') \\ f_{hv}(\theta, \phi; \theta', \phi') & f_{hh}(\theta, \phi; \theta', \phi') \end{pmatrix} \begin{pmatrix} E_{vi}(\theta', \phi') \\ E_{hi}(\theta', \phi') \end{pmatrix}. \quad (2.34)$$

In case of spherical particles the matrix containing the ASF in eq. (2.34) is diagonal. Numerical models have been developed to obtain the ASF for nonspherical particles (*Draine and Flatau, 1994; Flatau et al., 1993; Fournier and Evans, 1993; Rother and Schmidt, 1996; Waterman, 1971; Matsumura and Seki, 1996; Oguchi and Hosoya, 1974;*

*Barber and Yeh, 1975; Eremin et al., 1995; Mishchenko et al., 1996b; Mishchenko, 1993*).

All interaction parameters can be calculated applying equation (2.34) using the Stokes vector definition (2.14). According to *Tsang et al. (1985)* the extinction matrix  $\bar{\sigma}_e(\theta, \phi)$  is computed with the optical theorem from the forward scattering amplitudes. With equal angles  $\theta = \theta'$ ,  $\phi = \phi'$  and the definition  $M_{jl} = \frac{i2\pi}{k} f_{jl}(\theta, \phi; \theta, \phi)$  it reads:

$$\bar{\sigma}_e(\theta, \phi) = \begin{pmatrix} -2\text{Re}(M_{vv}) & 0 & -\text{Re}(M_{vh}) & -\text{Im}(M_{vh}) \\ 0 & -2\text{Re}(M_{hh}) & -\text{Re}(M_{hv}) & \text{Im}(M_{hv}) \\ -2\text{Re}(M_{hv}) & -2\text{Re}(M_{vh}) & -(\text{Re}(M_{vv}) + \text{Re}(M_{hh})) & (\text{Im}(M_{vv}) - \text{Im}(M_{hh})) \\ 2\text{Im}(M_{hv}) & -2\text{Im}(M_{vh}) & -(\text{Im}(M_{vv}) - \text{Im}(M_{hh})) & -(\text{Re}(M_{vv}) + \text{Re}(M_{hh})) \end{pmatrix}. \quad (2.35)$$

All four angles are necessary for the scattering phase matrix  $\bar{\mathbf{P}}(\theta, \phi; \theta', \phi')$ :

$$\bar{\mathbf{P}}(\theta, \phi; \theta', \phi') = \begin{pmatrix} |f_{vv}|^2 & |f_{vh}|^2 & \text{Re}(f_{vh}^* f_{vv}) & -\text{Im}(f_{vh}^* f_{vv}) \\ |f_{hv}|^2 & |f_{hh}|^2 & \text{Re}(f_{hh}^* f_{hv}) & -\text{Im}(f_{hh}^* f_{hv}) \\ 2\text{Re}(f_{vv} f_{hv}^*) & 2\text{Re}(f_{vh} f_{hh}^*) & \text{Re}(f_{vv} f_{hh}^* + f_{vh} f_{hv}^*) & -\text{Im}(f_{vv} f_{hh}^* - f_{vh} f_{hv}^*) \\ 2\text{Im}(f_{vv} f_{hv}^*) & 2\text{Im}(f_{vh} f_{hh}^*) & \text{Im}(f_{vv} f_{hh}^* + f_{vh} f_{hv}^*) & \text{Re}(f_{vv} f_{hh}^* - f_{vh} f_{hv}^*) \end{pmatrix}. \quad (2.36)$$

The absorption in the case of nonspherical particles is no longer a single number but becomes a four component vector that varies with the direction of incidence. In general, it is the total radiation loss (extinction) minus all radiation that is scattered into directions other than the direction of propagation. We obtain

$$\bar{\sigma}_a(\hat{r}) = \begin{pmatrix} \frac{4\pi}{k} \text{Im} f_{vv}(\hat{r}, \hat{r}) - \int d\Omega' (|f_{vv}(\hat{r}', \hat{r})|^2 + |f_{hv}(\hat{r}', \hat{r})|^2) \\ \frac{4\pi}{k} \text{Im} f_{hh}(\hat{r}, \hat{r}) - \int d\Omega' (|f_{vh}(\hat{r}', \hat{r})|^2 + |f_{hh}(\hat{r}', \hat{r})|^2) \\ 2\text{Re} \left\{ \frac{2\pi i}{k} [f_{vh}^*(\hat{r}, \hat{r}) - f_{hv}(\hat{r}, \hat{r})] - \int d\Omega' [f_{vv}(\hat{r}', \hat{r}) f_{vh}^*(\hat{r}', \hat{r}) + f_{hv}(\hat{r}', \hat{r}) f_{hh}^*(\hat{r}', \hat{r})] \right\} \\ 2\text{Im} \left\{ \frac{2\pi i}{k} [f_{vh}^*(\hat{r}, \hat{r}) - f_{hv}(\hat{r}, \hat{r})] - \int d\Omega' [f_{vv}(\hat{r}', \hat{r}) f_{vh}^*(\hat{r}', \hat{r}) + f_{hv}(\hat{r}', \hat{r}) f_{hh}^*(\hat{r}', \hat{r})] \right\} \end{pmatrix}. \quad (2.37)$$

For decoupled third and fourth components of the Stokes vector the absorption, extinction, and scattering matrices reduce to the following simpler forms:

$$\bar{\sigma}_e(\theta, \phi) = \begin{pmatrix} -2\text{Re}(M_{vv}) & 0 \\ 0 & -2\text{Re}(M_{hh}) \end{pmatrix}, \quad (2.38)$$

$$\bar{\mathbf{P}}(\theta, \phi; \theta', \phi') = \begin{pmatrix} |f_{vv}|^2 & |f_{vh}|^2 \\ |f_{hv}|^2 & |f_{hh}|^2 \end{pmatrix}, \quad (2.39)$$

$$\bar{\sigma}_a(\hat{r}) = \begin{pmatrix} \frac{4\pi}{k} \text{Im} f_{vv}(\hat{r}, \hat{r}) - \int d\Omega' (|f_{vv}(\hat{r}', \hat{r})|^2 + |f_{hv}(\hat{r}', \hat{r})|^2) \\ \frac{4\pi}{k} \text{Im} f_{hh}(\hat{r}, \hat{r}) - \int d\Omega' (|f_{vh}(\hat{r}', \hat{r})|^2 + |f_{hh}(\hat{r}', \hat{r})|^2) \end{pmatrix}. \quad (2.40)$$

By integrating over  $\phi'$  and averaging over  $\phi$  (with only one angle  $\phi$ ) the azimuthal dependence is cancelled out for isotropic conditions.

The above equations describe scattering by a single particle of a certain size. In order to calculate the radiation interaction parameters of a specific atmospheric layer we have to integrate equations (2.35), (2.36), and (2.37) over particle size distributions. A variety of different particle size spectra have been developed for the description of cloud and precipitation processes. Some of these distributions will be discussed in the modeling chapter (section 3.1.4).

In case of particles with spherical shape or random orientation the absorption and scattering cross sections do not depend on direction and polarization and therefore can be represented by simple scalar numbers. From the total absorption and scattering cross sections  $\sigma_a$  and  $\sigma_s$  one can define absorption efficiencies

$$Q_a = \frac{\sigma_a}{2\pi r^2} \quad (2.41)$$

$$\text{and } Q_s = \frac{\sigma_s}{2\pi r^2} \quad (2.42)$$

with an effective radius  $r$  describing the size of the particle. The relation between the extinction cross section and the geometric cross section describes how efficient a particle with geometric size  $2\pi r^2$  blocks radiation from a beam of light in terms of fractions of its own size. In the optical limit for large particles (compared to wavelength) the extinction efficiency tends towards 2, thus the fraction of light, which is prevented from propagating forward with the same direction is twice the geometric size of the particle (*van de Hulst*, 1981).

## 2.6 Boundary conditions

Solving the VRTE requires the upper and lower boundary conditions in terms of reflection, scattering, and absorption of MW radiation. The upper boundary condition is easily obtained by assuming a background temperature of 2.7 K for space. The effect of the sun, a source with a brightness temperature above 6000 K, can be neglected in most instances for the following reason: The enormous intensity of the sun is only emitted within a very small angular interval. The width of the sun disk is approximately 0.5 degree, so even an antenna in uplooking geometry with a larger beam width will only receive a diminished signal by averaging the sharp peak of the sun over the whole antenna pattern.

A radiometer with a 5 degree beam width (a factor of 10 in angular resolution compared to the peak of the sun) will average the signal of the sun over an angular pattern which is a hundred times larger, thus leading to a reduction of the sun signal by a factor of 100. In scattering media and especially for downlooking radiometers the radiation of the sun will be even more diluted and can be neglected. However, for perfect reflecting surfaces there may be a specular reflection of the sun signal. Observation of the sun with radiometers for the remote sensing of clouds, which are between observer and sun is also possible. For radiometers with good pointing quality like the MICCY instrument

(Crewell et al., 1999b) with less than 1 degree in all 22 channels the contribution from the solar source will be of particular interest.

Reflection and absorption of MW radiation at land surfaces cannot be calculated with sufficient accuracy for the remote sensing of rain at low frequencies, especially in the presence of canopy layers above the soil. Only in case of calm water surfaces there exists a quite accurate treatment of surface reflection: The interaction of electromagnetic radiation with a plane boundary between two dielectric media is described by the Fresnel reflection.

The reflected intensity is the incident intensity multiplied by the reflectivity. For polarized radiation the reflectivity is given in terms of the complex reflection coefficient  $R(\theta)$ , which is

$$R_v(\theta) = \frac{\mu_w \epsilon_w \cos \theta - \sqrt{\epsilon_w - \sin^2 \theta}}{\mu_w \epsilon_w \cos \theta + \sqrt{\epsilon_w - \sin^2 \theta}} \quad \text{and} \quad (2.43)$$

$$R_h(\theta) = \frac{\cos \theta - \sqrt{\epsilon_w - \sin^2 \theta}}{\cos \theta + \sqrt{\epsilon_w - \sin^2 \theta}} \quad (2.44)$$

for vertical and horizontal polarization. It is a function of incident angle  $\theta$  (see Fig. 2.9) and depends on the complex dielectric constants  $\epsilon_{w,a}$  and the magnetic permittivities  $\mu_{w,a}$  of water and air. The absolute values for air and the absolute magnetic permittivity of water are close to those of the vacuum, resulting in relative values of unity. The dielectric constant for microwave radiation within water depends on frequency, temperature, and salinity. Furthermore, the phase (liquid, solid) has a strong impact on the dielectric properties of water.

The reflection of radiation described by a four-component Stokes vector is obtained by the reflection matrix

$$\overline{\overline{\mathbf{R}}}(\theta) = \begin{pmatrix} |R_v(\theta)|^2 & 0 & 0 & 0 \\ 0 & |R_h(\theta)|^2 & 0 & 0 \\ 0 & 0 & \text{Re}(R_v(\theta)R_h^*(\theta)) & -\text{Im}(R_v(\theta)R_h^*(\theta)) \\ 0 & 0 & \text{Im}(R_v(\theta)R_h^*(\theta)) & \text{Re}(R_v(\theta)R_h^*(\theta)) \end{pmatrix} \quad (2.45)$$

$$\equiv \begin{pmatrix} R_1(\theta) & 0 & 0 & 0 \\ 0 & R_2(\theta) & 0 & 0 \\ 0 & 0 & +R_3(\theta) & -R_4(\theta) \\ 0 & 0 & +R_4(\theta) & +R_3(\theta) \end{pmatrix} \quad (2.46)$$

which gives the resulting Stokes vector (Tsang et al., 1985). Perfectly smooth surfaces reflect the incident light to a single zenith angle and therefore act like a mirror with a certain amount of transmission. The transmitted microwave intensity is absorbed within a short distance in water (Simmer, 1994). Surfaces with wind induced waves can be modeled by facettes of different sizes with different slopes (Schrader, 1995). Subscale ripples of the surface with sizes smaller than wavelength may also be parametrized. Foam coverage is implemented in the model as an absorbing layer above the sea surface.

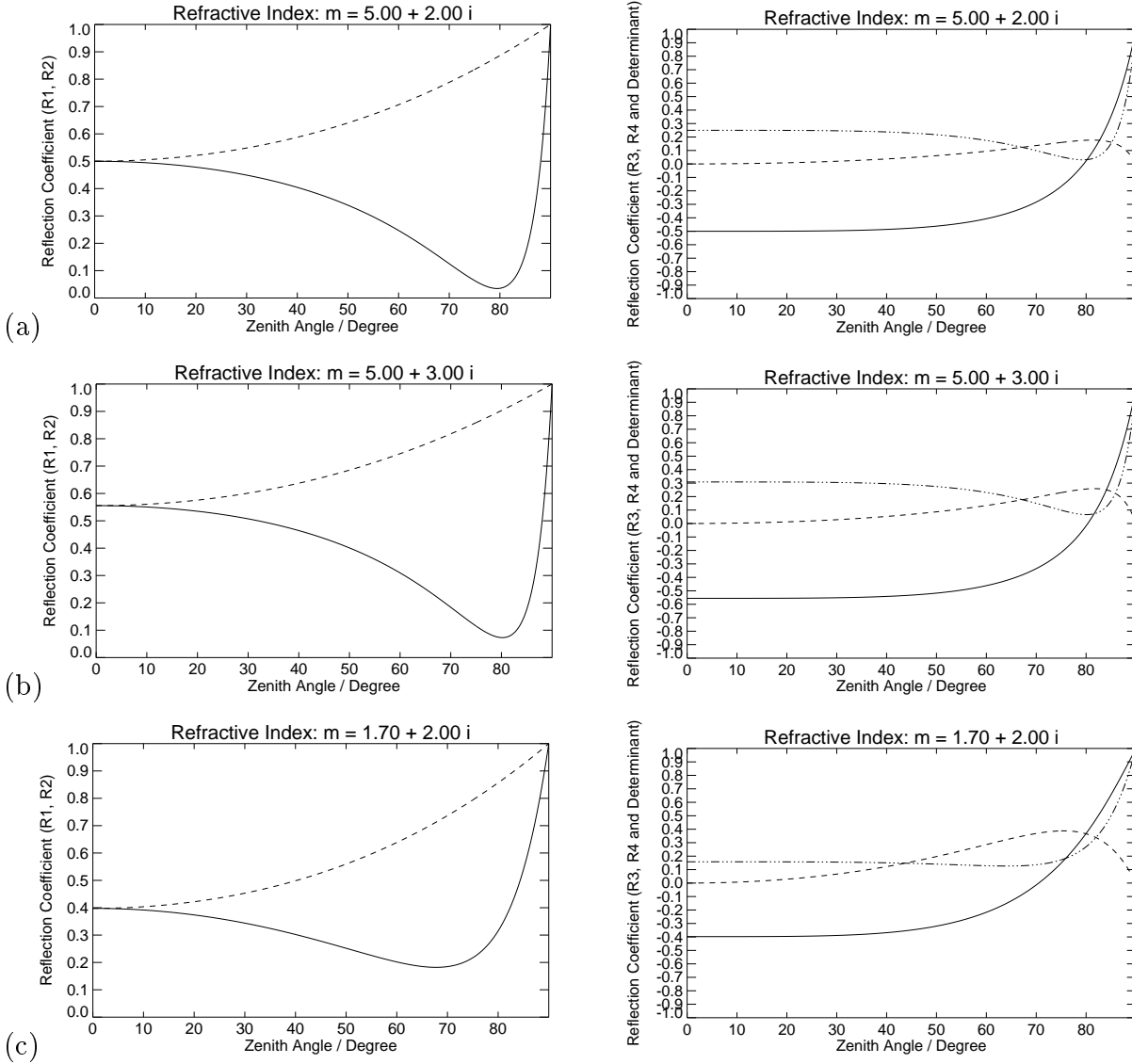


Figure 2.9: Elements  $R_1$  (left, solid),  $R_2$  (left, dashed) of the reflection matrix eq. (2.45) for different refractive indices: (a)  $m = 5 + 2i$ , (b) higher absorption:  $m = 5 + 3i$ , (c) smaller real part of refractive index:  $m = 1.7 + 2i$ . The Brewster angle close to 80 degree is visible in the vertical polarisation ( $R_1$ ) and in determinant of the  $2 \times 2$  sub-matrix of  $R_3$  and  $R_4$  as well.

The elements of (2.46) are given in Fig. 2.9 as a function of incident angle  $\theta$ . The Brewster angle  $\theta_B$  of maximum polarization is observed at

$$\cos \theta_B = m' \quad (2.47)$$

with  $m'$  the real part of the refractive index of the medium. The reflectivity for horizontal polarization increases with incident angle until it reaches perfect reflectivity of 1.0 for grazing incidence. Vertical polarized radiation is transmitted through the surface (instead of reflected) at  $\theta_B$ , leading to a highly polarized emission of sea surface at this angle.

The  $R_3$  diagonal component of the reflection matrix conserves the  $U$  and  $V$  compo-

nents of the Stokes vector only if it is unity. For most angles the  $R_3$  component is the negative value of the  $R_1$  and  $R_2$  values at zero angle while the  $R_4$  element is zero. The overall intensities of the  $U$  and  $V$  components is decrease in proportion to the attenuation of  $I_v$  and  $I_h$ . The change in sign results from mirroring the radiation within the fixed frame of the global coordinate system.

The determinant of the  $(2 \times 2)$  submatrix of  $R_3$  and  $R_4$  is shown for reasons of clarification: If the reflection is only a rotation or mirror process to the  $U$  and  $V$  components the determinant should be plus or minus one, respectively. This is not the case since the determinant depends on angle and for angles closer to the Brewster angle mixing takes place between the  $U$  and  $V$  component: The value of  $R_4$  gives the amount of exchange between both components. At  $\theta_B$  this exchange is at maximum while the  $R_3$  is zero. Thus the reflected parts of  $U$  and  $V$  only depend on their counterparts ( $V$  and  $U$ ). This effect becomes larger with smaller real parts and larger imaginary parts of the refractive index.

Ice, snow, and land surfaces show a much more complicated behaviour. The reflection becomes diffuse instead of specular, a bistatic scattering matrix depending on the incident and reflected directions describes the distribution of light to different directions and the exchange between Stokes components during this process.





## Chapter 3

# Numerical Solution of Radiative Transfer

The purpose of the numerical model is to find a solution of the VRTE (2.31) with boundary conditions. Only for "clear-sky" conditions (cloudless, no scattering) the radiative transfer can be solved analytically, but the presence of scattering prevents this solution.

Prior to the numerical integration procedure the VRTE needs to be discretized: All continuous variables (e.g., such as position and angle of propagation direction) are approximated by a set of discrete values. Provided that the solving algorithm itself is not approximative, the resulting solution will converge to the true solution when the discretization is made fine enough. After the selection of a suitable discretization mechanism, three major tasks have to be performed:

- definition of the geophysical environment in terms of atmospheric profiles of temperature, humidity, pressure, hydrometeor content, and hydrometeor size distributions,
- calculation of corresponding optical properties (interaction parameters), and
- solution of the VRTE by a numerical algorithm (Monte Carlo methods, integration schemes, successive order of scattering method).

The model which is used in this study is based on the radiative transfer model MW-MOD developed by *Simmer* (1994). It is a one-dimensional plane parallel model for polarized (two components of Stokes vector) microwave radiation, which has been tested and validated with other models and measured data. MW-MOD has been used for several remote sensing studies during the past years (*Karstens et al.*, 1994; *Fuhrhop and Simmer*, 1996; *Fuhrhop et al.*, 1998; *Liu and Simmer*, 1996).

In the present form MW-MOD has been extended to include multiple scattering effects by nonspherical particles (in contrast to the previous limitation to Rayleigh and Mie scattering for spherical particles). The previous version was able to handle absorption and extinction coefficients only as scalar numbers. The phase functions allowed mixing between vertical and horizontal polarization (dealing with a two-component Stokes-vector) by the scattering process.

The main component of this study is the improvement of the MW-MOD model package and the testing of the new model. On one hand the representation of drop size and -shape distributions was changed to account for the shape of the hydrometeors and the variation

of shape with size. On the other hand the single scattering calculations and the radiative transfer scheme were completely changed: For nonspherical particles with non-random orientation the absorption and extinction numbers will depend on propagation direction and polarization and thus will be given as matrices. Since single scattering results cannot be obtained from simple Mie-Theory any longer, sophisticated single scattering models from other scientific groups have to be used. The connection of such models with the radiative transfer models is crucial for the implementation of a radiative transfer scheme that accounts for nonspherical particles. The following pages will give a brief explanation of all main components of the model.

## 3.1 Definition of environment

### 3.1.1 Discretization grid

As a consequence of the one-dimensional and isotropic nature of the model only three variables of position and direction need to be considered: Vertical position  $z$ , zenith angle of propagation  $\theta$  and zenith angle of scattering source integration  $\theta'$ . The horizontal position  $(x, y)$  and the azimuthal angles  $(\phi, \phi')$  are not in use in a one-dimensional model.

The vertical grid can be chosen in any resolution and does not need to be regularly spaced. In addition to an explicit definition by giving layer boundaries it is possible to use radiosonde data for the definition of the atmosphere. In this case the level spacing of the radiosonde is used and, if necessary, extended to a requested minimum height. Both methods are used only for the atmospheric definition and therefore may use a coarse resolution. The radiative transfer scheme builds a sufficiently small level spacing to assure homogeneous layers high accuracy results.

The zenith angles  $\theta$  and  $\theta'$  are always discretized in the same way. For the integration schemes of the scattering source function are very sensitive to the choice of angles, two standard mechanisms of numerical integration procedures may be chosen: Gauss-Legendre and Gauss-Lobatto angles in arbitrary numbers are possible choices. These discrete angles are optimal for the integration of Legendre polynomials of corresponding degrees.

The definition of arbitrary numbers of regularly or irregularly spaced angles is possible as well. Under this condition, the integration weights for each angle are calculated from the actual angle spacing. For very inhomogeneous choices of angles the convergence of the scattering integral will be poorer than for Gauss angles.

### 3.1.2 Surface definition

The surface below the atmosphere is described by its reflectivity and emissivity. These parameters generally depend on frequency, viewing angle, and polarization. The simplest choice (of reflectivity) is a set of angle dependent or frequency dependent reflectivities given by the user defined input to the model. The latter choice is only useful when the model is used to calculate the same atmospheric setup for different frequencies.

These options include two commonly used special cases, which either assume black-body emission (surface emissivity  $\epsilon_s = 1.0$ ) or a perfectly reflecting mirror ( $\epsilon_s = 0.0$ ).

These idealized conditions are favourable for case studies which add to the general understanding of polarized radiative transfer since they allow for a selection of radiation sources: With  $\epsilon_s = 0.0$  the whole MW radiation originates from atmospheric constituents without any disturbance by upwelling radiation from the surface. Switching to blackbody conditions produces a strong upwelling radiation flux as it is found above land surfaces with an average emissivity above 0.9, which is fully unpolarized.

A more realistic choice of surface reflectivity is given by the Fresnel reflection matrix for water surfaces. Since the refractive index varies with frequency, salinity, and sea surface temperature (SST) the calculated reflectivity depends on these parameters and in addition on the viewing angle and the state of polarization.

This Fresnel reflection may also be calculated for wind induced roughness of sea surfaces. A three-scale facette model with foam coverage (different parametrizations) can be used for a given wind speed.

### 3.1.3 Vertical profiles

Within the specified vertical grid the profiles of pressure, temperature, and relative humidity have to be defined. The data can be taken from radiosonde observations or from the input parameter file. If no profile data, either measured or from any other source, are supplied the atmospheric conditions are calculated from surface values of temperature, pressure, and humidity by assuming user defined lapse rates for the temperature with height.

The presence of hydrometeors can be prescribed for every individual layer or determined from radiosonde profiles (e.g., using a threshold of 95 % for relative humidity). In this study only the explicit form of hydrometeor definition is used.

Every layer is capable of holding a mixture of several different hydrometeor species. These types of hydrometeors may consist of liquid and frozen cloud and precipitation particles, each with a distinct drop size distribution. The liquid water content (LWC), ice water content (IWC), and the actual rain rate are calculated from this data for every layer. Finally, the liquid water path (LWP), the ice water path (IWC), and the cloud top temperatures are given for the entire atmosphere.

### 3.1.4 Drop size distributions

Hydrometeors exist in a large variety of sizes. Depending on the microphysical processes that generated the cloud or precipitation particles, each size interval is populated with a specific number of particles. Such distributions of particle number with particle size are called *particle size distributions* (PSD) or more commonly *drop size distributions* (DSD). They have the form

$$n(r) = f(r) \tag{3.1}$$

and give the number of drops with a radius within the interval  $(r, r + dr)$ .

For small cloud droplets many DSDs exist, which are commonly characterized by an exponential decrease of drop number with increasing drop size. Natural DSD show, in accordance with measured spectra, a decay in drop number when the radius converges to zero. Such DSD show a maximum drop number at a certain drop size, which is

called the modal radius. A general mathematical representation of DSD with the above characteristics is the modified gamma distribution (MGD)

$$n(r) = ar^\alpha \exp(-br^\gamma). \quad (3.2)$$

The radiative transfer model has 20 predefined DSD which are fitted to the MGD for different types of clouds.

Precipitation particles tend to have much larger sizes than cloud particles and require a different DSD for a proper description. The particle spectrum of rain is often described by a distribution found by *Marshall and Palmer* (1948). It is defined by

$$n(r) = N_0 \exp(-qr) \quad (3.3)$$

with  $N_0 = 16\,000 \text{ m}^{-3} \text{ mm}^{-1}$ ,  $q = 8.2RR^{-0.21}$  and the rain rate RR given in mm/h.

The Marshall-Palmer DSD (3.3) emerges to be a special case of the MGD with  $\gamma = 1$  and  $\alpha = 0$ . It does not have a characteristic maximum but due to the rain rate dependent exponent  $q = 8.2RR^{-0.21}$  the fraction of large drops is increased at higher rain rates.

The current implementation of MWMOD can handle all four parameters of the MGD as input parameters. The integration of the DSD requires the number of integration intervals and the integration limits. Usually 50 equally spaced radius intervals are used, the upper and lower limits depend on the DSD. These parameters may be changed on input, too.

### 3.1.5 Hydrometeor shapes

The shapes of hydrometeors show a strong variation: Ice crystals and snow flakes exhibit strongest differences from spherical shape. Cirrus clouds in high altitudes consist of hexagonal plates, columns, rosettes, and irregular clusters of these primary shapes. These ice particles are generally very small and only have a minor contribution to the radiative transfer signal in the low microwave frequency regime. Larger ice particles, especially snowflakes and hailstones, have to be considered in radiative transfer calculations, but the shape cannot be effectively described by simple parametrizations. Hailstones sometimes show conical forms, but the overall occurrence of hail shapes is irregular.

The situation for liquid phase hydrometeors is more clear. Only very small raindrops with diameters well below 1 mm are perfect spheres due to surface tension. Larger drops tend to be flattened at the bottom, leading to oblate shapes. When describing drop shapes, we refer to the work of *Chuang and Beard* (*Chuang and Beard*, 1990; *Beard and Chuang*, 1987), who used a dynamic model to study the behaviour of falling water drops. The influences of hydrostatic pressure, friction, surface tension, and electric fields are taken into account, resulting in rotational symmetric shapes with cross sections  $r = r(\theta)$  that can be described by a series of Chebyshev polynomials in  $\cos(n\theta)$

$$r(\theta) = r_0 \left( 1 + \sum_{n=0}^N c_n \cos(n\theta) \right). \quad (3.4)$$

The radius of the undistorted drop is given by  $r_0$  and the coefficients  $c_n$  ( $n = 0, 1, \dots, 10$ ) for drop sizes from 1 mm to 9 mm diameter are taken from *Chuang and Beard* (1990) and listed in Table 3.1.

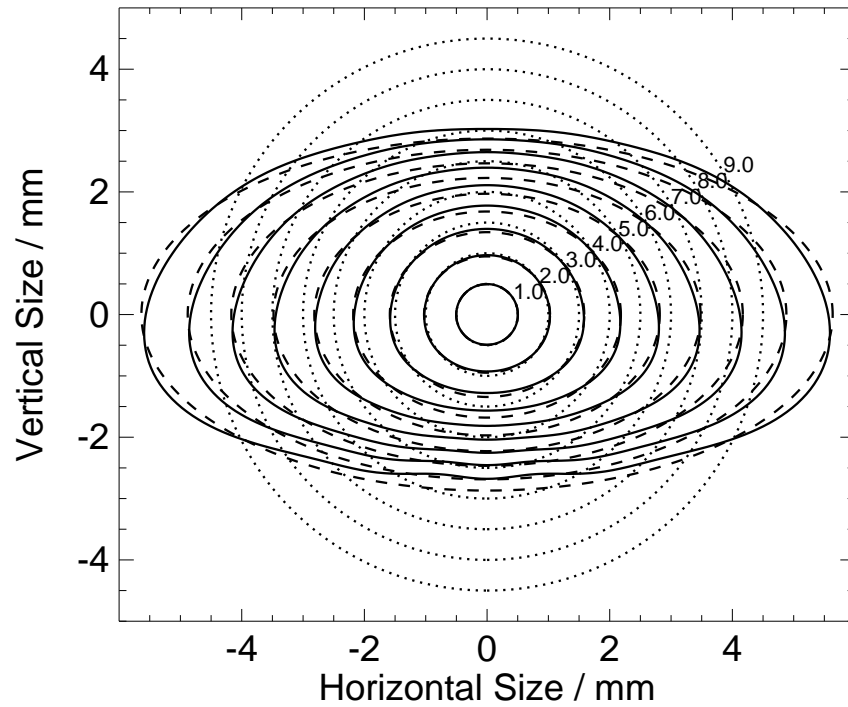


Figure 3.1: *Cross sections of falling drops (solid line) according to Chuang and Beard (1990). Equivalent volume spheres (dashed line) and spheroids (dotted line) are given for reasons of comparison.*

Table 3.1: *Coefficients for shape definition*

d/mm	Shape Coefficients $c_n \times 10^4$										
	$c_0$	$c_1$	$c_2$	$c_3$	$c_4$	$c_5$	$c_6$	$c_7$	$c_8$	$c_9$	$c_{10}$
1.0	-28	-30	-83	-22	-3	2	1	0	0	0	0
1.5	-72	-70	-210	-57	-6	7	3	0	-1	0	1
2.0	-134	-118	-385	-100	-5	17	6	-1	-3	-1	1
2.5	-211	-180	-592	-147	4	32	10	-3	-5	-1	2
3.0	-297	-247	-816	-188	24	52	13	-8	-8	-1	4
3.5	-388	-309	-1024	-211	53	75	15	-15	-12	0	7
4.0	-481	-359	-1263	-244	91	99	15	-25	-16	2	10
4.5	-573	-401	-1474	-255	137	121	11	-36	-19	6	13
5.0	-665	-435	-1674	-258	187	141	4	-48	-21	11	17
5.5	-755	-465	-1863	-251	242	157	-7	-61	-21	17	21
6.0	-843	-472	-2048	-240	299	168	-21	-73	-20	25	24
6.5	-930	-487	-2207	-222	358	175	-37	-84	-16	34	27
7.0	-1014	-492	-2364	-199	419	178	-56	-93	-12	43	30
8.0	-1187	-482	-2650	-148	543	171	-100	-107	2	64	32
9.0	-1328	-403	-2899	-106	662	153	-146	-111	18	81	31

Resulting shapes are presented in Fig. 3.1, which also shows the cross sections of the corresponding spheres and spheroids of the same volume. Figure 3.1 makes clear that the spheres only give a poor approximation to the realistic drop shapes. The volume

equivalent spheroids have the same aspect ratio as the corresponding Chebyshev drops and are used as another simplified but more accurate drop shape in this study.

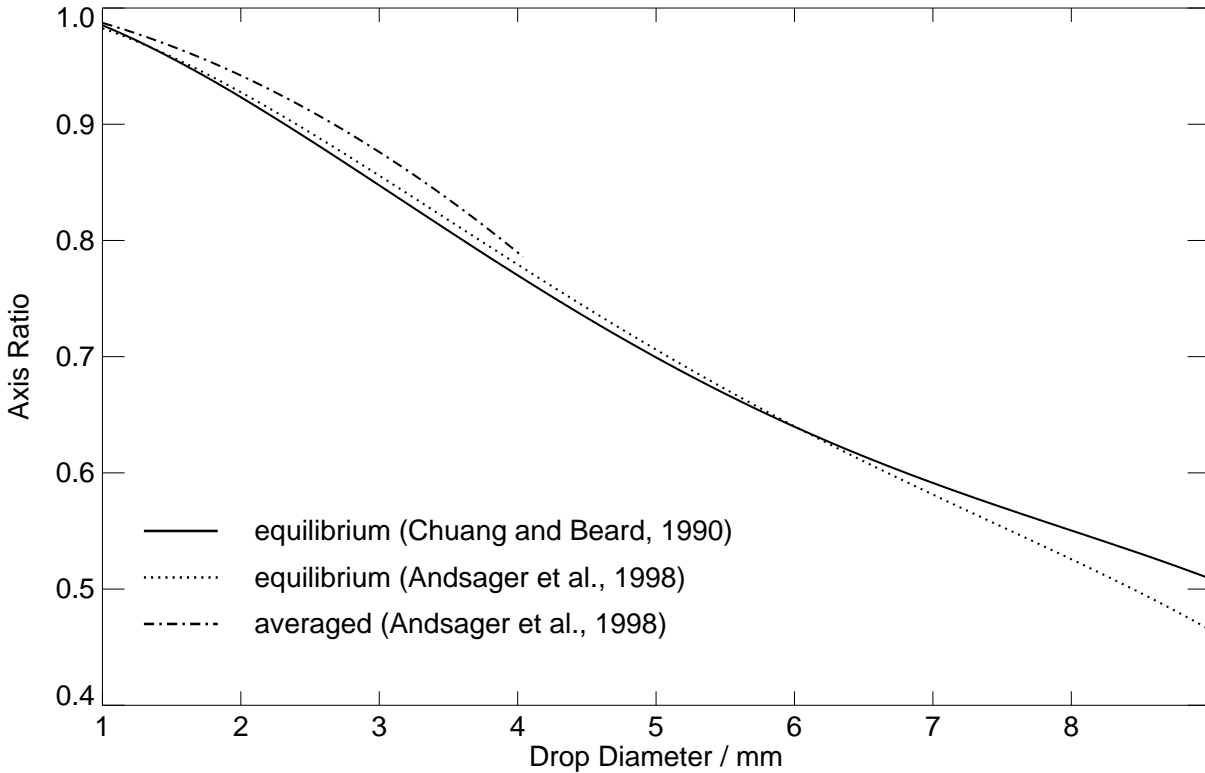


Figure 3.2: *Aspect ratio of falling drops: The modeled equilibrium shapes from Chuang and Beard (1990) (solid line), the equilibrium drop shapes measured by Andsager et al. (1998) (dotted line) and the averaged values for oscillating drops (dashed line, only valid up to 4.1 mm diameter, from Andsager et al. (1998)).*

The flattening of the drops increases with larger diameters and is more pronounced at their bottom, leading to particles that do not exhibit a symmetry between upward and downward directions. In addition, large drops will start to oscillate around this shape due to vortex shedding and collisions with other large drops. At this stage only equilibrium shapes are considered.

The aspect ratio  $\alpha$  of the Chebyshev particles, defined as the ratio of maximum vertical and horizontal extension, depends on the drop size  $d = 2r_0$ . It can be approximated with a fourth order fit (Chuang and Beard, 1990) to the numerical results

$$\alpha = 1.01668 - 0.98055d - 2.52686d^2 + 3.75061d^3 + 1.68692d^4 \quad (3.5)$$

and is plotted in Fig. 3.2 (solid line). Furthermore the most recent results of Andsager et al. (1998) are shown in which aspect ratios were fitted to experimental results. The aspect ratio of equilibrium drop shapes (dotted line) and the average aspect ratio for oscillating drops (only fitted for diameters less than 4.1 mm) are very close to the model calculations.

The above description of drop shape (oblate shape according to the drop size) and drop orientation (axis of rotational symmetry aligned to the vertical) is somewhat artificial. Natural drops will show oscillations around the equilibrium shapes that are used

throughout this study, especially for large drop diameters. The orientation is not expected to be absolutely perfect as the drops tumble while falling down. Furthermore, the presence of horizontal winds may lead to a tilting of the raindrop orientation according to the direction of wind speed.

## 3.2 Calculation of interaction parameters

### 3.2.1 Refractive index of water

Propagation of electromagnetic wave within a dielectric media is described by the complex refractive index  $m = m' + im''$ . It is linked to the complex dielectric constant  $\epsilon$  by

$$m^2 = \epsilon. \quad (3.6)$$

The real part  $m'$  gives the relative speed of light within the medium while the imaginary part  $m''$  determines the absorption within the medium.

The refractive index of water shows completely different characteristics for liquid water and ice, respectively. While ice has an real part of 1.78 and almost no absorption in the microwave spectral range, liquid water is highly absorbing. The real part  $m'$  generally is very large (Fig. 3.3) and reaches values above 9.0 for warm water and low frequencies (e.g., 10 GHz).

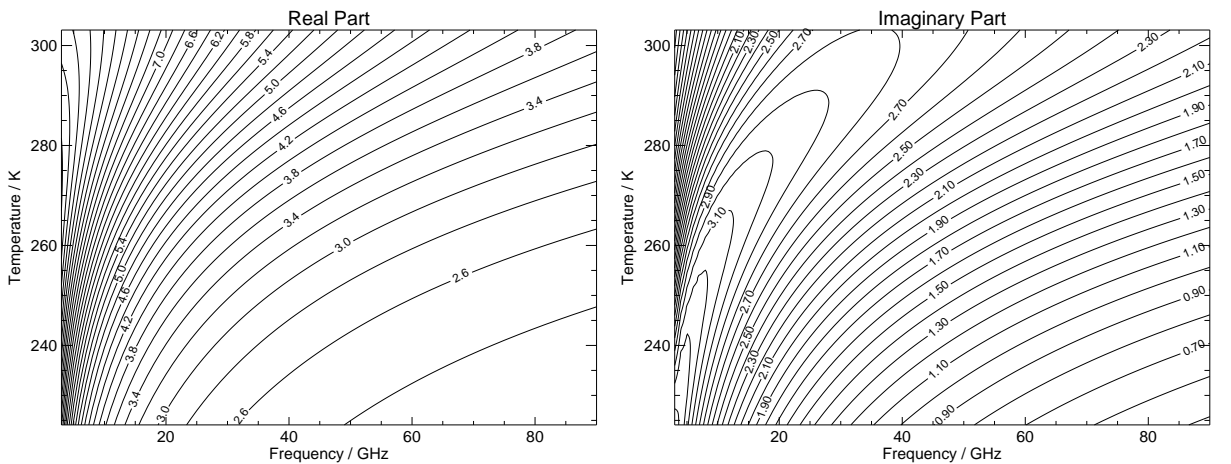


Figure 3.3: *Real part and imaginary part of refractive index.*

The temperature dependence of the absorption (Fig. 3.3) reveals a stronger dependence on temperature than the real part. Besides temperature, frequency, and phase of water the refractive index is affected by the salinity of water. All effects are parametrized according to *Ulaby et al. (1986)* whose parametrization is used in this model. The refractive index of ice is nearly constant for salt-free ice and given with  $m = 1.78 + i(0.00065 \pm 0.00005)$ .

### 3.2.2 Gas absorption

The absorption of MW radiation by the earth's atmosphere is subject of extensive measurements (e.g., *Bauer et al. (1999)*; *Jaquinet-Husson et al. (1998)*; *Rosenkranz (1998)*; *Pol et al. (1998)*). The resulting spectral parameters (such as center frequencies, frequency shifts, line width, line shape, line broadening) are used for parametrization of the absorption spectrum. A widely used parametrization is the MPM (microwave propagation model) by Liebe (*Liebe, 1981, 1985*; *Liebe and Layton, 1987*; *Liebe et al., 1993*). The radiative transfer model MWMOD uses the 1987 and 1993 versions.

Upon definition of pressure, humidity and temperature the MPM calculates the volume absorption coefficient for water vapour and oxygen. The far wing contributions of high frequency water vapour lines above 1 THz and the continuum absorption of collision induced nitrogen dimers is also parametrized and added to the absorption of the spectral lines. The resulting absorption spectrum between 1 and 250 GHz is shown in Fig. 2.5.

### 3.2.3 Single scattering calculations

The interaction parameters  $\bar{\sigma}_e$ ,  $\bar{\sigma}_a$ , and  $\bar{\mathbf{P}}$  for single hydrometeors may be calculated by three different methods: Spherical particles are generally treated with the Lorenz-Mie (*Mie, 1908*) scattering modul, which is included in the original MWMOD program. For rotationally symmetric particles that have an additional symmetry to their plane of rotation (e.g., spheroids or particles described by only a single Chebyshev polynomial of even order) the extended boundary condition method (EBCM) T-matrix code from Mishchenko is used (*Mishchenko et al., 1996b*). Furthermore, the radiative transfer model was extended to use the Discretized-Mie-Formalism (DMF) developed by Rother and Schmidt (*Rother and Schmidt, 1997*; *Rother, 1998*) for single scattering calculations.

Both single scattering models, the EBCM and the DMF, had to be adjusted for the use in the radiative transfer program. A software interface is used to pass the required input information to the single scattering codes and to obtain the scattering results in return. Extensive tests were made to assure that the results are calculated correctly and within the unit system and coordinate system of the radiative transfer model.

While the T-matrix implementation of Mishchenko in its current form is limited to scatterers having the additional mirror symmetry mentioned above, the DMF is able to handle any rotational symmetric object with a cross section that is given by a unique solution for  $r = r(\theta)$  for each  $\theta$  in the range from zero to 180 degrees. Particle shapes described by Chebyshev polynomials of odd order (as used by *Mugnai and Wiscombe, 1986*) can therefore be treated with the DMF.

Thus the model is able to perform passive microwave radiative transfer calculations which, for the first time, take into account the more realistic shape of raindrops described by a series of Chebyshev polynomials rather than a simpler approximation. For all calculations the rotational axis of the hydrometeors is aligned to the vertical.

The single scattering calculations provide solutions for the ASF (eq. 2.34 on page 22), which relates the scattered electromagnetic wave to the incident plane wave (*Tsang et al., 1985*). From the ASF the interaction parameters are calculated and integrated over azimuth angle, ending up with the appropriate values for one-dimensional radiative transfer. Finally, the results for drops of a certain size and shape are integrated over a



particle size distribution to obtain the polydisperse scattering quantities in each model layer.

The shape definition for the hydrometeors may be one of the following:

- spherical shape
- oblate or prolate spheroid shape (aligned to the vertical) with fixed aspect ratio for particles of all sizes
- oblate spheroid shape with aspect ratio depending on size (according to eq. 3.5)
- Chebyshev shapes depending on size: Series of 10 Chebyshev polynomials, size dependent coefficients interpolated for sizes other than those given in *Chuang and Beard* (1990).

### 3.2.4 Scattering database

The single scattering calculations need to be performed for each combination of frequency, particle size, particle shape, temperature (because of the temperature dependent refractive index), and phase of the water (liquid/frozen). In previous studies the computation time for exact calculations of scattering phase functions with Lorenz-Mie theory was an limiting factor which inhibited/prevented the processing of large data sets with the radiative transfer model.

The computational effort for calculations with the EBCM is two to three (depending on size and nonsphericity) orders of magnitude higher when compared to Mie calculations. The CPU time consumption of the DMF is even higher. In order to achieve insight into the mechanisms of radiative transfer in the presence of nonspherical scattering particles by investigating a variety of different atmospheric conditions it is highly desirable to use pre-calculated results again whenever they match the actual requirements. With such a scheme each combination of parameters is only calculated once and afterwards stored into the scattering database.

The database itself consists of two parts: The data block is a file on a hard disk in which all scattering data (phase matrix, extinction matrix, absorption vector) are stored in the sequence of calculation. Since one single scattering calculation produces some hundred kilobytes of data, the file is far too large to be ordered. Instead of ordering the data, the second part of the database keeps track of the positions of a certain calculation within the data block. This part holds all information that is needed to store data in and retrieve data from the database. It is encoded as an hierarchical tree structure (Fig. 3.4).

The tree consists of nodes in different levels. Any node may have a number of sub-nodes, but only in the following layer. At least one sub-node always exists. One layer of nodes within this tree is provided for each variable that is used to distinguish the single scattering calculations.

When storing data into the database, a parameter vector of 6 numbers that fully determine a calculation is generated. Each layer of nodes is checked against the corresponding value of the parameter vector. If a sub-node with this value exists, this node is followed one level down and the following level is compared. If no matching sub-node is found, such a node is generated and then followed one level down. Upon creation of

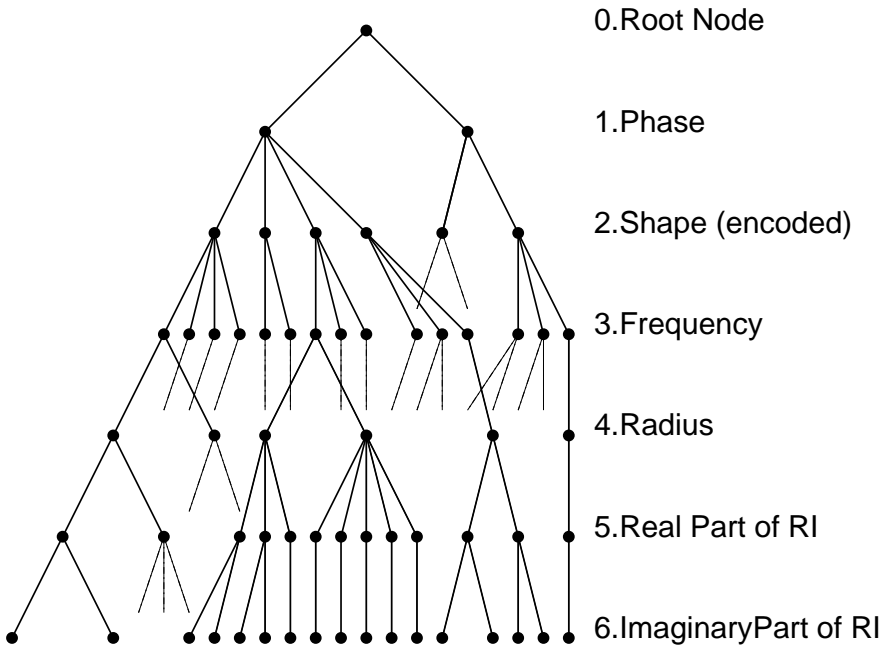


Figure 3.4: *Hierarchical structure of the database information source tree. Each node is represented by a filled dot, the sub-nodes ("childs") of each node are connected to the above node ("parent") by lines. The tree itself is ordered in the meaning that every list of sub-nodes below one node is ordered.*

a new child node the overlaying parent node is reorganized so that it always contains an ordered list of its sub-nodes. When all parameters are checked, the final layer is reached. Final nodes do not contain a list of sub-nodes, but the position of the corresponding data block within the file.

The tree structure is updated whenever new data is added to the database. It may easily be searched for the existence of a scattering calculation with a certain set of parameters. In addition to the prevention of unnecessary repetitions of the same single scattering calculation by looking for exact matches, an interpolating retrieval of data is implemented: If the phase function for particles of a certain size and shape is known for a sufficiently large set of frequencies, the result for an intermediate (and up to now non-existing) frequency can be calculated with sufficient accuracy by interpolating from the nearest neighbours.

The size of the database depends on the number of stored targets and the size of each target itself. The latter is defined by the angular resolution of the single scattering calculations. With an angular discretization of 12 angles for the relative azimuth angle (particles with azimuthal symmetry can be described by one relative azimuth angle  $\Delta\phi$  instead of incident and scattered azimuth angles  $\phi$  and  $\phi'$ ) and 16 angle for the discretization of the zenith angles ( $\theta$  and  $\theta'$ ) each element of the scattering matrix has to be stored 3072 times. With 16 elements in the scattering matrix and 8 Bytes per element the size per scattering matrix easily cumulates to 393216 Bytes. For 10 frequencies, 50 refractive indices, 50 sizes and 5 aspect ratios the database will contain approximately 50 Gigabytes of data.

The access time to this database is limited by the average speed of the hard disk system, but clearly is much faster than single scattering calculations for nonspherical particles. Especially for large particle sizes, frequencies, and aspect ratios the interaction parameters can be supplied a hundred to a thousand times faster by the database system. A standard calculation with 6 different frequencies, 8 different layers of hydrometeors (each with a different refractive index) and 40 different particle sizes in each layer will load 1920 data sets. The entire radiative transfer program (with an angular resolution of 8 zenith angles per hemisphere) consumes 60 seconds CPU time on a DEC Alpha workstation with 333 MHz CPU.

### 3.3 Radiative transfer

The previous steps described in this chapter are the foundations for the solution of the radiative transfer equation. The remaining task is to find a radiation field  $\bar{\mathbf{I}}(\hat{r}, \Omega)$  that solves the VRTE, which itself depends on the spatial position  $\hat{r}$  and the direction  $\Omega = (\theta, \phi)$ .

Since the VRTE is solved with boundary conditions, a non-zero solution ( $\bar{\mathbf{I}} \neq 0$ ) needs to be determined. For the one-dimensional solution any non-zero radiation field  $\bar{\mathbf{I}}(z, \theta)$  that solves the VRTE within a given accuracy will be accepted as the aspired result. The exact way of finding the solution is, aside of numerical efficiency, of no importance to the problem itself.

A variety of algorithms is capable of finding solutions of radiative transfer problems. Problems without scattering can be integrated analytically. The matrix operator method (MOM) is mainly applied to one-dimensional problems (*Liu et al., 1991*) while the discrete ordinates method (DOM) and spherical harmonics DOM (SHDOM) are also applied to three-dimensional problems (*Haferman et al., 1996; Evans and Stephens, 1995a,b*). Monte Carlo methods are used mainly for 3-D modeling (*Liu et al., 1996; Roberti et al., 1994; Roberti, 1997; Roberti and Kummerow, 1999*).

#### 3.3.1 Solving method

The radiative transfer model MWMOD is capable of solving by two methods, an iterative method and the successive order of scattering (SOS) method, which itself is also iterative, but in a different way. Both models start up with the same initialization: Beginning from the top of the atmosphere the downwelling radiation is calculated for all levels. During this initialization the scattering source term is zero, thus the first step gives only the emission and absorption contribution. When reaching the lower boundary, the reflection of downwelling radiation is calculated and added to the surface emission. The upwelling radiation is then calculated for all layers and directions without the scattering source function.

For non-scattering atmospheres this procedure provides the full solution. All other situations need further calculations including the scattering source function. The iterative method calculates the scattering source function by applying the scattering coefficient to the radiation field from the first iteration (the initialization). The second iteration starts again from the top, uses the lower boundary and ends at the upper boundary in exactly

the same way as before, except that the source function resulting from the previous iteration is included. The emission, absorption, and reflection contributions remain the same, but the scattering source term is adjusted after each iteration. After each iteration the new radiation field is compared to its predecessor. If the maximum difference at all layers and all directions is below a certain value, then iterations are stopped and the last radiation field is converted into brightness temperatures by the inverse Planck function and the result written to a file.

In case of the SOS method the iteration scheme is more physically motivated: The emitted radiation from all emitters is used for the first scattering processes and does not need to be re-calculated. The amount of radiation that is scattered after emission is calculated from the initial field as in the iterative method and then distributed through the atmosphere but without the main contribution from the initialization. The resulting radiation field from the second iteration is added to the first result. The following iterations simply calculate the amount of scattered radiation from the previous iteration and add it, after transfer through the atmosphere, to the previous results. So this method simply gives the radiation field which includes the non-scattered radiation and all radiation that had undergone a certain number of scattering processes. In an absorbing environment or a semitransparent medium with open boundary conditions the higher orders of scattered radiation will be smaller than the first ones so that the adjustment of the total radiation field by higher orders gets smaller and smaller. The convergence check is the same as for the truly iterative (or self-consistent) method.

In order to obtain multiple scattering solutions both algorithms use an automatic re-scaling of the vertical grid. The above algorithms assume single scattering within each layer and include multiple scattering by the number of iterations being performed. These algorithms obtain correct multiple scattering results as long as the assumption of single scattering within each layer is correct. The optical thickness resulting from the scattering cross section is a good indicator of the probability for a scattering process taking place in the layer. Because the model MWMOD does not calculate the optical thickness solely from the scattering coefficient the total optical thickness (absorption plus scattering) is used to estimate the probability of scattering. If a single layer has an optical thickness above a threshold the layer is divided into sublayers until the required optical thin state is reached. The threshold value is set to  $\tau = 0.01$  throughout this study. This nadir optical thickness is increased by the slanted path through the atmosphere for angle close to the horizontal. At 85 degrees zenith angle the optical thickness is increased to 0.11, thus the transmission is  $(1/\exp(-\tau)) = 0.896$ . The probability of an extinction process either due to absorption or due to scattering is roughly ten percent at angles closest to the horizontal. Even if this probability is produced only by scattering (in non-absorbing media), the probability of two scattering processes within the layer is only one percent. The single scattering approximation within each optical thin layer treats the scattering in a sufficient way.

### 3.3.2 Examples of convergence

The convergence of the multiple scattering solution is illustrated in Fig. 3.5 by showing the variation of the upwelling TB results with increasing numbers of iterations of the SOS

method. Here, a model atmosphere showing rain below 3 km height, a mixture of rain and ice between 3 and 4 km height and an ice particle layer up to 5 km height was assumed. The rain rate was set to 25 mm/h with a Marshall-Palmer drop size distribution. Sea surface boundary conditions were used as the lower boundary condition.

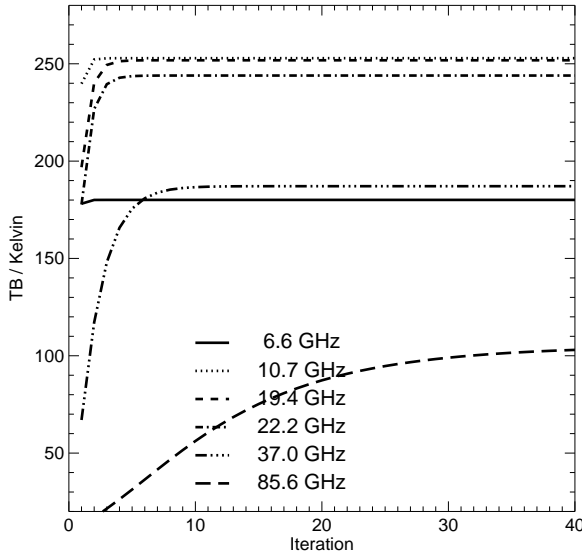


Figure 3.5: *Convergence of brightness temperature (at a zenith angle of 54 degrees) with order of scattering (iteration number).*

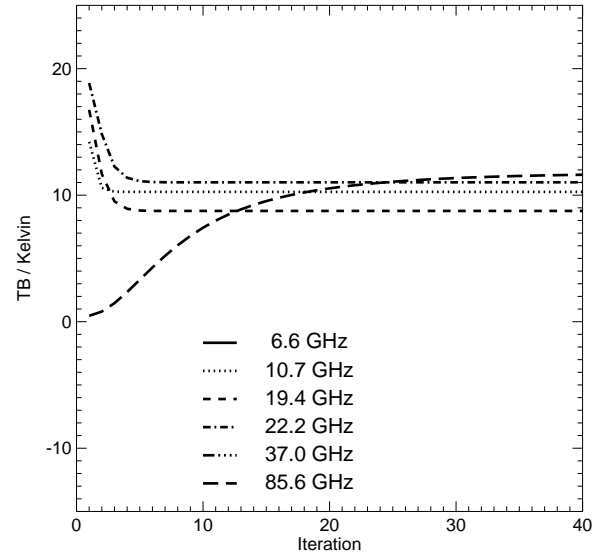


Figure 3.6: *Convergence of polarization difference with iteration number (at a zenith angle of 54 degrees).*

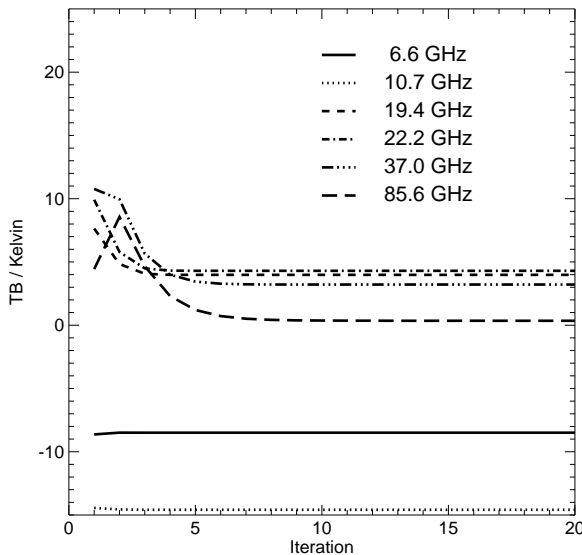


Figure 3.7: *Convergence of polarization difference with iteration number for downwelling radiation at 97 degrees zenith angle (7 degrees elevation angle).*

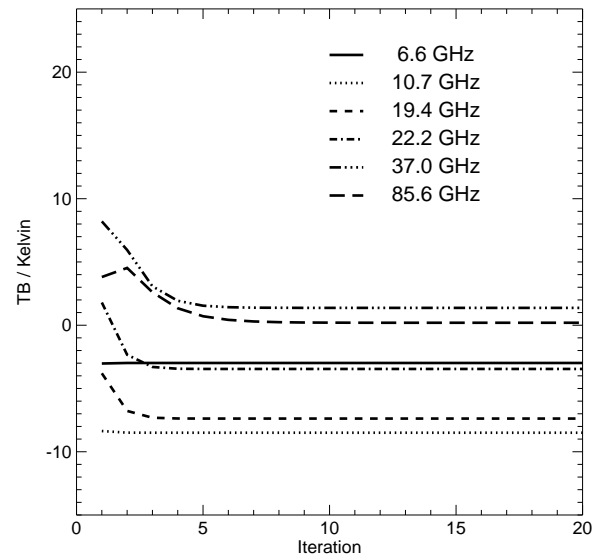


Figure 3.8: *Convergence of polarization difference with iteration number for downwelling radiation at 111 degrees zenith angle (21 degrees elevation angle).*

The self-consistent TB result is reached at small numbers of scattering order for the lower frequencies. At 85 GHz the ice particle scattering is more effective: at least 40 iterations are required to obtain an accuracy better than 1 K.

The polarization signal (Fig. 3.6) shows the same frequency dependence as the brightness temperature. Since hardly any radiation is originating from the polarizing surface, all PD in 85 GHz channel is produced from subsequent scattering processes. At the lower frequency regime the attenuated PD from the sea surface is adjusted to the stable solution within 5 to 8 scattering orders.

The polarization results of the downwelling radiation reveals an interesting feature: At a zenith angle of 97 degrees (7 degree elevation for a ground-based radiometer) the emission by the raindrops itself is polarized (Fig. 3.7). Scattering processes modify this PD signal towards negative polarization differences. Furthermore, the emitted PD signal depends on the observation angle as illustrated in Fig. 3.8 for an elevation angle of 21 degrees. Both, positive and negative values of PD are obtained by the emission of liquid drops depending on frequencies. A detailed discussion on the angular dependence of polarization differences at different frequencies and rain rates is given in section 4.2 on page 44.

## Chapter 4

# Effects of Nonspherical Particles

The modified radiative transfer model is used to analyze the effect of particle shape on the radiation intensity and polarization within the atmosphere. Model atmospheres are defined with different assumptions of hydrometeor shape. Calculations assuming spherical hydrometeors serve as test cases for the results obtained by more realistic nonspherical particle shapes.

### 4.1 Oblate spheroid shape

We assume a very simplified rain event in the lower troposphere. The temperature and humidity profiles are set to a mean midlatitude summer profile. Between 2 km height and ground level a vertically constant rain rate of 20 mm/h is assumed. A water cloud with an LWC of  $0.5 \text{ g/m}^3$  reaches from 1 km up to a cloud top of 3 km. Ice particles are placed above the raining layer to a height of 3 km with the same mass per volume compared to the rain. For both rain and ice particles the Marshall-Palmer DSD is applied by defining the radius of nonspherical particles as the radius of a sphere with equivalent volume.

The approximation of raindrops by oblate spheroids with their rotational axis aligned to the vertical is a very realistic assumption, but applying the same sizes, shapes, and masses to large precipitating ice particles is not meant to be a perfect approximation of the ice particles. Our intention is to investigate the basic effects of ice particle scattering above raining layers. Certainly, the ice particle shapes vary much more than those of water drops but the assumption of oblate particles is still valid. The high amount of ice that we use in this study is rather extreme. For smaller ice masses the signal from the raining layers will be less disturbed by the ice scattering. With the chosen atmospheric setup we are able to understand the fundamental effects of rain and ice particle scattering. More realistic calculations on which retrieval schemes may be set up, need to take into account the specific shapes of ice particles in more detail (e.g., *Evans and Vivekanandan (1990); Turk and Vivekanandan (1995); Evans and Stephens (1995a,b)*). However, even those calculations still do not account for realistic three-dimensional scenarios and therefore still lack the desired degree of highest accuracy.

For reasons of comparison the clear atmosphere (without any hydrometeors) and the cloudy atmosphere (only the water cloud) are calculated as test cases. Radiative transfer results of the rainy atmosphere are calculated in the presence of the ice particle layer

Table 4.1: *Definition of test cases. All cases include a water cloud between 1 and 3 km height with an altitude constant LWC of  $0.5 \text{ kg/m}^3$  and a MGD particle size spectrum with a modal radius of  $5.5 \mu\text{m}$ . The raining layer is positioned between 0 and 2 km height, the ice particle layer starts at 2 km and ends at 3 km.*

Name of case	Shape of Raindrops	Shape of Ice Particles
A	Spheres	(No Ice Particles)
B	Oblate Spheroids	(No Ice Particles)
AC	Spheres	Spheres
AD	Spheres	Oblate Spheroids
BC	Oblate Spheroids	Spheres
BD	Oblate Spheroids	Oblate Spheroids

and without. Table 4.1 defines the different atmospheric states that are modeled. The water cloud is always present in the six precipitating cases and modeled with spherical particles.

The following situations were calculated for the hydrometeor shapes: (A) spherical raindrops only, (B) oblate raindrops only, (AC) spherical raindrops and spherical ice particles, (AD) spherical raindrops and oblate ice particles, (BC) oblate raindrops and spherical ice particles, (BD) oblate raindrops and oblate ice particles.

All six situations were calculated for two different surface conditions with a varying rain rate between 0 and 100 mm/h. Using the surface emissivity  $\epsilon = 1.0$  assumes a perfect blackbody and results in a unpolarized but dominant emission from the bottom of the atmosphere. It allows to study the polarization effects of the hydrometeors without polarization effects by the surface. This situation of strong upwelling radiation interacting with hydrometeors is an approximation to land surfaces. Alternatively, the frequency dependent reflection of a water surface is used to study the polarization effects in the presence of large PD from surface emission.

## 4.2 Angular dependence

The variation of total intensity with zenith angle is shown as an example in Fig. 4.1a for a rain rate of 20 mm/h and  $\epsilon = 1.0$ . At zero angle the radiation is emerging straight upward for nadir observation. The opposite direction ( $180^\circ$ ) is the uplooking geometry for downwelling radiation. The horizontal direction ( $90^\circ$ ) is undefined for the one dimensional model: In a plane parallel medium with no boundaries at the sides the geometric path through the layer and therefore also the optical thickness tends to become infinitely large as the direction approaches the horizontal. For upward directions  $T_B$  is taken from the top of the model atmosphere (TOA, which is 15 km in this case), for downward directions



$T_B$  is taken at ground level (bottom of the atmosphere, BOA).

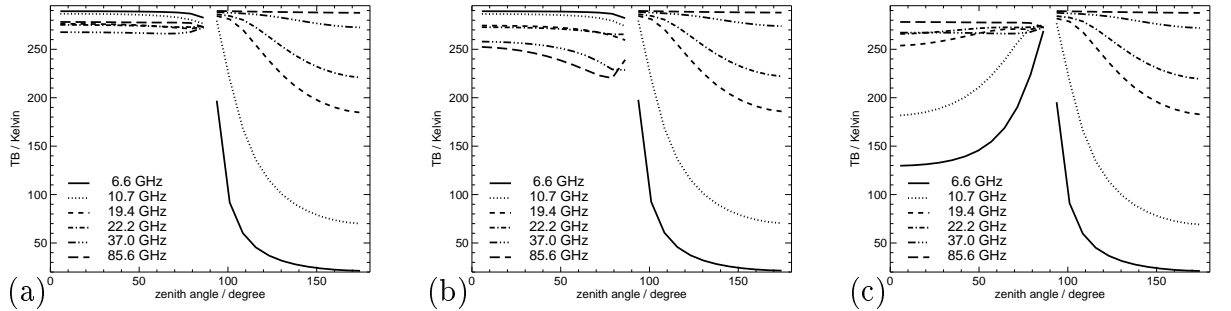


Figure 4.1: Total intensity versus zenith angle of propagation at different frequencies for 20 mm/h rain rate for different situations: (a) case B, emissivity is set to  $\epsilon = 1.0$ , (b) case BD,  $\epsilon = 1.0$ , (c) case B, but with polarizing sea surface below. The upwelling radiation (angles 0 to 90 degree) is taken at the top of the atmosphere, downwelling radiation (90 to 180 degree propagation direction) at the bottom of the atmosphere.

When observing the atmosphere from above (angles  $0^\circ$  to  $90^\circ$  in Fig. 4.1a, the main contribution is the thermal emission from the surface. With increasing opacity to higher frequencies the radiation originates from higher layers of the atmosphere, leading to reduced  $T_B$  results.

At downward directions (angles  $90^\circ$  to  $180^\circ$  in Fig. 4.1) the atmosphere is mostly transparent for the lower four frequencies even with a 2 km thick rain layer. Due to the minimal signal from space and only small contributions from the atmosphere, the resulting  $T_B$  remains rather cold. At 37.0 GHz and 85.6 GHz the atmosphere starts to become opaque and produces increasing  $T_B$ .

Adding a further precipitating layer with ice particles of the equivalent hail rate from 2 km to 3 km height (case BD) leaves the results at downward directions nearly unchanged. Only the upwelling radiation is affected by the well known brightness temperature depression (Fig. 4.1b) due to scattering, showing the highest efficiency for 85 GHz.

Figure 4.1c shows the effect of sea surface emission at the lower boundary by a Fresnel surface using the refractive index of water according to the parametrization of *Ulabiy et al.* (1986): the averaged emission is significantly smaller than one, leading to lower brightness temperatures at upward directions. For long optical path lengths (at angles close to the horizontal) and at higher frequencies the atmosphere becomes opaque enough to reach higher  $T_B$  close to the physical temperature of the surface.

The distribution of intensity with direction for 37 GHz and  $\epsilon = 0$  is given in Fig. 4.2. Previous investigations (e.g., *Liu and Simmer* (1996); *Czekala and Simmer* (1998)) have shown that polarization effects caused by hydrometeors require a non-isotropic distribution of intensity with zenith angle. This situation is given when either the surface emission depends on direction or the total intensity is dominated by the atmospheric emission. The latter is directly linked to the line of sight total optical thickness which itself depends on direction. We can observe from Fig. 4.2 that much more radiation is propagating upward than in the opposite direction. The resulting PD is given in Fig. 4.3.

It is clear from Fig. 4.3 that the PD originates from within the precipitation layer. At downward directions close to the horizontal, especially at lower layers where humidity

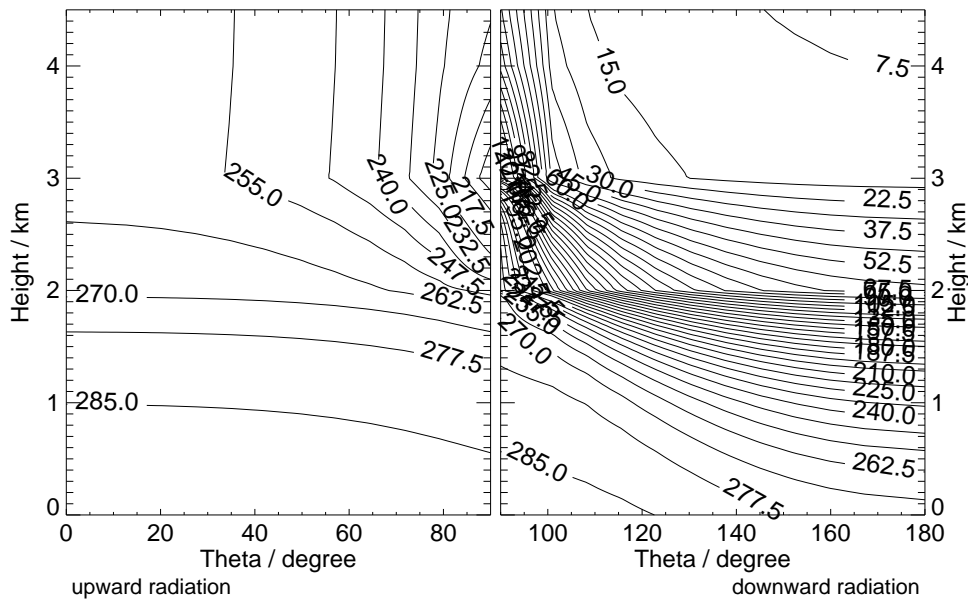


Figure 4.2: *Brightness temperature for 37 GHz (case BD,  $\epsilon = 1.0$ ) versus zenith angle and vertical position. The rain layer with 20 mm/h rain rate reaches up to 2 km height, the ice layer is placed between 2 km and 3 km.*

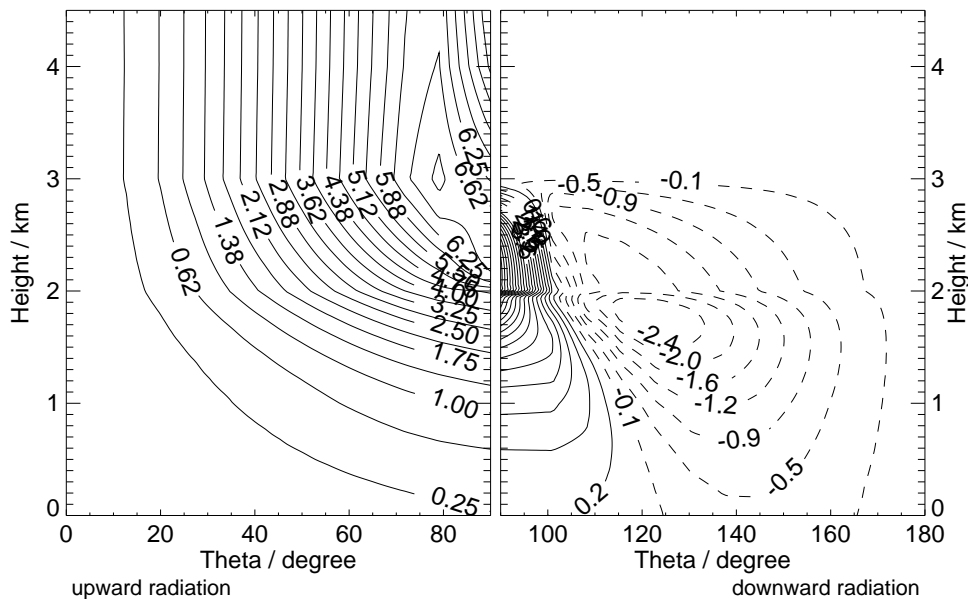


Figure 4.3: *Polarization difference (corresponding to Fig. 4.2).*

and temperature are higher, the optical thickness is increased and the PD changes from negative to positive values, very similar to those at upward directions.

Figure 4.4 gives the resulting PD from four calculations with 20 mm/h rain rate and blackbody surface emission ( $\epsilon = 1.0$ ). The atmospheric conditions are set to the cases A, B, AC, BD, respectively (Table 4.1). The most evident feature for nonspherical particle shapes (cases B and BD) is the negative PD at downward directions. This feature may have large impacts on ground-based observations; the details have been discussed elsewhere (Czekala and Simmer, 1998).

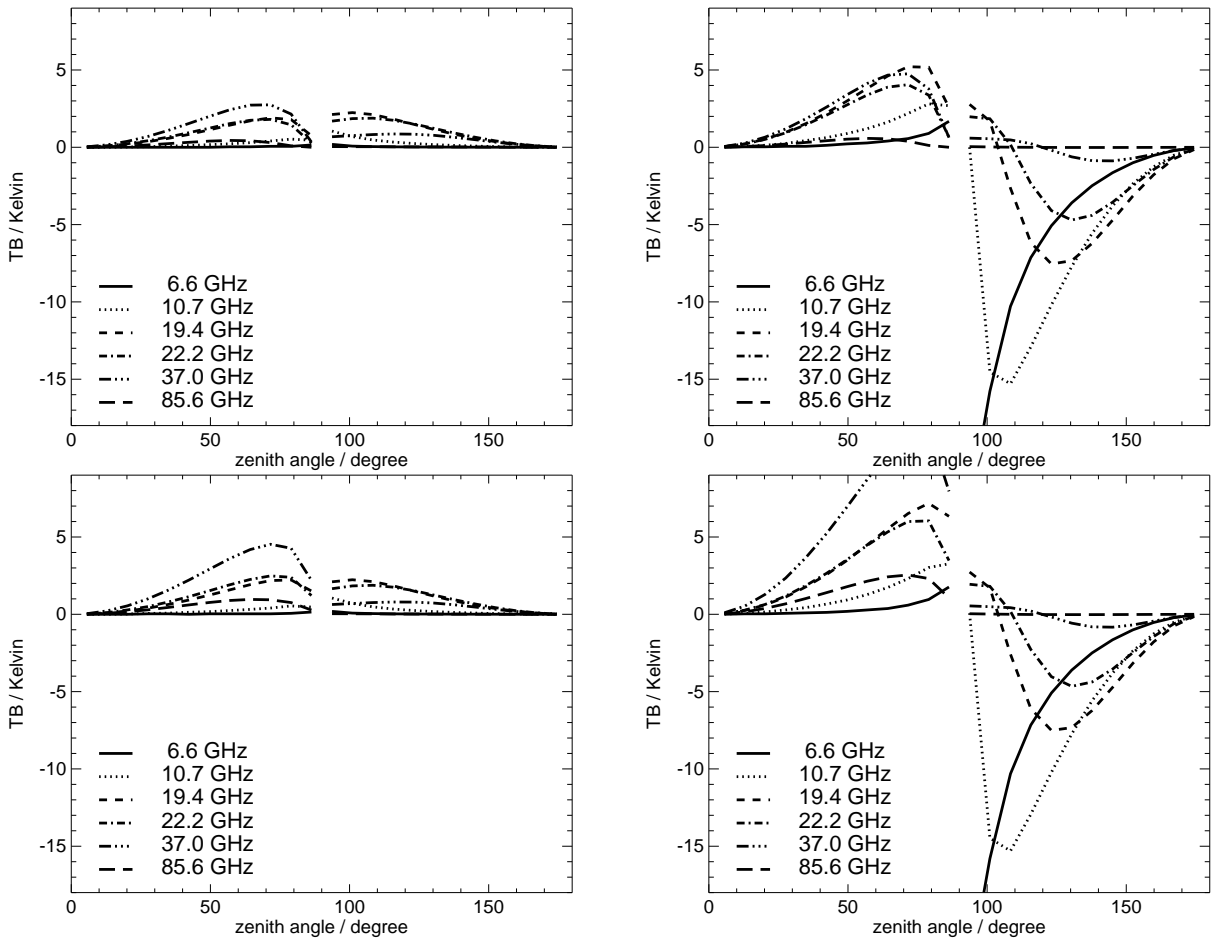


Figure 4.4: Angular dependence of PD for case A (upper left), B (upper right), AC (lower left) and BD (lower right).

The PD an airborne sensor would observe is positive, but smallest for the spherical rain without ice (case A, Fig. 4.4). Oblate raindrops result in an enhanced PD, especially for the 19 and 22 GHz channels (case B, Fig. 4.4). The 37 GHz channel is less affected by switching from spherical to nonspherical shape, but exhibits the strongest polarization features above pure rain layers without ice. Adding ice particles increases the positive PD for spherical particles (case AC, Fig. 4.4), but this behaviour is still stronger for oblate ice particles (case BD, Fig. 4.4) than for spherical ones. Polarization due to ice particle scattering is most efficient at 37 GHz, regardless of the exact shape.

The observed PD increases with zenith angle until the atmosphere becomes opaque near the horizontal direction. This point of saturation and decreasing PD is reached at smaller zenith angle for the higher frequencies, with no saturation at all for 6.6 and 10.7 GHz.

A closer look at the difference of two calculations with 20 mm/h rain rate, one using oblate shapes for both, liquid and frozen particles, the other one using oblate ice particles but spherical raindrops, clearly shows that the PD originating from the liquid hydrometeors can be seen from above through the layer of ice particles (Fig. 4.5). The effect is very close to the difference of oblate and spherical particles in the absence of the ice

layer, pointing out the necessity of taking the shape of raindrops into account.

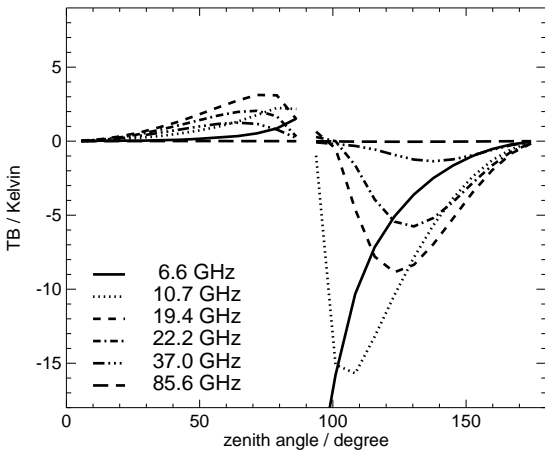


Figure 4.5: *Change in PD when using oblate shape for both phases instead of spherical rain and oblate ice particles (case BD minus AD).*

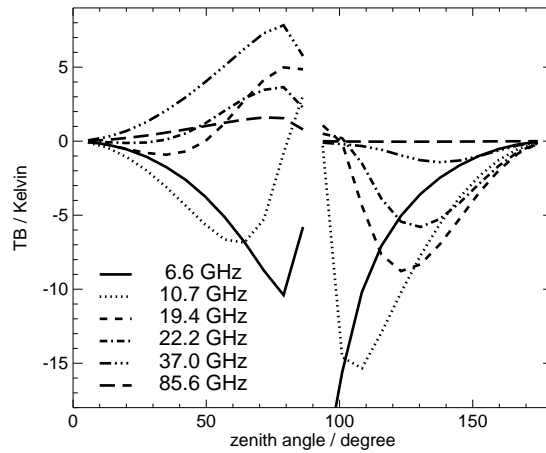


Figure 4.6: *Change in PD (cases BD minus AC) when using oblate shapes for both phases instead of spheres for both. The rain rate is set to 20 mm/h (as in all previous figures), but the surface emissivity is set to Fresnel reflection.*

By switching the surface emissivity to sea surface conditions the observed PD at upward directions is dominated by the linear polarization caused by the Brewster angle for Fresnel surfaces. This effect produces up to 60 K PD for 10.7 GHz and will not fully be damped by the above rain mass. However, the increase of PD by rain and ice layers is still observable in the difference plot (Fig. 4.6) of the realistic shapes (case BD, both phases with oblate particles) and the simplified assumption (case AC, both phases modeled as spheres). This change in PD is originating from the changed intensity distribution caused by the lowered emissivity of the surface, for these changes are very similar in behaviour to those obtained by a non-polarizing surface at  $\epsilon = 0.5$ .

### 4.3 Rain rate dependence

The above results were calculated with a fixed rain rate of 20 mm/h. Obviously, the observed  $T_B$  and PD will depend on rain rate. Figure 4.7 gives the PD produced by a liquid rain layer (case B) above a blackbody emitting surface for different frequencies versus the rain rate. Unless otherwise mentioned, the zenith angle is set to 56 degrees, which is close to the SSM/I observing angle. The linear polarization produced by liquid raindrops over a non-polarizing surface increases strongest for the 37 GHz frequency, but saturates at low rain rates. Due to the higher transparency the PD signal of the less sensitive lower frequencies continues to increase at higher rain rates. At 85 GHz the atmosphere is nearly opaque. Radiation emerging from the rain layer at upward directions most likely is absorbed before leaving the rain layer. If radiation escapes the area of high optical thickness without being absorbed, then the probability of a scattering process is minimal since the scattering albedo of liquid raindrops at 85 GHz is very small.

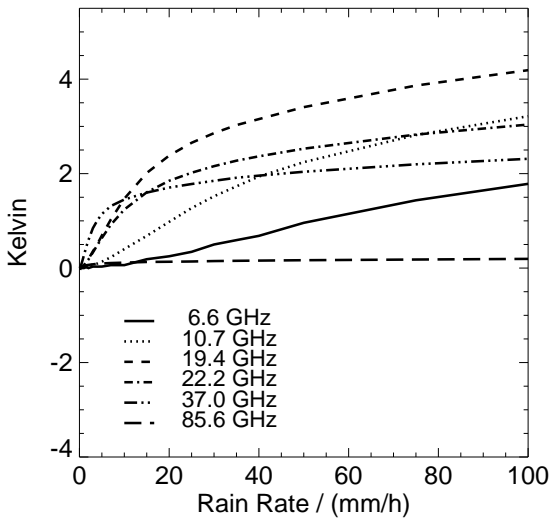


Figure 4.7: *PD versus rain rate for different frequencies (case B, rain layer with oblate spheroids).*

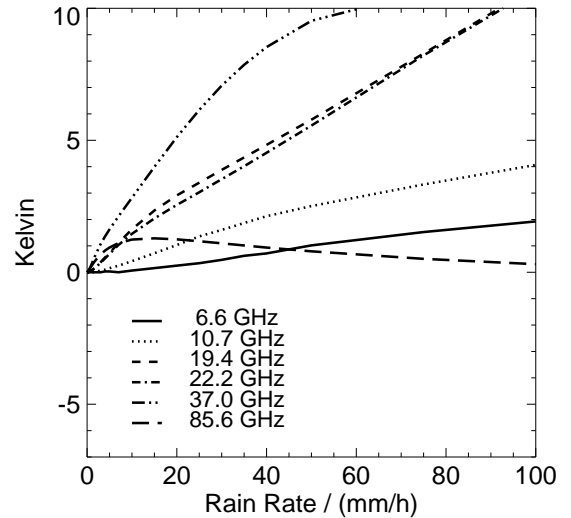


Figure 4.8: *Change in PD versus rain rate when using oblate raindrops and ice particles instead of spheres for both (case BD minus AC).*

The difference of PD calculated with realistic rain and ice on the one hand and spherical particles on the other hand also varies with rain rate (Fig. 4.8). The difference is highest for 22 and 37 GHz when assuming spherical hydrometeors. This forces us to model the hydrometeors shape accurately since the PD induced by the precipitation is also strongest at 22 and 37 GHz. A small amount of linear polarization is induced by ice particles at 85 GHz. The small absorption and high scattering efficiency for ice particles enables scattering effects for this high frequency. However, the PD signal at 85 GHz depends very much on the selected size and shape distribution of the hydrometeors. Assuming larger sizes and aspect ratios together with lower particle density for a simulation of large snowflakes will lead to much larger PD signals at 85 GHz with only small effects around 20 GHz, since the low frequencies are most sensitive to liquid water and only have a small scattering efficiency for ice particles.

Above sea surfaces the total PD is dominated at low rain rates by the surface induced polarization (Fig. 4.9). With increasing rain rate the atmosphere becomes opaque and the PD is damped. After saturation, when no PD from the surface is reaching the cloud top, we observe an increasing PD. This polarization is induced by scattering on nonspherical hydrometeors of both phases, liquid and frozen. At 25 mm/h rain rate the 37 GHz channel receives 10 K PD with a saturation around 15 K.

Finally, the changes in PD calculated by using the oblate shapes instead of the spherical shapes over water surfaces are much more complicated than in the case of perfect blackbody emission (Fig. 4.10).

At small rain rates the spherical calculation will overestimate the PD. This happens because the nonspherical particles produce negative PF in a situation where the intensity distribution is very non-isotropic. This negative PD leads to a decrease of the large positive PD from the surface. Spherical scattering particles will not produce this negative fraction of PD and therefore result in higher values.

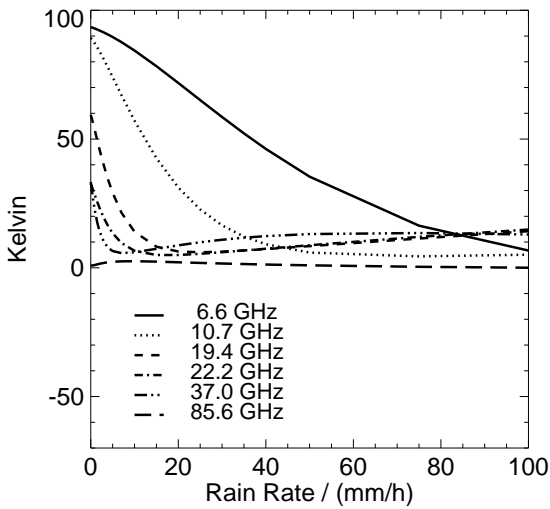


Figure 4.9: *PD versus rain rate over water surface. Oblate raindrops and oblate ice particles are used (case BD).*

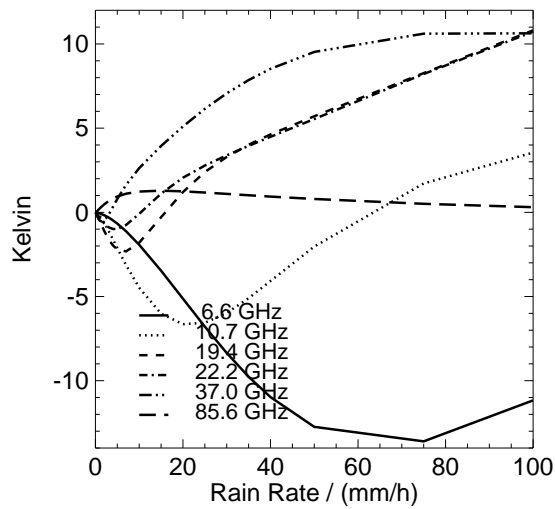


Figure 4.10: *Change in PD versus rain rate when using oblate raindrops and ice particles instead of spheres for both (case BD minus AC, similar to Fig. 4.8, but with sea surface emission).*

With increasing rain rate the atmosphere becomes opaque, the intensity distribution becomes more isotropic and the negative PD caused by nonspherical particles changes to positive values. This point is reached at lower rain rates for higher frequencies. Further increase of rain rate makes the surface invisible from above. The only resulting PD (at frequencies above 10.7 GHz) is coming from the raining layers. In this situation the nonspherical particles polarize the radiation more efficiently than spheres. Calculations neglecting the aspherical shape will underestimate the PD.

## 4.4 Sensitivity to drop size

The polarization effects due to nonspherical raindrops exhibit the surprising feature of being very sensitive to the lower frequencies, especially 22 and 37 GHz. Investigations on the sensitivity of radiative transfer result on the maximum size of particles in the DSD reveal the reason for this behaviour.

The variation of TB as a function of the maximum drop radius which is used as the upper limit of the integral over the particle size distribution is shown in Figure 4.11. The total water mass is left unchanged by adjusting the total drop numbers, the rain rate is set to 20 mm/h with a rain layer of oblate rain drops only (similar to case B, but with a humidity profile that contains less moisture). The surface emissivity is set to  $\epsilon = 1.0$ .

Figure 4.12 gives the difference of oblate drops minus spherical drops. The corresponding PD for oblate drops and the difference to spherical shape is given in Figs. 4.13 and 4.14, respectively.

The lowest frequency (6.6 GHz) is insensitive to particle size (Figs. 4.11 and 4.13). With increasing frequency the sensitivity rises, but saturation effects are reached at

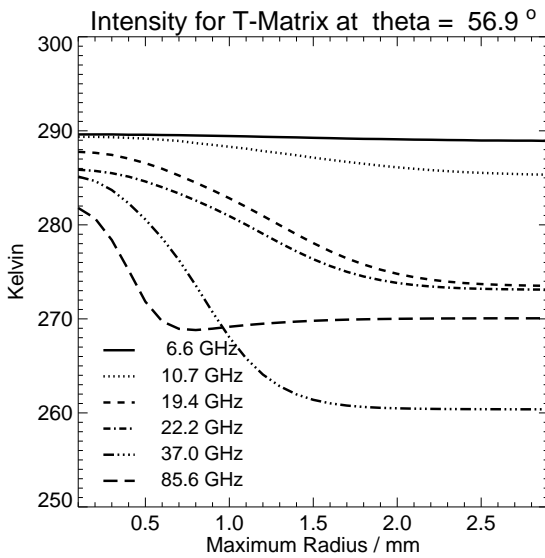


Figure 4.11: *Change in brightness temperatures (using spheroid particles and a zenith angle of 56 degrees) as a function of maximum radius in the DSD integration (for details see text).*

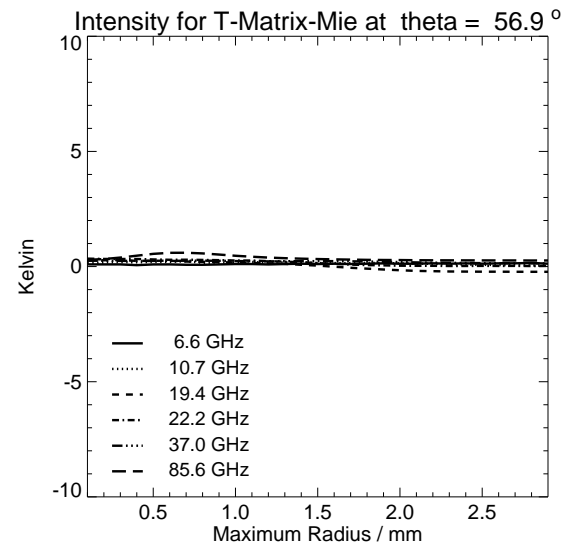


Figure 4.12: *Difference of brightness temperatures obtained by different drop shapes (spheroids minus spheres) as a function of maximum radius in the DSD integration (using a zenith angle of 56 degrees).*

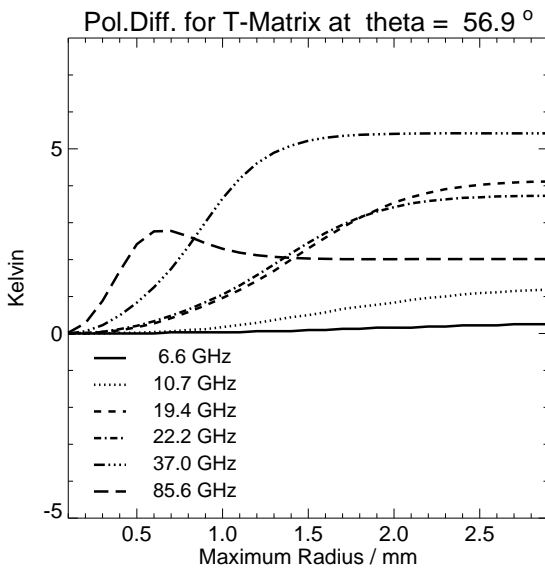


Figure 4.13: *Change in polarization differences (using spheroid particles) as a function of maximum radius in the DSD integration (using a zenith angle of 56 degrees).*

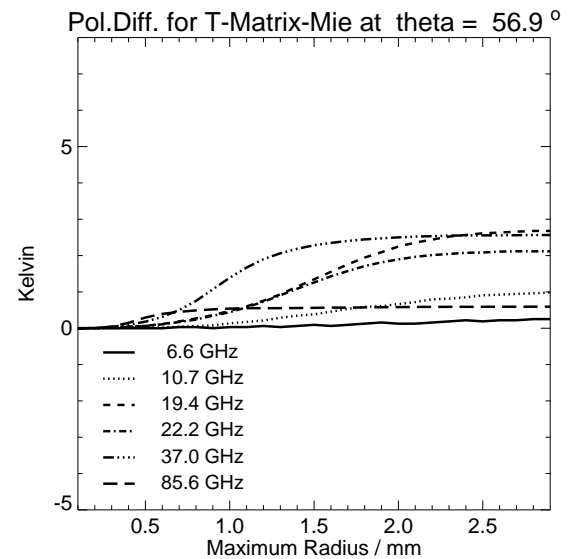


Figure 4.14: *Difference of polarization differences obtained by different drop shapes (spheroids minus spheres) as a function of maximum radius in the DSD integration (using a zenith angle of 56 degrees).*

smaller drop sizes for 37 and 85 GHz. The PD result for 85 GHz is unaffected by drops larger than 2 mm diameter, but this is the drop size where significant distortion from spherical shapes begins.

While the differences in TB are small for all frequencies (Fig. 4.12), the differences for PD are significant (Fig. 4.14). The additional PD caused by nonsphericity depends on the particle sizes, and again the 85 GHz and 37 GHz channels are insensitive to particles above 2 and 3 mm diameter while the signals around 20 GHz are still influenced by drops of 4 mm diameter.

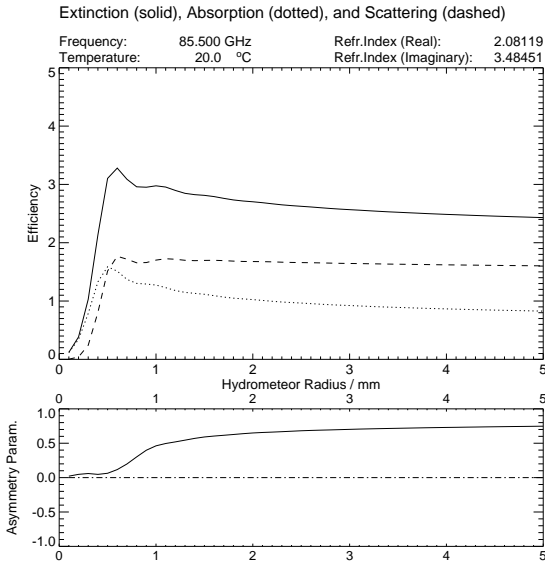


Figure 4.15: *Scattering, absorption, extinction efficiencies (dashed, dotted, and solid) and asymmetry parameter for DSD at 85 GHz.*

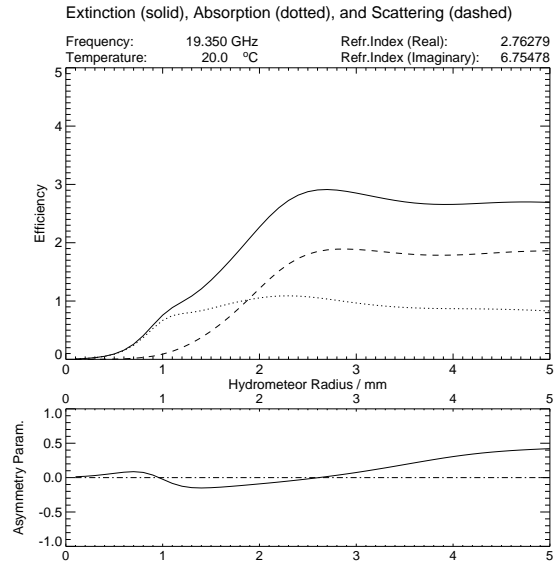


Figure 4.16: *Scattering, absorption, extinction efficiencies (dashed, dotted, and solid) and asymmetry parameter for DSD at 19 GHz.*

The reason for this insensitivity to large water drops for 85 GHz is found in the high absorption coefficient of microwaves for water. The absorption is large for all frequencies, but the size of the particles (measured in wavelength units of the considered frequency) is four times larger at 85 GHz compared to 22 GHz. This leads to a smoothed curve of scattering and absorption efficiency (which is the total absorption coefficient normalized with the particles geometric cross section, defined by the volume equivalent radius) that reaches its maximum at small drop sizes (Fig. 4.15). For large particles the extinction efficiency approaches the optical limit of 2, which means that the extinction in a beam of light by a particle is twice its geometric cross section (e.g., *van de Hulst*, 1981).

At 19 GHz (Fig. 4.16) the situation is different: The efficiencies are still increasing up to drop diameters of 5 mm. Looking at the interaction parameters for 19 GHz we clearly see the difference between both frequencies. The asymmetry parameter, describing the balance of forward and back scattering, rises around 1 mm radius for 85 GHz to its maximum. So all scattering effects by larger drops will only be seen in the forward direction.

Due to the larger wavelength of 19 GHz, the asymmetry parameter stays around zero (indicating equal amounts of scattered intensity in both directions). It even drops below zero (indicating backscattering) because of the high refractive index of 6.8, which causes large phaseshifts of internal and external fields, resulting in resonant scattering behaviour



(*Deirmendjian*, 1969). This makes small frequencies very sensitive to backscattered radiation from a non-isotropic radiation distribution, as it is found in an atmosphere with weak surface emission.

## 4.5 Comparison of different shape approximations

The following calculations are dealing with the question how specific or realistic the shape description of a hydrometeor should be.

For the calculations we used an atmospheric rain layer between the surface and 2 km height with 3 layers of different temperature. The polydisperse interaction parameters are computed with a Marshall-Palmer drop size distribution for a constant rain rate of 25 mm/h (*Marshall and Palmer*, 1948). Some calculations have an additional layer of large, precipitating hail above the rain layer, reaching from 2 km to 3 km. The aim of this atmospheric setup is to model realistic raindrop scattering on one hand and the possible screening of these results by a hail layer above the rain on the other hand. The purpose of the ice layer is not to model real thunderstorm conditions, but to study the principle radiative transfer effects of such ice particle layers. For such a rough estimation the exact microphysical parameters are of minor importance; basic processes can be understood with these simple model assumptions. The size and shape distributions of the hail are not meant to be realistic in any other way than to produce a strong scattering signal: The nonspherical ice particles will lead to high polarization and depolarization efficiencies which modify the upwelling radiation emerging from the rain.

In order to determine the ice particle contribution to the total signal the hail layer is calculated without the underlying rain layer. The comparison of the results for rain (without ice), ice (without rain), and rain (with ice) allows to estimate the screening effect of ice particles above rain layers. The results clearly state that the polarization signal produced by nonspherical raindrops emerges to the top of the atmosphere without being substantially attenuated by ice particle layers.

Surface boundary effects were examined by using three different surface conditions: blackbody boundary condition ( $\epsilon = 1.0$ ), sea surface boundary (using Fresnel reflection) and a fixed emissivity of  $\epsilon = 0.5$  (Lambertian surface). The latter case gives an enhanced angular variation of the radiation in the lower layers due to the reduced emissivity, which is very similar to the sea surface emission, but does not polarize the surface emission. This is useful for a separation between polarization effects that originate from either the highly polarized emission of a Fresnel surface or from the angular distribution of the intensity.

### 4.5.1 Intensity results

An example of the total radiation intensity (the sum of vertically ( $I_v$ ) and horizontally ( $I_h$ ) polarized intensity), expressed in terms of equivalent blackbody brightness temperatures, versus zenith angle of propagation is given in Fig. 4.17. Zero angle is the direction of upwelling radiation at nadir direction. At the horizontal direction (90 degrees) the one-dimensional model is not defined.

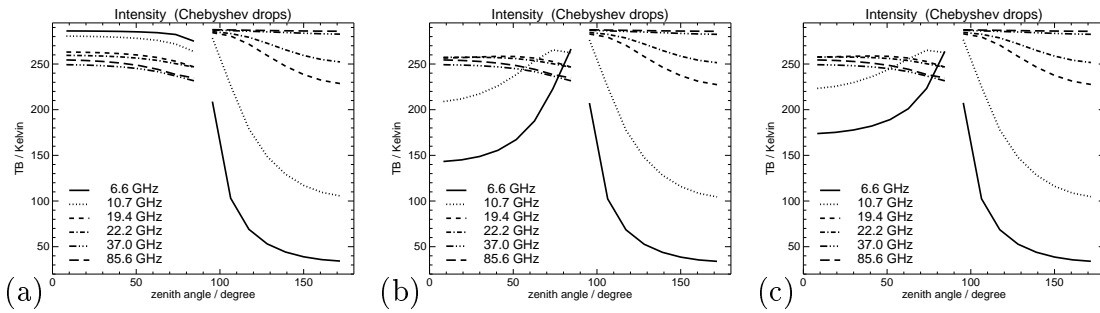


Figure 4.17: *Brightness temperature vs zenith angle of propagation for six frequencies at 25 mm/h rain rate (no ice particles) and three different surface conditions: (a) blackbody emission ( $\epsilon = 1.0$ ), (b) sea surface (Fresnel), (c) lowered emissivity ( $\epsilon = 0.5$ , Lambertian surface).*

The upwelling radiation at the high frequencies (37 and 85 GHz), which reaches high opacities at 25 mm/h rain rate, is nearly unaffected by changes in the surface emission. The radiances are mostly determined by the temperature of the top of the raining layer. In the low frequency regime the opacity is much lower, so that the reduced emissivities (polarized in Fig. 4.17b and unpolarized in Fig. 4.17c) lessen the nadir upwelling radiation. At angles close to the horizontal the path integrated optical thickness rises, leading to a saturation of the brightness temperatures at the physical temperature. Downwelling radiation results show the effect of optical thickness much stronger: At 85 GHz the radiation that can be observed at the bottom of the atmosphere comes only from the lowest rain layers, leading to the highest brightness temperatures. At the lowest frequency of 6.6 GHz the atmosphere is very transparent resulting in a low emission by the atmosphere in addition to the cold background from space.

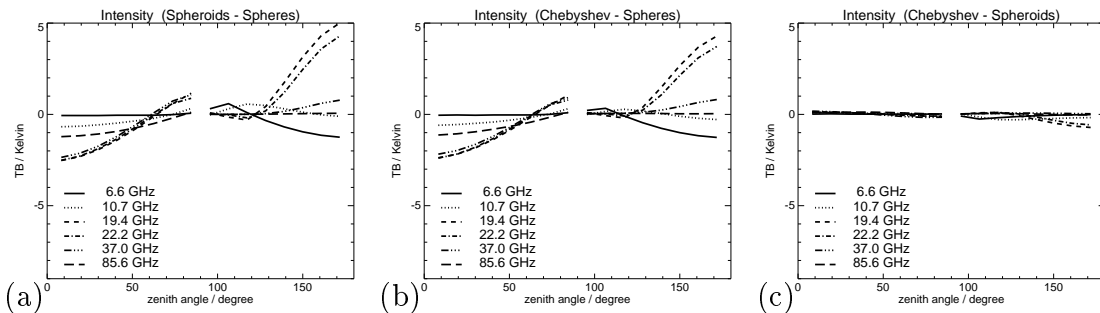


Figure 4.18: *Brightness temperature differences vs zenith angle (rain only and blackbody emission at the surface): (a) Spheroids minus Spheres, (b) Chebyshev drops minus spheres, (c) Chebyshev drops minus spheroids.*

Figure 4.18 shows the differences of calculations obtained by the three different assumptions on particle shape. A raining layer of oriented oblate particles (spheroids or Chebyshev drops) produces more radiation in downward directions and less radiation in upward directions (Figs. 4.18a and 4.18b). Since the results calculated with blackbody emission and fixed orientation of the particle are strongest for the low frequencies (22 and 37 GHz), this result indicates enhanced backscattering or emission for oblate particles

compared to spheres. However, the difference between the spheroid approximation and the more realistic Chebyshev drops is minimal.

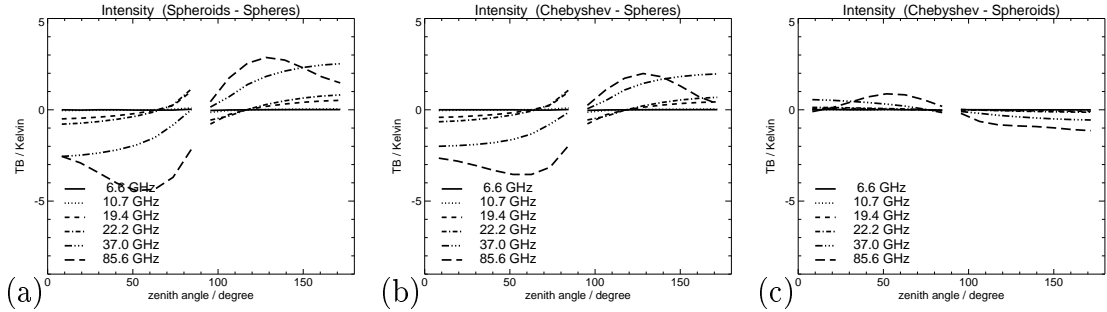


Figure 4.19: All settings as in Fig. 4.18, but with the ice particle layer only (no rain).

When considering only ice particle scattering (isolated from the corresponding rain layer), Fig. 4.19 clearly shows that the basic effect is the same, but this time more pronounced for larger frequencies. The 37 and especially the 85 GHz channel, which were very insensitive to the change of shapes for rain, exhibit remarkable changes of the intensity. At the latter frequency the spheroid shape suppresses additional 5 K of the upwelling radiation compared to spheres. The difference of the two oblate shapes (Chebyshev minus spheroids, Fig. 4.19c) states that the Chebyshev shaped particles lead to smaller changes in comparison to spheres.

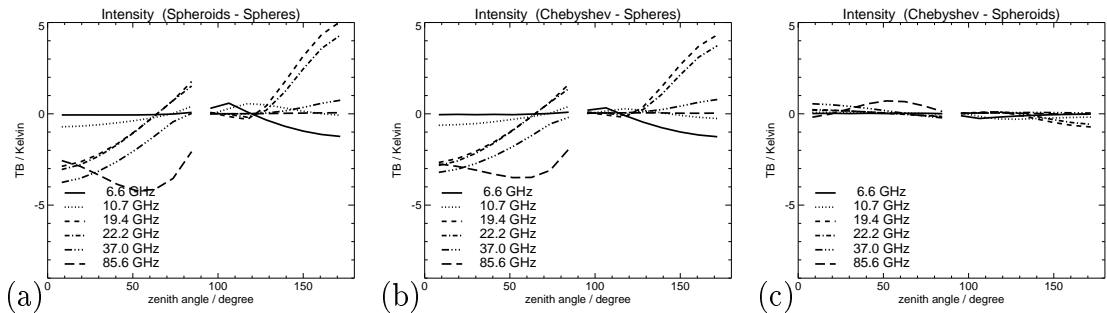


Figure 4.20: All settings as in Fig. 4.18, but with the ice particle layer additional to the rain layer (both layers present).

Combining rain and ice layer in one calculation (Fig. 4.20) straightforward gives a 'mean' result from the single cases of Fig. 4.18 and Fig. 4.19. At upward directions the resulting differences for the low frequencies are fully determined by the raining layer and are not affected by ice particle scattering above. The opposite is true for 85 GHz, which has a significant sensitivity to ice particle scattering only. This separation of high and low frequencies is more difficult at 37 GHz, where the effects of both hydrometeor phases have an impact on the signal. The downwelling radiation is nearly the same as in the case of rain only because most of this radiation is emitted by the rain itself and may only interact with the liquid phase hydrometeors on the path to the surface. Again, the differences between the spheroid shape and Chebyshev drops (Fig. 4.20c) are very small, giving a similar result as in the case of ice scattering only.

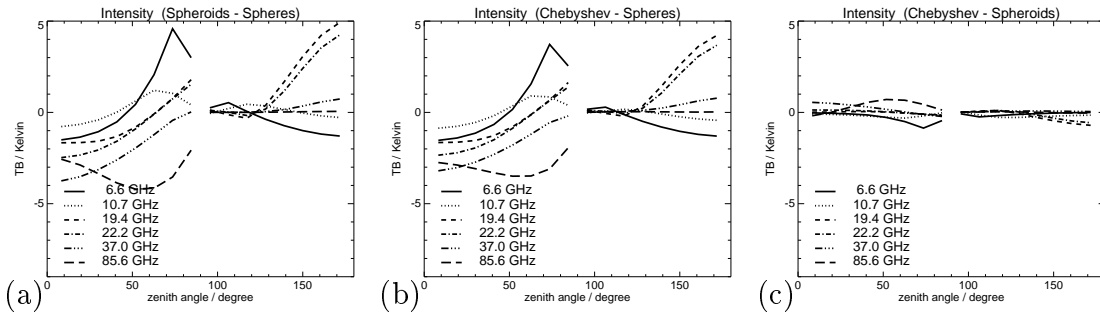


Figure 4.21: All settings as in Fig. 4.20 (both layers, rain and ice), but with sea surface conditions at the lower boundary.

These results indicate a sensitivity of the low frequencies to changes in surface emission. Figure 4.21 gives the results for the combination of rain and ice layer (as in Fig. 4.20), but with an underlying sea surface with reflection and emission according to Fresnel instead of a blackbody source. While the downwelling radiation is unaffected, there is a change for those frequencies with small opacity which are able to see the surface from above the atmosphere. The channels at 6.6 and 10.7 GHz, which were both nearly unaffected by changes of particle shape in case of blackbody boundary conditions, now show larger differences, reaching from negative values ( $-1.5$  K) to positive values ( $+5$  K) depending on the angle.

## 4.5.2 Polarization results

The effect of scattering by hydrometeors is known to be twofold: On the one hand the highly polarized radiation emanating from the sea surface is depolarized by the hydrometeors, and on the other hand unpolarized radiation is polarized by the interaction process with liquid and frozen particles. The variable best suited for remote sensing purposes is the polarization difference (PD), which is defined as difference of vertically and horizontally polarized brightness temperature ( $PD = T_{B,v} - T_{B,h}$ ). The total PD hence originates from two sources, which are the effects of hydrometeors on the one hand and the polarized emission by sea surface on the other hand.

Figure 4.22 gives the resulting PD in case of the raining layer above three different surface types. While Fig. 4.22a and Fig. 4.22c include a non-polarizing surface, Fig. 4.22b shows the high amount of linear polarization close to the Brewster angle for the low frequencies. Note that these large PD values for a nearly transparent atmosphere (at frequencies of 6.6 and 10.7 GHz and 25 mm/h rain rate) are not connected to the hydrometeor shape, so that the results have been clipped.

The effect of surface PD can be eliminated by subtracting calculations performed with spherical particles from those with Chebyshev drop shapes (Fig. 4.23). The PD of the upwelling radiation at low frequencies and blackbody surface emission (Fig. 4.23a) differs from the two surface conditions with a lower emissivity. These two calculations (Fig. 4.23b and Fig. 4.23c) have similar emissivities, but completely different polarization features. However, the resulting PD matches almost perfectly.

The comparison of the different shapes is done in Fig. 4.24, restricting the results to

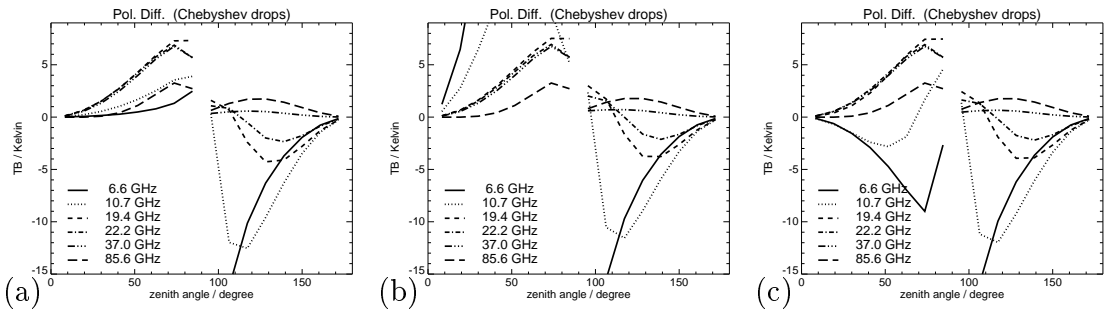


Figure 4.22: *PD vs zenith angle of propagation for six frequencies at 25 mm/h rain rate (no ice particles) and three different surface conditions: (a) blackbody emission ( $\epsilon = 1.0$ ), (b) sea surface (Fresnel), (c) lowered emissivity ( $\epsilon = 0.5$ ). Note that the large PD values in (b) for a nearly transparent atmosphere are not connected to the hydrometeor shape, so that the results have been clipped.*

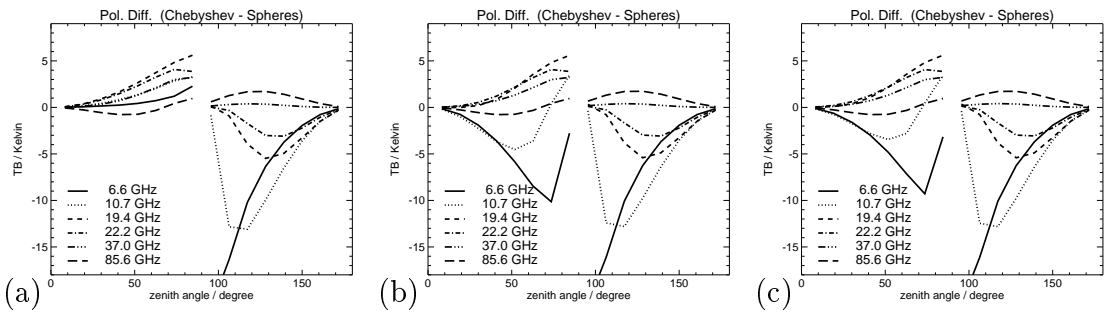


Figure 4.23: *Difference of PD (Chebyshev drops minus spheres) vs zenith angle of propagation for three different surface conditions: (a) blackbody emission ( $\epsilon = 1.0$ ), (b) sea surface (Fresnel), (c) lowered emissivity ( $\epsilon = 0.5$ ).*

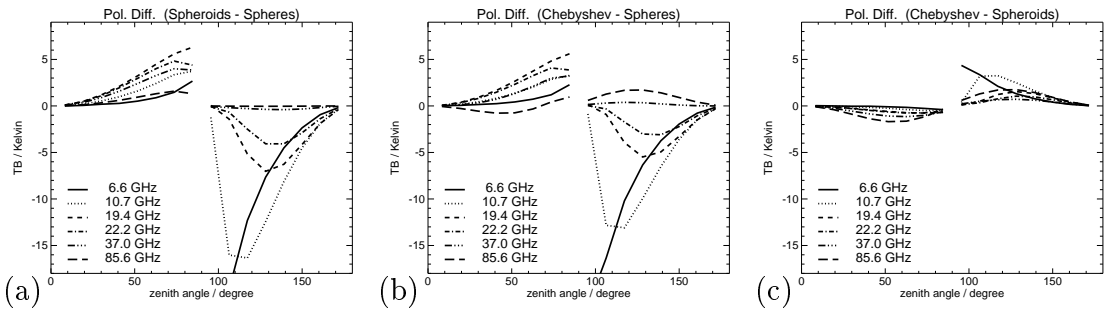


Figure 4.24: *PD differences vs zenith angle (rain only and blackbody emission at the surface): (a) Spheroids minus Spheres, (b) Chebyshev drops minus spheres, (c) Chebyshev drops minus spheroids.*

only those calculations with surface emissivity  $\epsilon = 1.0$ . As for the total intensity, the results for the PD are very similar (Fig. 4.24c) for the two oblate shapes, which both show large differences to the spherical shape. The low frequency range, which produces the largest positive change in PD of up to +5 K when switching to oblate shapes is not sensitive to the small deviation in particle geometry between spheroids and Chebyshev particles. Only the 85 GHz channel, which has a positive (but small) PD for spheroids

changes to small negative values. The PD of downwelling radiation is more sensitive to small changes of the particle shape: Chebyshev drops produce about max. 4 K less negative PD (which gives a positive change) than the spheroid particles. In general, the main findings for PD are similar to the findings for total intensity: The more realistic Chebyshev particles show very similar results to the spheroids on the large scale, but somewhat less changes compared to spheres than the spheroids.

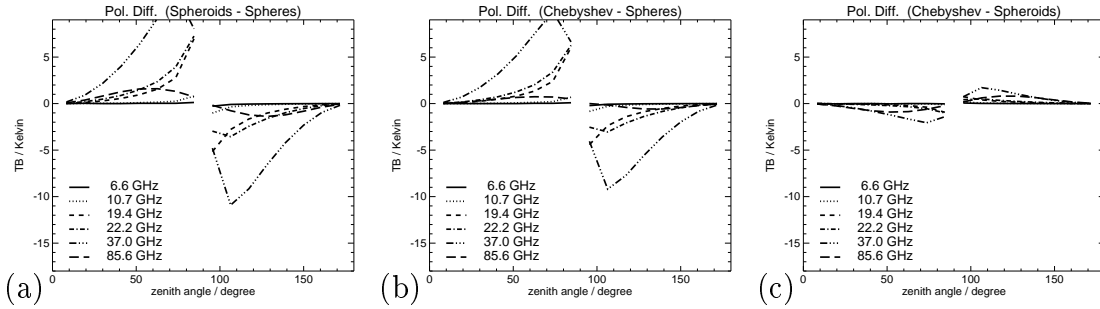


Figure 4.25: All settings as in Fig. 4.24, but with the ice particle layer only (no rain).

When considering ice particle scattering by the single layer with hail, the trend of the calculation with rain only is reproduced. The PD at upward directions is increased (e.g. +10 K for 37 GHz) when either spheroids (Fig. 4.25a) or Chebyshev particles (Fig. 4.25b) are used instead of spheres. At opposite direction of propagation, oblate particles produce a smaller PD. The Chebyshev shapes reduce the changes at 37 GHz originating from the use of spheroids (Fig. 4.25c).

The combination of liquid and frozen precipitation in one calculation leads to a simple addition of the differences at upward directions (not shown here). Since the total PD at upwelling directions is not determined by the intense scattering contribution of ice particles alone, the effect of raindrop shape will be of interest for the remote sensing of precipitation. Polarization difference will be best suited for such applications because it is affected by all hydrometeor layers instead of only the uppermost ice particle layer.

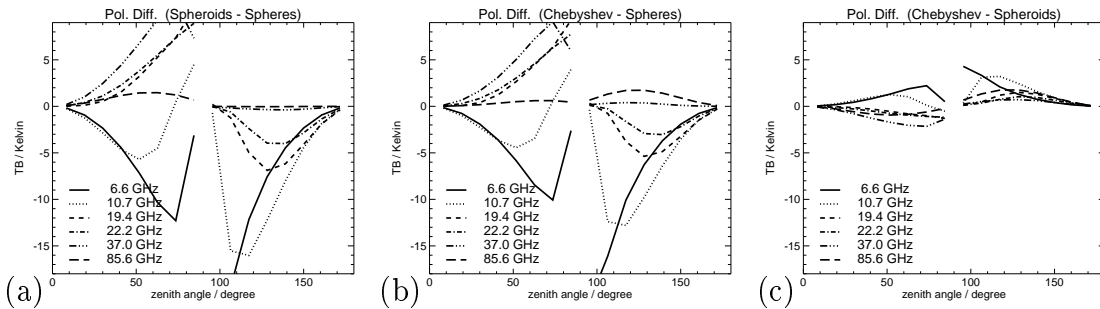


Figure 4.26: All settings as in Fig. 4.20 (both layers, rain and ice), but with sea surface conditions at the lower boundary.

The polarization results still depend on the surface emissivity. For a different distribution of intensity the changes of shape have different effects on the total PD. Figure 4.26 gives the change in PD for the precipitating ice and rain layers over a sea surface (corresponding to Fig. 4.21). It is clear from Fig. 4.26c that the more realistic shapes

described by the Chebyshev shapes add only little to the changes that can be obtained by a spheroid approximation, but the difference (up to an amount of 2 K for 25 mm/h rain rate) is still in the range of detection limits (usually  $\Delta T < 1$  K) and may vary with higher and lower rain rates.





# Chapter 5

## Validation

In order to validate the previous results one needs measurements of microwave radiation in the presence of rain under certain conditions. These conditions have to be chosen in such a manner that a final conclusion can be drawn from the results whether the nonspherical scattering theory is more realistic than Mie-scattering or not.

First of all, the environmental conditions need to be as close as possible to the assumption of a homogeneous plane parallel atmosphere. Otherwise the developed radiative transfer model would not be applicable. Obviously, the observation geometry and frequency are of major importance: A situation is desirable with large and easily observable differences between the model predictions for spherical particles on the one hand and oblate particles on the other hand. These differences have to be measured without ambiguity about their origin. Ice particles, an inhomogeneous field of view and three-dimensional effects can lead to observations that differ from the one-dimensional model predictions, thus making it impossible to focus on effects of particle shape.

With these requirements satellite data cannot be considered for validation purposes: The entire scene within the field of view will not fulfill the one-dimensional assumption in most cases. Furthermore, the differences between both cases for intensity and polarization are not as large in upwelling directions as for the downwelling direction and may as well result from inhomogeneities in the surface properties within the field of view.

Ground-based sensors receive radiation which is mainly influenced by the atmosphere. Downwelling radiation exhibits large differences in the predicted PD for spheres and oblate spheroids especially at elevation angles close to the horizontal. Furthermore, due to the much smaller distance between the radiometer and the targeted measurement volume, the field of view is several orders of magnitude smaller for ground-based radiometers than for satellite observations, resulting in a better concordance with the assumption of a horizontally stratified atmosphere.

### 5.1 Measurements

At the *Institut für Hochfrequenztechnik* of the *Deutsches Zentrum für Luft- und Raumfahrt* (DLR, Oberpfaffenhofen, Germany) a 19 GHz dual polarization radiometer (vertically and horizontally polarized radiation is measured simultaneously with the same antenna) is operated. With a time resolution of  $\Delta t = 10$  s the vertically and horizontally polarized

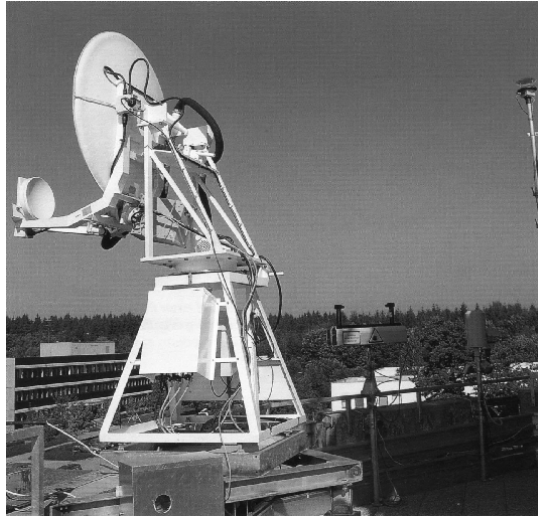


Figure 5.1: *The 19 GHz radiometer on top of the roof: The antenna is aligned to southward direction with an elevation of 30 degree. On the right hand side the meteorological sensors can be seen.*

brightness temperatures  $T_{B,v}$  and  $T_{B,h}$  are recorded. For some intervals in 1996, there exist data recordings (see Tab. 5.1). From autumn 1998 on the recording became operational, leading to continuous time series with only small interruptions due to calibration or maintenance.

Table 5.1: *Temporal coverage of the data available from the 19 GHz radiometer of the DLR Oberpfaffenhofen.*

Year	Observed days per month											
	Jan	Feb	Mar	Apr	May	Jun	Jul	Aug	Sep	Oct	Nov	Dec
1996	–	–	–	10	–	–	31	–	21	31	25	–
1998	–	–	–	–	–	–	–	–	–	–	14	31
1999	27	25	31	28	29	29	29	17	29	n.a.	n.a.	n.a.

Table 5.2 gives an overview of the radiometer specification. The antenna pattern with  $1.2^\circ$  resolution (full width at half maximum, FWHM) gives high spatial resolution measurements. Although the absolute accuracy is only around 2 K, the estimation of polarization differences can be performed better than 0.5 K. This precision is reached because calibrating errors of both channels cancel out: Vertical and horizontal polarization use the same hot load for calibration.

Several meteorological sensors are collocated with the radiometer on top the roof of a DLR building (Fig. 5.1). Temperature, pressure, humidity and rain rate are recorded for the same time as the radiometric observations. However, the temporal resolution of the environment recording is limited to intervals of 60 s. Observation of wind speed and wind direction started November 1998 and is not available for the 1996 data. The

Table 5.2: Radiometer description.

(transl. from <http://www.op.dlr.de/~igex98op/monitor/radiometerdaten.html>)

Parameter	Value	Parameter	Value
Frequency	19 GHz	Bandwidth	100 MHz
Integration time	1 s	Resolution	< 0.5 K
Accuracy	1–2 K	Beamwidth (FWHM)	1.2°
Side lobes	< –32 dB	Cross polarization	< –32 dB
Azimuth angle	180°	Elevation	30°
Polarization	horizontal/vertical		

Table 5.3: Description of sensors.

(translated from <http://www.op.dlr.de/~igex98op/monitor/sensordaten.html>)

Sensor	Vendor	Bezeichnung	Accuracy	Range
Temperature	Rotronic	RTD Pt 100 ohm	0.5 K	[–40°C, +60°C]
Humidity	Rotronic	Hygromer-C94	2.0 %	[0, 100] %
Pressure	Sensortechnics	D/C 414	1.0 hPa	[800, 1100] hPa
Rain gauge	Thies Clima	Ombrometer HP	0.3 mm/h	[0, 120] mm/h
Ultrasonic anemometer	MESA Systemtechnik	WNT	2 %	[0, 360]°

different sensors are listed in Tab. 5.3 together with the manufacturer, sensor resolution and sensor accuracy.

Data recording is done automatically with direct transfer to the University Bonn. In case of ambient temperatures below zero degree a heating mechanism clears the antenna from snow or ice particles (e.g., hoarfrost). Major problems that may arise during the measurements with this setup originate from the viewing geometry and the finite rain detection limit: Rain rates cannot be quantified to better than 0.3 mm/h. In case of slight rainfall the onset will be recorded too late or even completely missed although the radiometer receives radiation affected by precipitation due to its oblique line of sight.

## 5.2 Data processing

Before relating the measured TB and PD to the observed surface rain rate (RR) the data are subject to a calibration procedure. From sequences which are classified as rain free by looking at the observed RR and TB, the PD signal is adjusted to zero. This procedure is justified by the fact that under clear sky conditions no source for polarized radiation exists. Observations with a zero RR from the meteorological sensors may also be contaminated by rain due to the viewing geometry: The radiometer is oriented to the south with an elevation angle of 30 degrees above the horizontal. With such a low viewing direction the radiometer may observe distant clouds and rain events that move beside the

rain gauge due to wind directions which are not parallel to the south-looking azimuthal orientation of the instrument. Even if the observed RR corresponds to observed cloud and precipitation features there will be a time lag between the ground observation of precipitation and the radiation signal. Unless the atmosphere is strictly homogeneous (perfectly one-dimensional), this time lag depends on wind speed, wind direction and the average height from which the radiation originates. The time lag reaches from zero (homogeneous atmosphere) up to 3 to 5 minutes and may even be infinitely large when the wind direction is perpendicular to the viewing direction, and the atmosphere is highly inhomogeneous. In addition, a beginning rain event will not be recorded immediately but with a time lag that depends on rain intensity and the fabrication of the precipitation sensor. This instrumental delay adds to the geometric delay and needs to be corrected as well.

For some data periods the wind direction and speed were not available, but even for situations with known wind conditions it was nearly impossible to calculate the time lag from auxiliary data. Instead, a statistical method was applied for the determination of the time lag. Sections of two hour length of the time series (Fig. 5.2) of RR were shifted along the time axis and correlated with the TB time series. The correlation curve along the time shift was searched for a peak of maximum correlation: If a clear maximum correlation above a certain threshold could be found (Fig. 5.3a), then the width of this peak was determined at 70 percent of peak height. The center of the peak width was then taken as the position of maximum correlation and used to calculate the time lag between both observations. This method avoids the selection of misleading peaks at the maximum of the correlation function, especially if the top of the peak is rather flat (Fig. 5.3b).

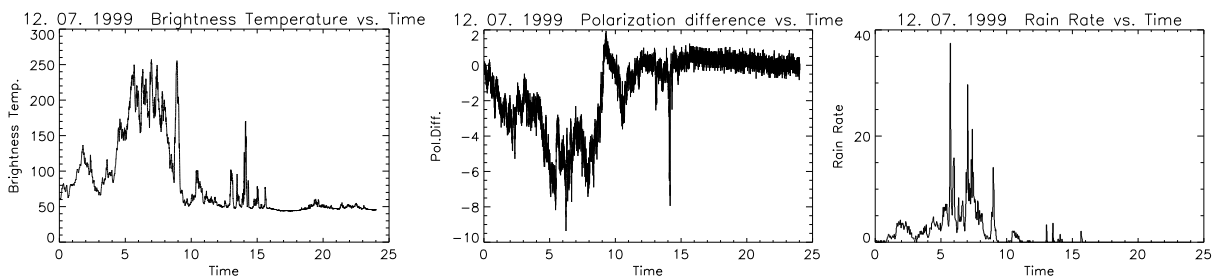


Figure 5.2: *Time series of TB, PD and RR at July 12, 1999.*

If the threshold value was not reached or the time lag exceeded a maximum value of 5 minutes, the data set was excluded from the analysis. Otherwise the RR measurements were shifted in time and matched with the TB and PD data. Such triples (RR,TB,PD) of all two hour sections of the 60 days which were selected as homogeneous rain events were classified by rain rate and averaged for each specific rain rate. The result is shown in Figs. 5.4 to 5.6. The selection of the 60 days was based on the minimum duration of the rain event: at least 30 minutes continuous rainfall had to be present in order to assure a quite homogeneous atmosphere.

The averaged TB and PD results as a function of rain rate show a clear dependence on the rain rate (Fig. 5.4 and Fig. 5.5). However, the surface RR is not the variable of choice when examining the radiation of a rainy atmosphere if the height of the rain layer is unknown. Radiation effects in both signals, that is TB and PD, respectively,

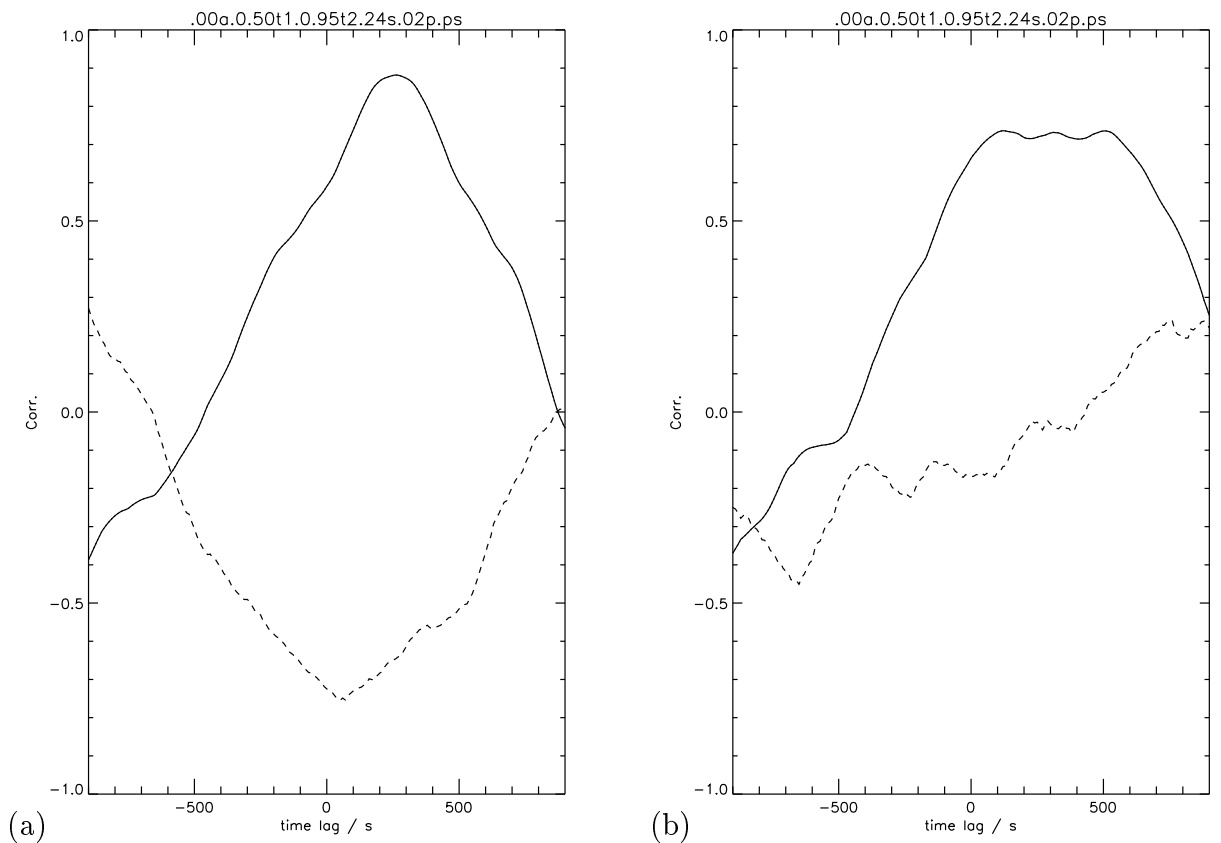


Figure 5.3: *Two examples correlation between TB and RR as a function of time shift (solid line). Example (a) gives a clear maximum with an symmetric shape of the peak correlation. The absolute maximum of example (b) may be misleading, so the center of the peak width at a certain threshold value is used for the determination of the time lag.*

will be linked more closely to the total liquid water content of the lower atmosphere and therefore be sensitive to the rain layer extension: The total LWP may be the same for two different rain rates, while a constant rain rate may correspond to a doubled LWP if the rain layer thickness is doubled. This effect of water amount is (partially) cancelled out by representing the polarization signal as a function of TB (Fig. 5.6). Since both signals are proportional to LWP, the functional dependence on the unknown LWP is effectively suppressed.

### 5.3 Comparison with the model

Model calculations show the influence of rain layer thickness even clearer. Figure 5.8 gives the resulting TB for different rain rates in an idealized atmosphere. A water cloud with  $0.5 \text{ g/m}^3$  liquid water content between 1 and 3 km height attenuates the polarization originating from the rain layer. The rain rate is assumed to be constant with height for 9 different rain layer top heights from 1 to 3 km. The variation of the rain layer height results in a large variation of the polarization signal at the bottom of the atmosphere. The reason for this variability is the strong impact of rain columns height on the total

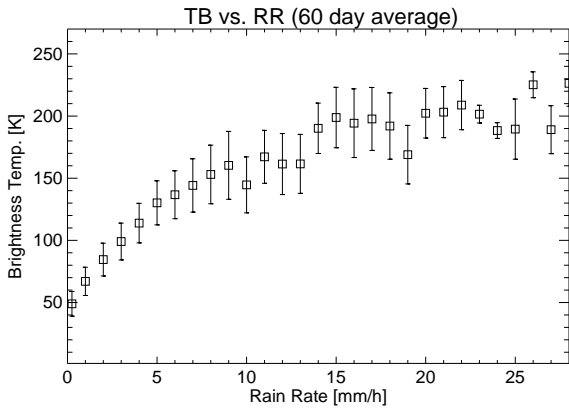


Figure 5.4: Measured brightness temperature as function of surface rain rate for 60 selected days. Observations were made at 30 degrees elevation and 19 GHz frequency. The standard deviation of the averaged value is indicated with error bars.

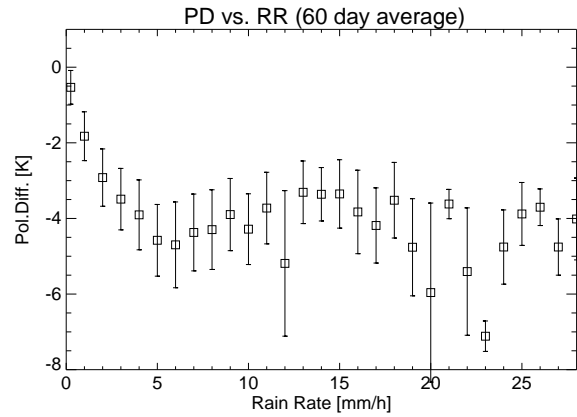


Figure 5.5: Measured polarization difference as function of surface rain rate (same observations as in Fig. 5.4).

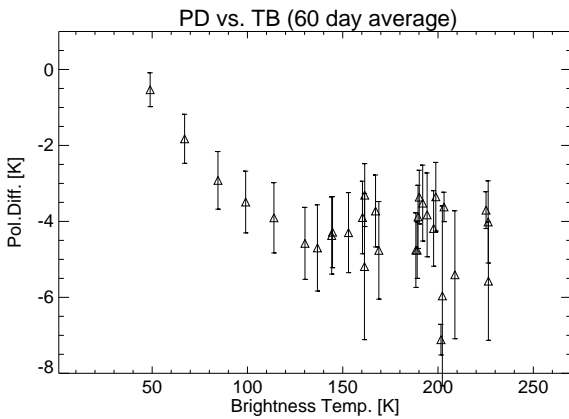


Figure 5.6: Measured polarization difference as function of brightness temperature (same observations as in Fig. 5.4).

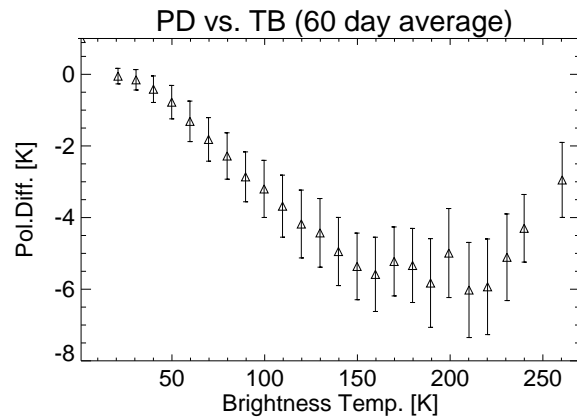


Figure 5.7: Measured polarization difference as function of brightness temperature (same observations as in Fig. 5.6, but with histogram function with respect to TB instead of RR).

optical thickness. Only rain layers with non-isotropic radiation produce the polarization while all rain layers attenuate the polarization signal. With high rain columns only the topmost layers will have a non-isotropic distribution of radiation at high rain rates, while the lowest layers receive the same amount of radiation from all directions.

The cloud drop size distribution (DSD) is a modified gamma distribution with a modal radius of 5.5 micron. For the rain layer the Marshall-Palmer DSD is selected. Surface emission is set to 0.9 while the atmospheric temperature profile is adjusted to 6 different temperatures in the lowest layer, ranging between 273.15 and 298.15 K. The profile is calculated with a constant tropospheric lapse rate and a constant profile of

relative humidity. Increasing the atmospheric temperature leads to an increasing amount of water vapour in the troposphere and thus to an increased optical thickness at higher temperatures. All situations were calculated with either spherical or oblate raindrops.

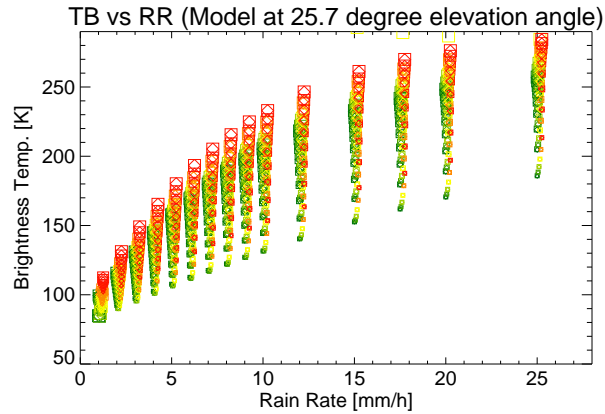


Figure 5.8: Modeled TB versus rain rate. The size of the plot symbols indicates the rain layer height (from 1 to 3 km). The colour gives the atmospheric temperature at lowest level from 0 (dark green) to 25 degree centigrade (red).

The influence of atmospheric temperature (indicated by the colour of the plotsymbols in Fig. 5.8) is much smaller than the change in TB caused by different rain layer heights (indicated by the size of the plot symbols). Both effects are almost identical for spheres (square symbols) and oblate spheroids (diamond symbols).

The PD results (Fig. 5.9) reveal large differences between spherical and nonspherical particles. While spheres produce small positive PD under all circumstances, the nonspherical drops produce large negative results which reach a maximum value at high rain rates and saturate with increasing optical thickness. This saturation process is mostly determined by rain rate and rain layer thickness.

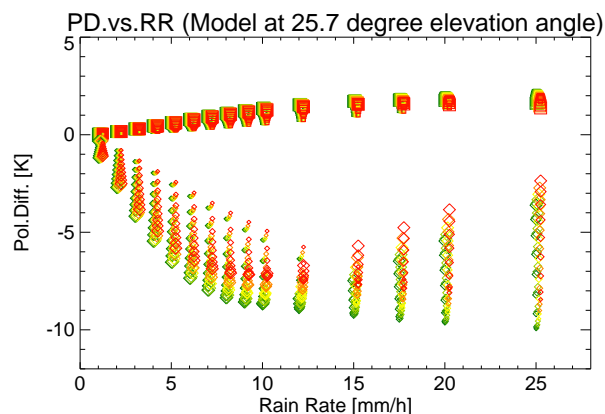


Figure 5.9: Modeled PD versus rain rate. Squares (upper branch) indicate spherical particles, diamonds (lower branches) indicate oblate raindrops.

The modeled PD is also given as a function of TB (Fig. 5.10). Comparing Fig. 5.10 with Fig. 5.6 clearly shows that the radiative transfer model and the selected drop shapes explain the measured data very well. However, TB and PD do not only depend on rain column height and rain rate but also on the drop size distribution, which can significantly differ from the Marshall-Palmer distribution for rain rates above 10 mm/h. In particular, the influence of DSD on PD is not cancelled out if PD is plotted versus TB as it is the case in Fig. 5.10 for a fixed Marshall-Palmer distribution. In *Hornbostel and Schroth* (1995) and *Hornbostel et al.* (1995) it was shown that it is possible to derive an path averaged DSD from PD and TB if a fixed rain layer height is assumed.

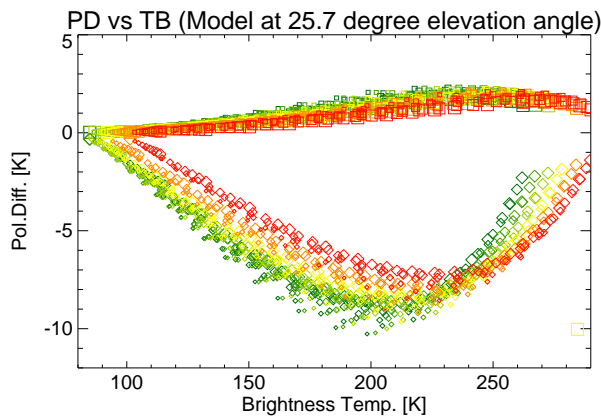


Figure 5.10: *Modeled PD versus TB. The variation in PD for nonspherical particles due to rain layer height is cancelled out, the remaining difference is simply the variability in atmospheric temperature and a more pronounced saturation due to increased optical thickness with warmer atmospheres.*

## 5.4 Conclusions

The remaining differences between the modeled and measured data can be attributed to the uncertainties in the state of the atmosphere: The exact vertical profiles of temperature, humidity, liquid water content and drop size spectra are unknown. Water drops may tumble around their preferred vertical orientation and undergo oscillations around their equilibrium shapes (*Beard, 1984; Beard and Tokay, 1991*). Finally, the melting layer at the 273 K temperature level is not taken into account.

This imperfect knowledge forces simplifications and assumptions for the radiative transfer modeling. Keeping in mind that the observed data shown here are an average over 60 days with different weather situations, the result is an encouraging confirmation of the radiative transfer model.



## Chapter 6

# Implications for Remote Sensing of Precipitation

Within the previous chapters the impact of raindrop shape on forward model calculations was quantified. An important question is the relevance of these findings for current and future remote sensing applications. Since the consequences of particle shape are very different for different observation platforms, the following discussion is divided into ground-based measurements and observations from either airborne or spaceborne sensors.

### 6.1 Ground-based observations

Passive microwave radiometry is a method well suited and often used for the retrieval of cloud liquid water path (LWP) (e.g., *Westwater, 1978*). Ground based radiometers measure the radiation emitted by the atmospheric constituents, which are gases, liquid water and ice. The equivalent brightness temperature obtained at one or more frequencies can be related to the LWP by either statistically derived algorithms (based on training data with observed brightness temperatures and the measured LWP) or by physically based algorithms. The latter are based on accurate modeling of the atmospheric radiative transfer.

Both types of algorithms perform well as long as the LWP is produced only by small cloud droplets. In the presence of rain the situation is worse: Rain and cloud drops both emit microwave radiation and therefore increase the observed TB. Unfortunately, the sensitivity of TB to rain and cloud particles shows significant differences due to their particle sizes: The absorption coefficient of rain droplets increases much stronger than proportionally to the drop volume, which is the case for small cloud droplets and the basis of most algorithms. In addition, the larger raindrops tend to have a much higher single scattering albedo than the smaller cloud particles. However, the TB signal is the sum of both and decomposition of the signal contributions from rain and cloud fractions is not possible without an additional source of information which will allow for an estimation of the rain water fraction.

### 6.1.1 Sensitivity to cloud and rain particles

In order to investigate the use of polarized microwave measurements for the remote sensing of LWP and the discrimination of cloud and rain water in the received signal, a sensitivity study was carried out. The frequency of 22.235 GHz was selected in this example because it is the lowest (and therefore best-suited) dual-polarized frequency of the MICCY radiometer (*Crewell et al., 1999b*). All calculations were performed for nonspherical raindrops and spherical cloud droplets of a cloud between 1 and 2 km height and a ground-based radiometer with a 36 degree elevation angle. The cloud LWP was modeled with a DSD given by a modified gamma distribution with a modal radius of 5.5 micron. The rain LWP was produced by a Marshall-Palmer distribution. The LWP due to cloud water is varied between 0.0 and 1.3 kg/m<sup>2</sup> while the LWP due to rain is varied between 0.0 and 1.6 kg/m<sup>2</sup>. All possible combinations of both kinds of LWP were calculated, resulting in total LWP values between 0.0 and 2.9 kg/m<sup>2</sup>.

Figure 6.1 shows the resulting brightness temperatures as a function of total LWP. The symbol size indicates the amount of LWP caused by to the rain water fraction. The increase in TB is strongest for pure rain LWP (uppermost symbols in each column) and smallest for the pure cloud LWP (lowest symbols). As a consequence, mixtures of cloud and rain water cannot be identified unambiguously by monospectral TB measurements.

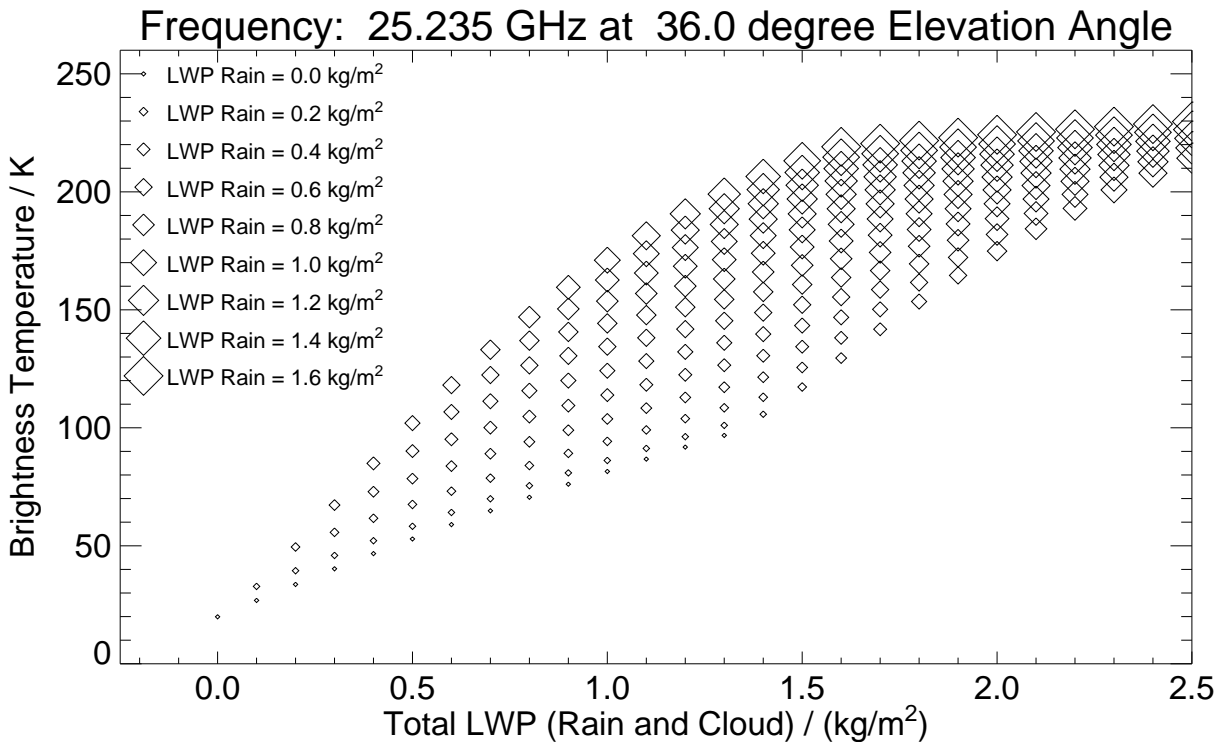


Figure 6.1: *Brightness temperature versus total LWP of cloud and rain mixtures. The symbol size indicates the rain LWP fraction of the total LWP.*

Assuming a fixed cloud LWP for the retrieval of total LWP may be justified at very high amounts of rain LWP where the sensitivity to cloud LWP is small (Fig. 6.2). This is not the case for small rain LWP, say less than 0.5 kg/m<sup>2</sup>. Especially when cloud and rain LWP are similar the variation of the mixture leads to large changes in the TB signal.

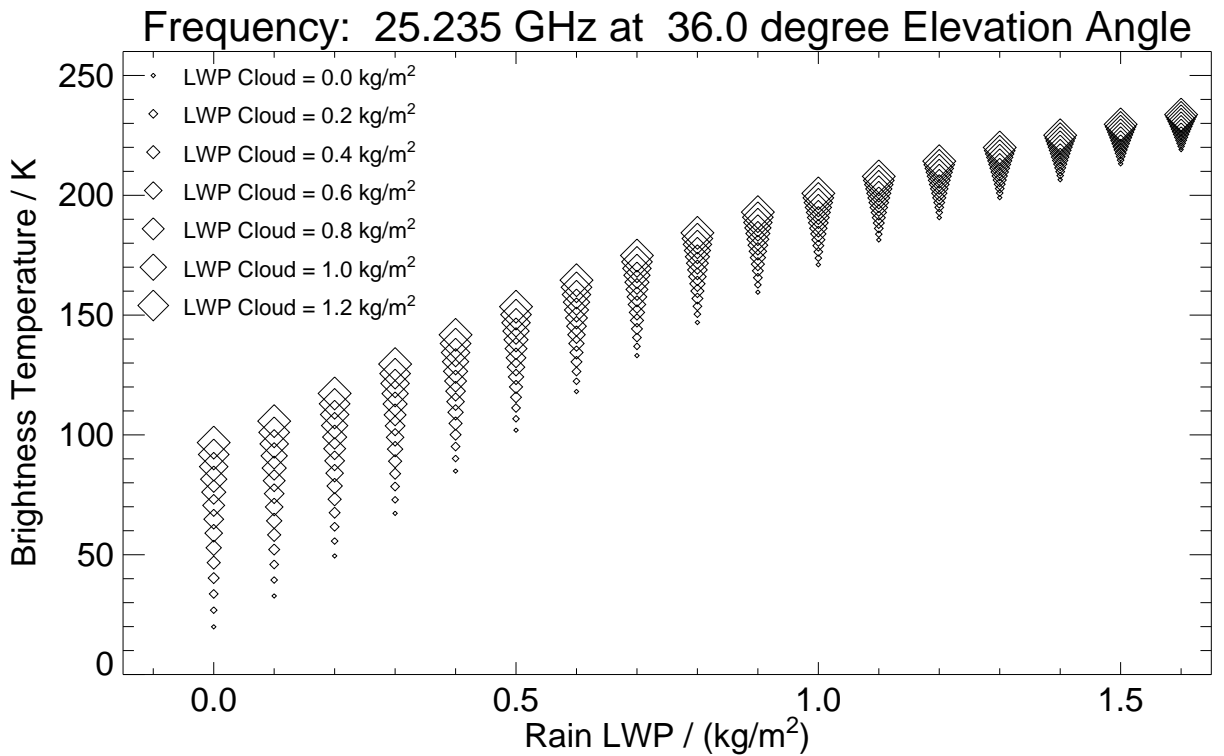


Figure 6.2: *Brightness temperature versus LWP caused by rain water. At high rain rates the sensitivity to cloud LWP is decreased.*

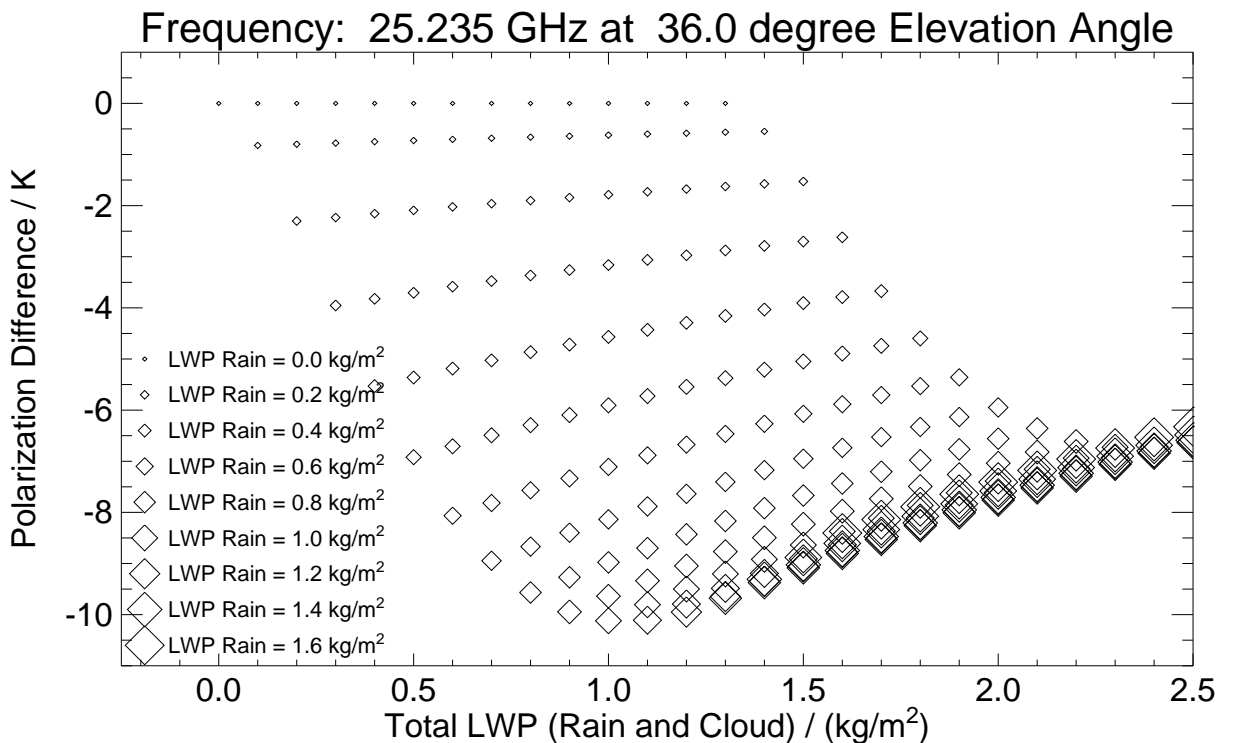


Figure 6.3: *PD versus total LWP for different fractions of rain LWP: With increasing rain water fractions the PD signal is increased.*

The corresponding PD results of Fig. 6.1 and Fig. 6.2 are shown in Fig. 6.3 and Fig. 6.4, respectively. Increasing rain water amounts cause the negative PD values with a nearly linear slope for small amounts of rain. At higher rain LWP, the PD signal saturates and diminishes again. The overall sensitivity of PD to rain LWP is reduced with increasing cloud LWP.

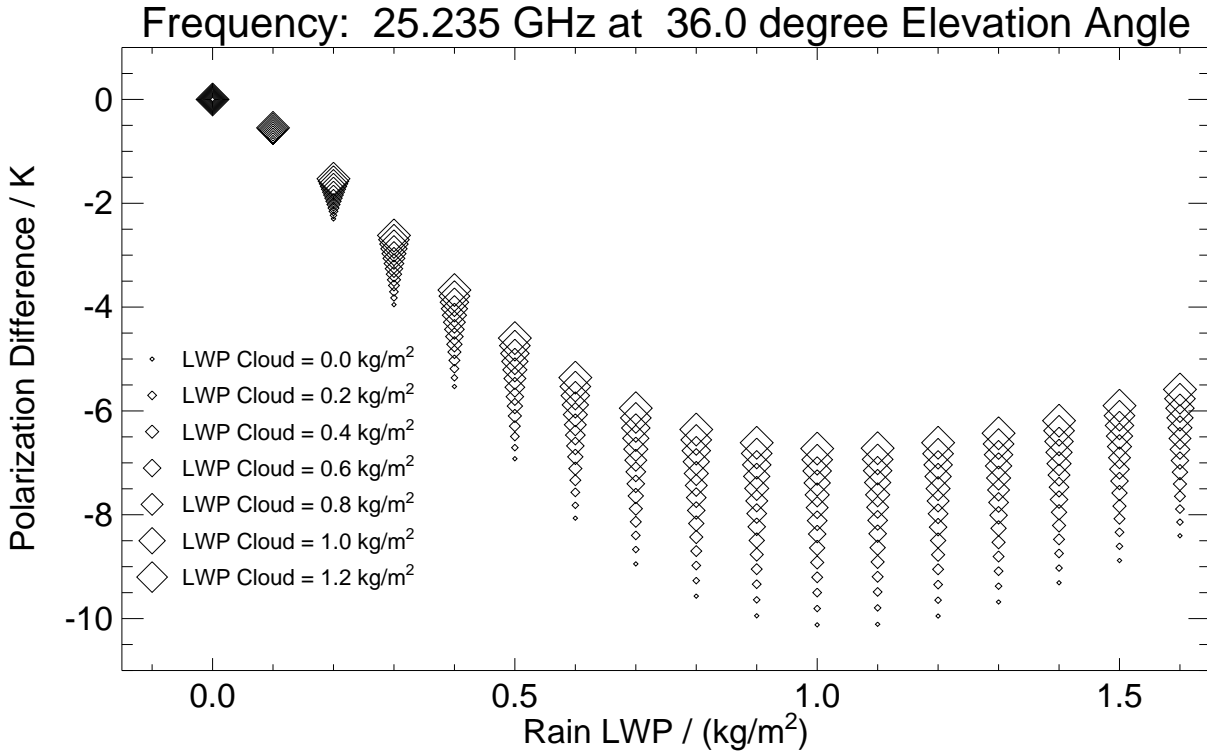


Figure 6.4: *PD versus rain LWP: At low rain amounts the PD is determined by the rain LWP with no impact from the cloud LWP. At higher rain fractions the saturation caused by the rain liquid water is dominant and the additional saturation by cloud liquid water leads to a variation of PD with cloud LWP.*

The variation of the radiometric signal with cloud LWP shows a contrary behaviour for TB and PD signal: While the TB variation due to cloud water is strongest at low rain water amounts, the variation of PD with cloud water is strongest at large rain water amounts.

### 6.1.2 Proposed method

Figure 6.5 illustrates the information content of polarized measurements concerning the LWP of cloud and rain. The different combinations of cloud and rain LWP are positioned by their response in TB and PD in this diagram. Cloud water variations result in a horizontal displacement with no PD signal. Rain water variations result in a stronger horizontal displacement and an additional vertical displacement to negative PD. Mathematically speaking, these vectors of sensitivity are a linear independent combination and allow the retrieval of two degrees of freedom by the measurement.

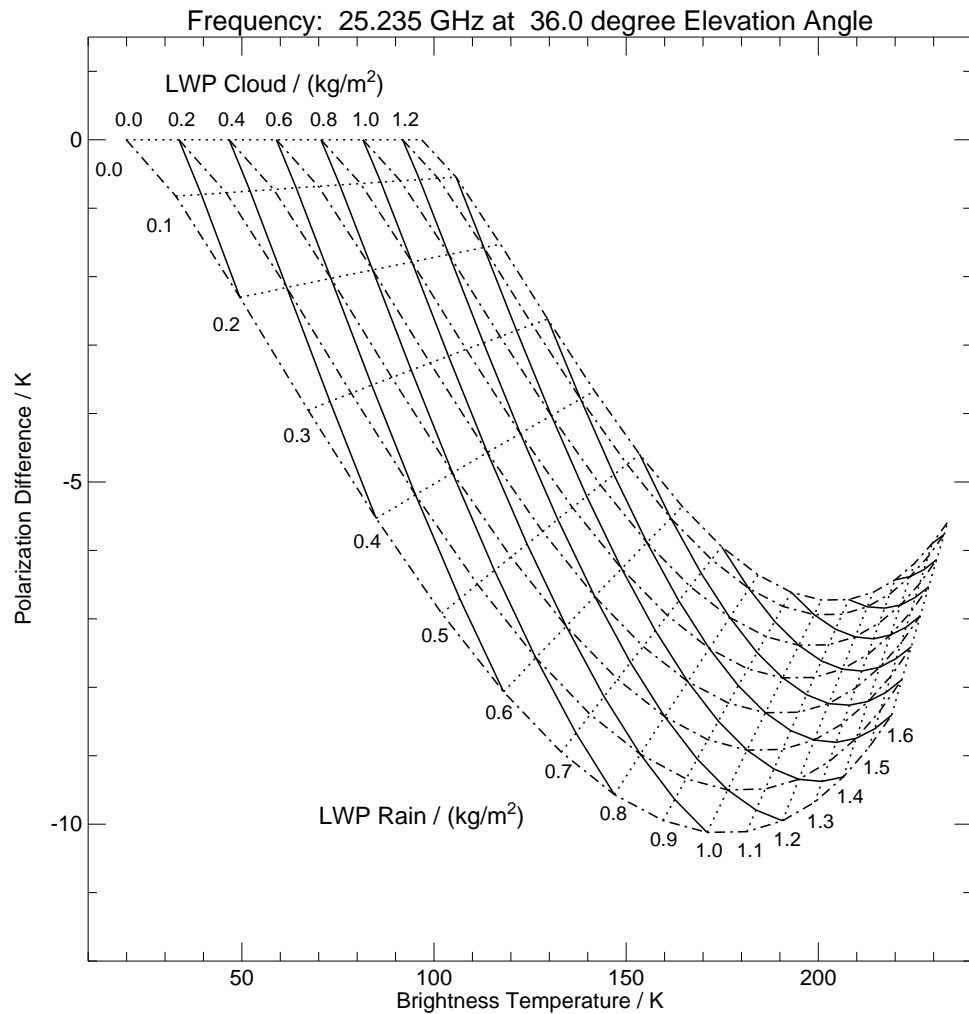


Figure 6.5: Sensitivity of PD and TB to rain LWP, cloud LWP and total LWP. Along solid lines the total LWP is constant, dashed lines indicate constant rain LWP and dash-dotted lines indicate constant cloud LWP.

By giving a measured pair of TB and PD and by assuming a fixed rain layer height and DSD, it should be possible to retrieve the rain LWP and cloud LWP separately. The accuracy of such an algorithm will depend on the representativeness of the modeled atmospheric conditions and the calibration of the radiometer. Recently build radiometers have an accuracy of 1 K or better. With such instruments, the retrieval of small rain water amounts within a cloud will be possible. Small rain rates may occur in and below clouds without being associated with a surface rain rate. If the LWP due to rain exceeds  $0.1 \text{ kg/m}^2$ , the PD will reach a value below  $-1 \text{ K}$  and, therefore, allow the detection and discrimination of rain in the presence of cloud water.

Further information will be gathered by additional frequencies (most radiometers for LWP retrieval are multi-channel radiometers) and observations at several elevation angles. The sensitivity of PD to raindrop shape which is used in this study varies with frequency and viewing angle since both parameters affect the optical thickness. Figure 6.6 gives the PD signal as a function of rain LWP for a fixed total LWP. Six different elevation angles are shown.

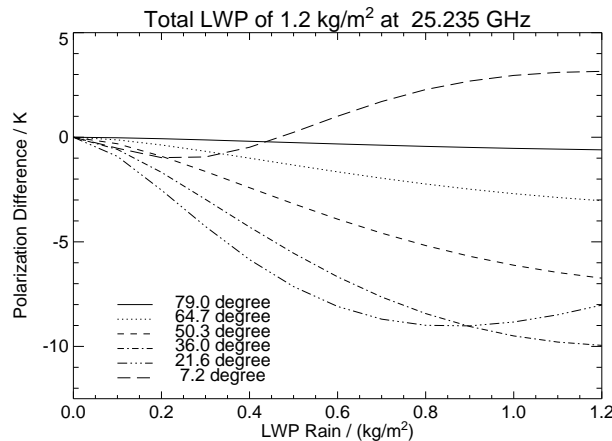


Figure 6.6: *PD* as a function of rain LWP at a fixed total LWP of  $1.2 \text{ kg/m}^2$  for six different elevation angles.

Without rain (left side of the graph) the PD is zero at all observation angles. At directions closer to nadir the polarization signal is very small. Lowering the radiometer viewing angle to the horizontal increases the sensitivity and the total optical thickness until a saturation is reached for large rain amounts. Such a saturation is more pronounced at higher frequencies because of the increased absorption of liquid water. Using non-saturating and saturating combinations of viewing angle and radiometer frequency will add information to the retrieval process.

However, this is only a sensitivity study. A possible retrieval algorithm may be derived from radiative transfer calculations which have to be based on realistic atmospheric profiles. The consistent set of microphysical cloud properties could be obtained from a detailed cloud model. Even then the applicability of such an algorithm nevertheless will depend on the question of how good the one-dimensional assumption is fulfilled in the observed rain event. The impact of three-dimensional effects on the downwelling radiation and especially the polarization signal is not yet determined.

## 6.2 Observation of upwelling radiation

The consequences of nonspherical particle shape for algorithms that evaluate upwelling brightness temperature are less clear than for ground-based observations. The main reason for this is the origin of the radiation: Downwelling radiation either originates directly from the atmosphere or has undergone at least one scattering process within the atmosphere on cloud or precipitation particles. Surface emission may affect the polarization measurements for ground-based sensors by changing the degree of isotropy in the atmosphere, but even then the information content of the observed signals is still connected to the hydrometeors present.

In case of measurements from above with airborne or spaceborne radiometers the total signal often contains a part which is mainly unaffected by hydrometeors. Especially at frequencies below 50 GHz the total atmospheric optical thickness is low enough for observations of surface effects from space. Under such circumstances the observed brightness temperatures include contributions from both, surface and atmosphere. If the

contribution from the atmosphere cannot be identified unambiguously within the mixed signal, the retrieval of atmospheric parameters such as liquid water path and rain rate is subject to large errors.

### 6.2.1 Current methods

A separation of atmosphere and surface effects is often difficult. Only if the contribution from precipitation differs significantly from the microwave signature of the surface the distinction is possible and the retrieval of precipitation can be performed. When looking at the first order effects of precipitation over water surfaces such a situation is given:

- In terms of TB the sea surface is a cold and rather homogeneous background signal
- In the low frequency regime (37 GHz and below), the atmospheric water content produces an increasing warm signal with increasing water amount
- Sea surfaces emit a large positive PD
- Polarized surface emission is depolarized by scattering and absorption at cloud and precipitation (more effectively at higher frequencies)
- At 85 GHz (and higher frequencies) the optical thickness for saturation of the rain emission signal is reached at low rain rates: The emission signal at 85 GHz originates mainly from the uppermost rain layer
- Scattering on ice particles at 85 GHz effectively decreases brightness temperatures above the rain layers

Based on these effects, most algorithms can be grouped into emission based methods (looking at the warm emission by rain water on the low frequency range) and scattering based methods (looking at the brightness temperature depression caused by ice particle scattering in the higher frequency range). Some algorithms use the full information of the seven SSM/I channels or even data from additional sensors (AVHRR). A common feature of the rain retrieval algorithms is that the observed PD is assigned to the ocean surface. Thus, the screening of this PD by precipitation is an indirect estimation of the rain rate.

Rain retrieval over land is much more difficult due to the high emissivity, its larger spatial variability, and the low polarization signal of land surfaces. The warm emission from liquid water cannot be distinguished from the warm background emission from the lower boundary. Polarization signatures of vegetation, soil and soil moisture are small (compared to water surfaces) and not very well known, so an obvious signal of polarization depression that may be used for the retrieval of precipitation does not exist. Only the indirect method of TB depressions observed in the high frequency channels may serve for rain retrieval techniques over land. Rain which is not associated with large amounts of ice particles of a certain size above the rain layer (warm rain events) will go undetected.

### 6.2.2 Polarization as an additional atmospheric signal

The effects of scattering particles in radiative transfer can neither be described as "polarizing" nor as "depolarizing", they are evident both at the same time. Completely polarized radiation will be depolarized by scattering effects on hydrometeors, but scattering will also polarize a beam of completely unpolarized light under most circumstances. Natural radiation can always be split up into two parts, polarized and unpolarized radiation.

The largest source of polarization is the emission of water surfaces. This polarization signal is attenuated by absorption and scattering, but a significant amount of polarization is added by the scattering process. Neglecting this effect may lead to errors in the retrieval of rain rates.

In the following section the possible retrieval error induced by false assumptions of model calculated brightness temperatures will be estimated. For that purpose the effects on six widely used rain retrieval algorithms will be studied:

- Bauer and Schlüssel  
(*Bauer and Schlüssel*, 1993),
- NOAA/SRL  
(as described in *Conner and Petty* (1998), based on *Grody* (1991); *Ferraro et al.* (1994); *Ferraro and Marks* (1995)),
- NASA/GSCAT  
(as described in *Conner and Petty* (1998), based on *Adler et al.* (1994)),
- Ferraro  
(*Ferraro et al.*, 1996),
- Adler  
(*Adler et al.*, 1993),
- Ferriday  
(*Ferriday and Avery*, 1994).

A model atmosphere with the following properties is considered: The sea surface temperature is 293 K, the melting layer with 273 K is located at 3 km height. Below 3 km a vertically constant rain rate is assumed. Above 3 km height up to 4 km height the precipitation is split up into a mixture of liquid and frozen precipitation. Above 4 km up to a height of 6 km only frozen precipitation particles are used. A calm water surface (Fresnel reflection) is used as the the lower boundary condition. The size distribution for all types of precipitation is set to the Marshall-Palmer distribution. Rain is modeled by oblate spheroids with size-dependent aspect ratio. The ice particles are switched to 3 different geometries: A fixed aspect ratio of 1.7 (which means oblate particles) for all sizes of hydrometeors ("Type-I"), the same size-dependent aspect ratio as used for rain ("Type-II"), and a fixed aspect ratio of 3.0 regardless of particle size ("Type-III"). These choices are not meant to be valid descriptions of the hydrometeor type that can be found in hail, graupel, or snow, but they bear some relation to the parameters of natural ice particles in clouds and allow for a rough estimation of the extremes that may affect the



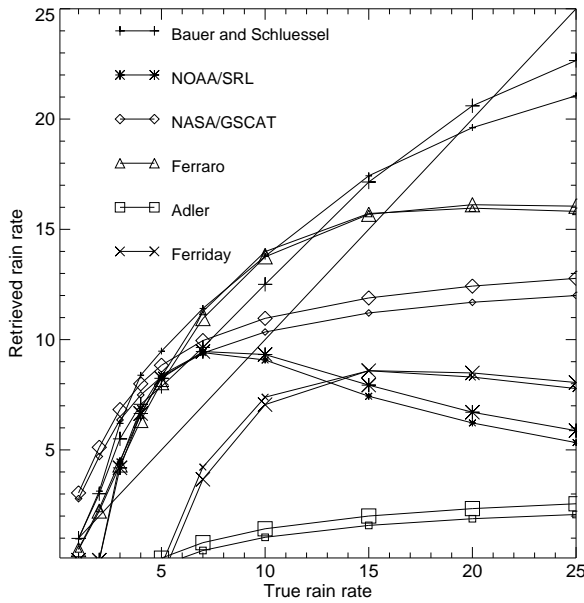


Figure 6.7: Rain rate retrieval with six different algorithms (see text for details) for a simulated rain layer (without ice): Results obtained by using spherical raindrops are indicated by small plot symbols, oblate raindrops by large plot symbols.

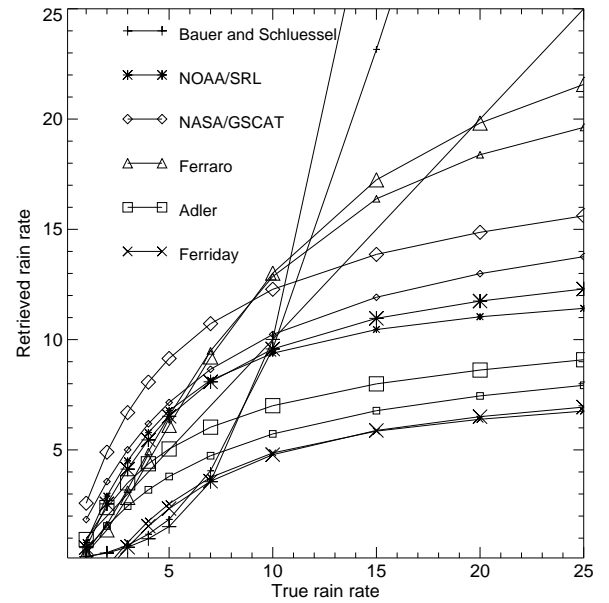


Figure 6.8: Rain rate retrieval in the presence of rain and ice particles. Large symbols indicate nonspherical particles (Type-I), small symbols indicate spherical shape.

rain retrieval: In the presence of large snowflakes the scattering effect at 85 GHz certainly will be very different from the scattering on hail or graupel particles.

For a more realistic treatment of ice particle scattering the effect of the melting layer should be as well included as the density effects for mixtures of ice and air: Snowflakes have a large dimension and also a large aspect ratio, but contain only a small amount of frozen water. Furthermore, the terminal velocities of snowflakes will be smaller than those of raindrops. If the liquid precipitation below the melting layer originates from ice particles, then the absolute number of ice particles per volume and the size of the ice particles will be increases (compared with the DSD of raindrops) to compensate for the effects mentioned above.

Figure 6.7 gives the retrieval results for the atmosphere with the rain layer only (without any ice particles). Large plot symbols give the result obtained with oblate particles, small symbols indicate the spherical result. Although the rain layer reaches up to 3 km, all algorithms underestimate the rain rate. This result cannot be used to assess the quality of the algorithms since the model calculations are very simplified and do not take into account the field of view averaging and the effect of inhomogeneous beam-filling. However, there is a large deviation between the different algorithms. The effect of raindrop shape on the retrieval is small compared to the algorithm uncertainty. This result could be expected due to the nature of the algorithms: Most of them use the scattering information from the 85 GHz channel which is not affected very much by scattering at liquid water.

The results for rain and hail combined (Fig. 6.8, nonspherical particles shown again

with large symbols) reveal larger differences between spherical and nonspherical shape. The deviation between the algorithms is less pronounced than for the rain layer only. The effect of particle shape reaches up to 1 to 2 mm/h, depending on algorithms and rain rate.

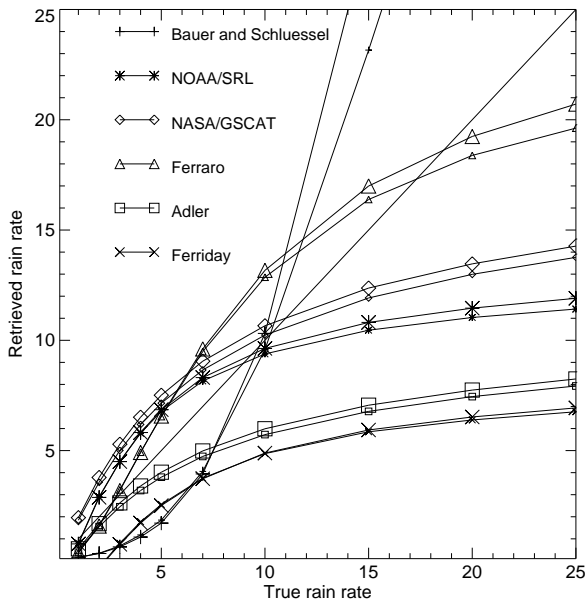


Figure 6.9: *Rain rate retrieval in the presence of rain and ice particles. Large symbols indicate nonspherical particles (Type-II), small symbols indicate spherical shape.*

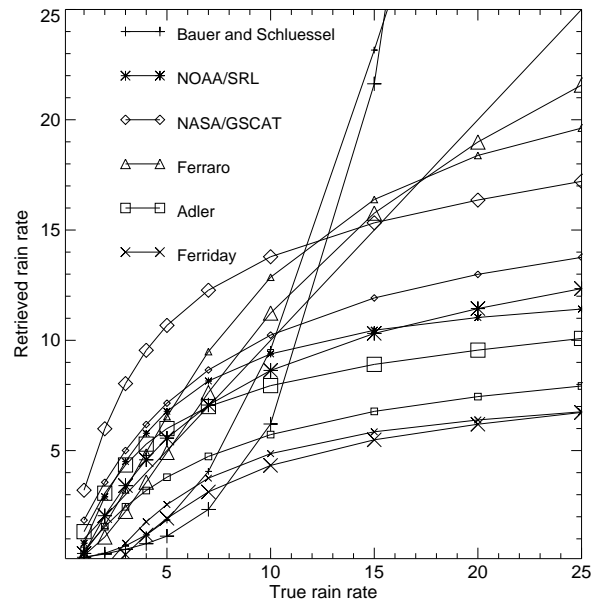


Figure 6.10: *Rain rate retrieval in the presence of rain and ice particles. Large symbols indicate nonspherical particles (Type-III), small symbols indicate spherical shape.*

All the algorithms have a high sensitivity to ice particle scattering. Thus the shape of the ice particles is of major importance for the rain retrieval. Figures 6.9 and 6.10 show the results for the Type-II and Type-III ice particles above a nonspherical rain layer. In both figures the results are compared to the calculation with spherical shapes for rain and ice. While the Type-II ice particle shape (aspect ratio depending on size) gives results closer to the spherical assumption, the Type-III shape with a much higher aspect ratio leads to significant changes in the retrieved rain rate. This may be of major importance in the presence of a melting layer where large snowflakes melt down to liquid raindrops. During this process particles are produced that on one hand show the nonspherical shape of large ice particles and on the other hand have a complex refractive index that is much larger than for pure ice. The latter effect is caused by the mixing of air, water, and ice in the melting particles and thin water coatings around frozen cores.

Such particles will have a strong impact on the observed brightness temperatures. However, the size and shape of ice particles are directly linked with the rain intensity, but with the synoptic situation and the cloud microphysical processes that took place in the generation of the raining cloud.

The highest sensitivity of the 85 and 37 GHz channels to the specific ice particle shape is demonstrated with Figs. 6.11 to 6.14. From the calculations that are used in Figs. 6.7 to 6.10 the resulting PD is given as a function of rain rate. Figure 6.11 gives the decrease

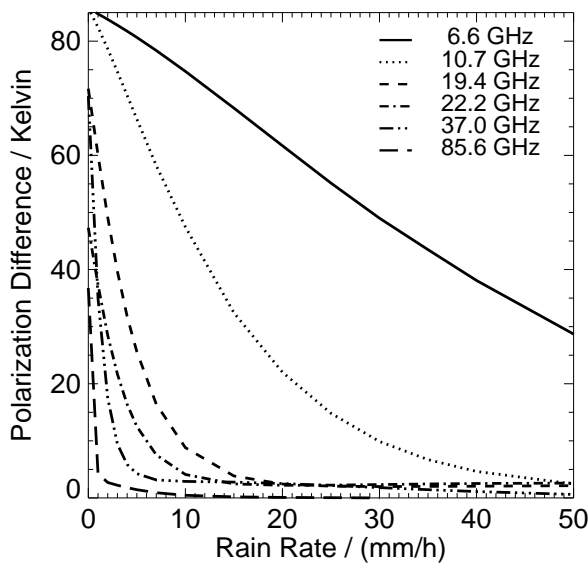


Figure 6.11: *Polarization difference versus rain rate over a calm water surface for the rain layer without ice (corresponding to the results of Fig. 6.7).*

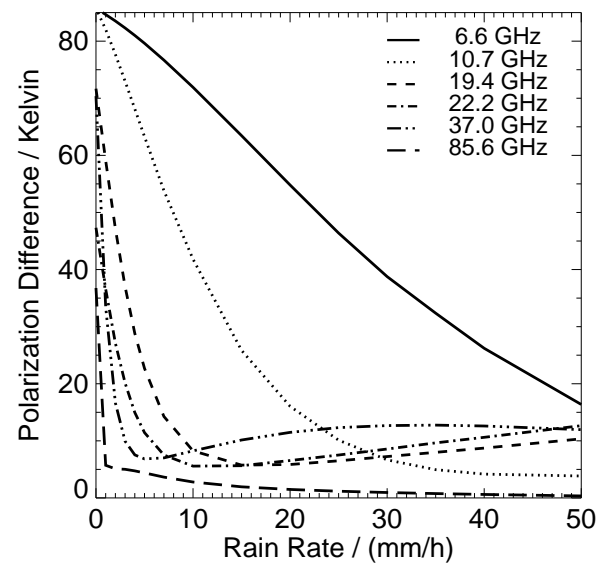


Figure 6.12: *Polarization difference versus rain rate over a calm water surface for the rain layer and Type-I ice particles (corresponding to the results of Fig. 6.8).*

of ocean PD with increasing opacity, only small amounts of PD are produced by the hydrometeors.

Using nonspherical rain and ice particles with size dependent aspect ratio (Fig. 6.12) gives larger PD especially for the low frequencies and 37 GHz, the 85 GHz PD remains small. With increased nonsphericity of the ice particles (Fig. 6.13 and Fig. 6.14) the maximum signal occurs at 37 and 85 GHz, but the general behaviour (position of the maximum, saturation with higher rain rates) depends very much on the aspect ratio. The 20 GHz frequencies also have an increase in PD (which does not saturate at high rain rates and therefore offers great potential for the remote sensing of heavy rain), but the form of the signal is much more similar to the results obtained with more spherical ice particles.

Since the ice particles above a rain event give only an indirect estimation of rain rate and the highest microwave frequencies show the highest sensitivity to particle shape (which itself is highly variable for ice particles and not well known), the rain retrieval with these frequencies will introduce yet unknown errors into the retrieval.

The low frequencies are more directly linked to the rain intensity and less affected by ice particle shapes. The shape of liquid hydrometeors can be given by models with a much better accuracy than that of ice particles. The information content of these channels will produce better retrieval results if an algorithm is specifically designed for this approach. Nonetheless the generally smaller sensitivity of the lower frequencies will make the retrieval problematic for low rain rates and inhomogeneous beamfilling. In addition, a main error source in the connection of modeled and measured radiances is the unknown vertical extent of the precipitation system. The low frequency regime is more sensitive to path integrated liquid water (clouds and precipitation), the high frequencies are better suited for the remote sensing of high cloud structures (mainly ice particles).

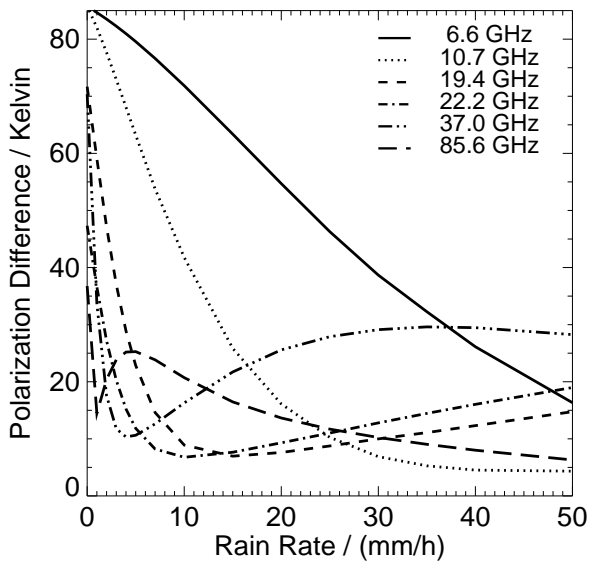


Figure 6.13: *Polarization difference versus rain rate over a calm water surface for the rain layer and Type-II ice particles (corresponding to the results of Fig. 6.9).*

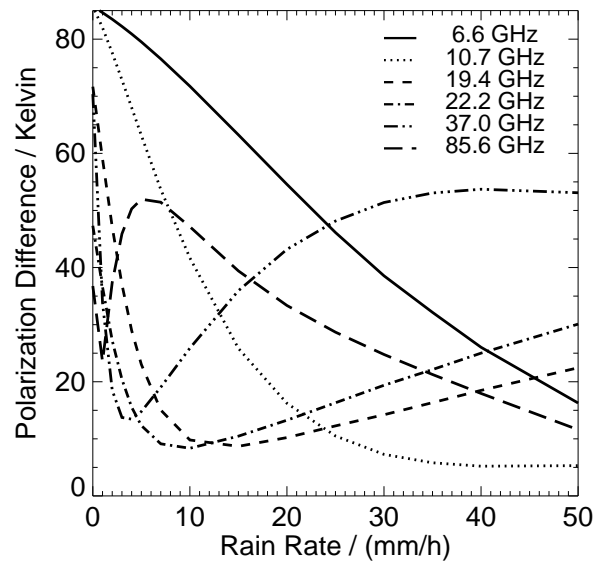


Figure 6.14: *Polarization difference versus rain rate over a calm water surface for the rain layer and Type-III ice particles (corresponding to the results of Fig. 6.10).*

Without additional information (for example from a radar) the conversion of brightness temperatures to surface rain rates is questionable.

### 6.2.3 Application to three-dimensional problems

The effect of particle shape in three-dimensional applications will depend on the distribution of radiation within the modeled scenario. Only in case of nearly horizontally homogeneous and isotropic conditions the results from one-dimensional calculations give an good estimate of the expected observations. The distribution of intensity with angle will then be similar to the one-dimensional case.

If there is a structure of broken clouds with clear air between clouds or even precipitation areas with significant amounts of liquid water, then these clouds will act as warm side-boundaries and induce a non-isotropic radiation field in horizontal direction (in contrast to the non-isotropic field in upward and downward directions for the one-dimensional case).

All previous investigations (Czekala, 1998; Czekala et al., 1999c) stated that the shape of scattering particles leads to large effects in side-scattering to back-scattering directions. This will be the case for horizontal non-isotropic radiation, but the precise effect is difficult to estimate. A three-dimensional model will ultimately be needed to solve this question. Furthermore, the averaging process of the field of view will affect the overall results. Since a large variety of atmospheric and surface conditions can be present in the field of view, the total result will be a mixture of many scenes. Decomposition will only be possible with additional information from other sensors.

# Chapter 7

## Summary

The influence of nonspherical hydrometeor shape on radiative transfer calculations in the microwave spectral range was investigated. For this purpose a polarized one-dimensional radiative transfer model was modified from spherical scattering to nonspherical scattering. The radiative transfer scheme had to be adjusted from scalar absorption and scattering cross sections to four-component angle dependent interaction parameters. Two single scattering models were combined with the radiative transfer model: The Extended Boundary Condition Method T-Matrix code from Mishchenko (*Mishchenko et al., 1996b*) and the Discretized Mie Formalism from *Rother and Schmidt (1996)*.

Model calculation were performed with the extended radiative transfer model to assess the effect of particle shape. The shape of liquid drops was chosen according to simulated equilibrium raindrop shapes from a dynamical model. The rotationally symmetric drops were aligned with their axis along the vertical. The resulting brightness temperatures and polarization differences were compared to control results obtained by spherical particles.

In case of nonspherical rain the averaged (vertical and horizontal polarization) brightness temperature is very similar to the one obtained by spherical particles. The brightness temperature depression due to ice particle scattering, however, shows a larger sensitivity to particle shape, especially at frequencies above 85 GHz.

The main difference is found in the polarization results. Nonspherical particles lead generally to higher positive polarization differences for upwelling radiation. The downwelling radiation shows a complex behaviour depending on frequency, rain rate and observation angle. Negative polarization differences may occur in certain ground-based observing geometries. This feature is completely different from effects of spherical particles.

Detailed analysis of the polarization signal with respect to the state of the atmosphere and the observation geometry showed that the shape of the particles only becomes important if the angular distribution of radiation within the atmosphere is non-isotropic. A high contrast between radiation propagating in a specific direction and its counterdirection produces the negative polarization feature for downwelling radiation. Such non-isotropic radiation fields can be found in transparent or semi-transparent atmospheres with differing boundary conditions (warm surface below, cold space above the atmosphere) and atmospheres with a gradient in optical thickness. If the gradient in the optical thickness is too steep (for example above a high reaching rain column and its cloud layer with se-

vere rain rates), then the radiation is nearly isotropic in the vicinity of the hydrometeors and to a high degree non-isotropic outside the region with hydrometeors. The thin layer at the cloud boundary produces only a small scattering signal.

As a consequence, the high microwave frequencies (with their larger optical thickness) do not contain much information about the scattering particles inside the cloud and rain layer, thus they are also less affected by the nonsphericity than lower frequencies. Microwave radiation below 20 GHz is able to pass a raining atmosphere without being totally blocked, thus the information content due to scattering by rain may help for the rain retrieval.

Groundbased observations with a 19 GHz radiometer were used to validate the model calculations. Data taken from 60 days with rain events from all over a two year period show the predicted polarization signal behaviour of varying negative polarization difference with the total water content. Although the exact values were slightly overestimated by the model, the accordance of measured and modeled data proves that the assumption of oblate raindrop shape is well justified.

Based on the validation results a new method of liquid water path retrieval with polarimetric ground-based measurements was proposed. The scattering signature of nonspherical particles makes a discrimination of cloud and rain liquid water as independent variables possible.

The implications of the nonspherical hydrometeor shape on satellite rain retrieval algorithms are difficult to estimate. The 37 and 85 GHz channels of SSM/I for example show a high sensitivity to the aspect ratio of ice particles. If the particle shape is not known at the time of the retrieval, significant errors may occur. Again, the low frequencies are more directly linked to the precipitation and the better known rain drop shapes. However, the assumption of a one-dimensional atmosphere is even less valid for satellite observations than for ground-based measurements. Thus the one-dimensional model needs to be replaced by a fully polarized three-dimensional model. Such a model can be used to test the valid range of one-dimensional modeling for three-dimensional applications.

# Acknowledgments

I would like to thank Clemens Simmer for his interest in this study and his encouraging guidance throughout the whole project.

The work of Michael Mishchenko (NASA Goddard Institute for Space Studies) who made available the EBCM code and helped with his advice while merging this code into the radiative transfer model is gratefully acknowledged. I wish to thank Tom Rother and Karsten Schmidt (DLR Neustrelitz) for the permission to use the DMF code. The work of Stephan Havemann (DLR Neustrelitz) was essential for the combining of the DMF with the radiative transfer model.

Achim Hornbostel and Arno Schroth (DLR Oberpfaffenhofen) kindly provided the validation data which significantly improved the quality of the study.

I thank Peter Bauer, Jeff Haferman, Matthias Drusch, Susanne Crewell, Andreas Macke, Dietrich Feist and Grant Petty for many fruitful discussions on the areas of radiative transfer, remote sensing, and meteorology.

Dirk Meetschen and Ariane Thiele supported the data analysis during some stages of this study. Finally, I wish to thank all people who helped to improve the quality of the manuscript by careful proof-reading.

This work was supported by the Deutsche Forschungsgemeinschaft under Si 606/1-1 and 606/1-2.





# Bibliography

- Adler, R. F., G. F. Huffman, and P. R. Kehn, Global tropical rain rate estimates from microwave-adjusted geosynchronous IR data, *Remote Sensing Reviews*, 11, 125–152, 1994.
- Adler, R. F., A. J. Negri, P. Keen, and I. M. Hakkarinen, Estimation of monthly rainfall over Japan and surrounding waters from a combination of low-orbit microwave and geosynchronous IR data, *Journal of Applied Meteorology*, 32, 335–356, 1993.
- Akvilonov, A. G., A. E. Basharinov, A. K. Gorodetskii, A. S. Gurvich, M. S. Krilova, B. G. Kutuza, D. T. Matveev, and A. P. Orlov, Determination of meteorological parameters with measurements from the satellite Cosmos-384, *Izvestia Atmos. Oceanic Phys.*, 9, 187–189, 1973.
- Andsager, K., K. V. Beard, and N. F. Laird, Laboratory measurements of axis ratios for large raindrops, *Journal of the Atmospheric Sciences*, 1998, submitted.
- Asano, S. and G. Yamamoto, Light scattering by a spheroidal particle, *Applied Optics*, 14, 29–49, 1975.
- Barber, P. and C. Yeh, Scattering of electromagnetic waves by arbitrarily shaped dielectric bodies, *Applied Optics*, 14, 2864–2872, 1975.
- Basharinov, A. E., A. S. Gurvich, S. T. Yegorov, A. A. Kurskaya, D. T. Matveyev, and A. M. Shutko, *The results of microwave sounding of the earth's surface according to experimental data from the satellite Cosmos-243. Space Research XI*, Akademie-Verlag, 1971.
- Bauer, A., N. Jacquinet-Husson, and P. Rosenkranz, Spectroscopy and microwave radiative transfer in the clear atmosphere, in *Development of Radiative Transfer Models*, edited by C. Mätzler, pages 9–29, Institute of Applied Physics, University of Bern, Sidlerstr. 5, CH-3012 Bern, Switzerland, 1999.
- Bauer, P. and N. Grody, The potential of combining SSM/I and SSM/T2 measurements to improve the identification of snowcover and precipitation, *IEEE Transactions on Geoscience and Remote Sensing*, 33, 252–261, 1995.
- Bauer, P. and P. Schlüssel, Rainfall, total water, ice water, and water vapor over sea from polarized microwave simulations and Special Sensor Microwave/Imager data, *Journal of Geophysical Research*, 98, 20737–20759, 1993.

- Beard, K. V., Oscillation models for predicting raindrop axis and backscatter ratios, *Radio Science*, 19, 67–74, 1984.
- Beard, K. V. and C. Chuang, A new model for the equilibrium shape of raindrops, *Journal of the Atmospheric Sciences*, 44, 1509–1524, 1987.
- Beard, K. V. and A. Tokay, A field study of small raindrop oscillations, *Geophysical Research Letters*, 18, 2257–2260, 1991.
- Borysow, A. and L. Frommhold, Collision-induced rototranslational absorption spectra of  $N_2$ - $N_2$  pairs at temperatures from 50 to 300 K, *Astrophysical Journal*, 311, 1043–1057, 1986.
- Cavalieri, D. J., P. Gloersen, and W. J. Campbell, Determination of sea-ice parameters with the nimbus-7 smmr, *Journal of Geophysical Research*, 89, 5355–5369, 1984.
- Chandrasekhar, S., *Radiative transfer*, Dover Publications Inc., 1960, 393p.
- Chuang, C. and K. V. Beard, A numerical model for the equilibrium shape of electrified raindrops, *Journal of the Atmospheric Sciences*, 47, 1374–1389, 1990.
- Conner, M. D. and G. W. Petty, Validation and intercomparison of SSM/I rain-rate retrieval methods over the continental United States, *Journal of Applied Meteorology*, 37, 679–700, 1998.
- Crewell, S., G. Haase, U. Löhnert, H. Mebold, and C. Simmer, A ground based multi-sensor system for the remote sensing of clouds, *Physics and Chemistry of the Earth (B)*, 24, 207–211, 1999a.
- Crewell, S., U. Löhnert, and C. Simmer, Remote sensing of liquid water profiles using microwave radiometry, in *Remote sensing of cloud parameters: retrieval and validation*, Symposium Proceedings, pages 45–50, Delft University of Technology, P.O. Box 5031, 2600 GA Delft, The Netherlands, International Research Centre of Telecommunications-Transmission and Radar (IRCTR), 1999b.
- Czekala, H., Effects of ice particle shape and orientation on polarized microwave radiation for off-nadir problems, *Geophysical Research Letters*, 25, 1669–1672, 1998.
- Czekala, H., P. Bauer, D. Jones, F. Marzano, A. Tassa, L. Roberti, S. Englisch, P. Baptista, A. Mugnai, and C. Simmer, Clouds and precipitation, in *Development of Radiative Transfer Models*, edited by C. Mätzler, pages 36–68, Institute of Applied Physics, University of Bern, Sidlerstr. 5, CH-3012 Bern, Switzerland, 1999a.
- Czekala, H., S. Havemann, K. Schmidt, T. Rother, and C. Simmer, Comparison of microwave radiative transfer calculations obtained with three different approximations of hydrometeor shape, *Journal of Quantitative Spectroscopy and Radiative Transfer*, pages 545 – 558, 1999b.

- Czekala, H. and C. Simmer, Microwave radiative transfer with non-spherical precipitating hydrometeors, *Journal of Quantitative Spectroscopy and Radiative Transfer*, 60, 365–374, 1998.
- Czekala, H., C. Simmer, T. Rother, K. Schmidt, and S. Havemann, Microwave radiative transfer with nonspherical particles, in *Satellite Remote Sensing of Clouds and the Atmosphere II*, edited by J. D. Haigh, pages 174–185, Proceedings of SPIE Vol. 3220, 1998.
- Czekala, H., A. Thiele, A. Hornbostel, A. Schroth, and C. Simmer, Polarized microwave radiation from nonspherical cloud and precipitation particles, in *Remote sensing of cloud parameters: retrieval and validation*, Symposium Proceedings, pages 71–76, Delft University of Technology, P.O. Box 5031, 2600 GA Delft, The Netherlands, International Research Centre of Telecommunications-Transmission and Radar (IRCTR), 1999c.
- Deirmendjian, D., *Electromagnetic scattering on spherical polydispersions*, American Elsevier, 1969, 290p.
- Draine, B. T. and P. J. Flatau, Discrete dipole approximation for scattering calculations, *Journal of the Optical Society of America*, 11, 1491–1499, 1994.
- Eremin, J. A., N. V. Orlov, and V. I. Rozenberg, Electromagnetic scattering from single electrified raindrops, *Journal of Atmospheric and Terrestrial Physics*, 57, 141–149, 1995.
- Evans, K. F. and G. L. Stephens, Microwave radiative transfer through clouds composed of realistically shaped ice crystals. Part I: Single scattering properties, *Journal of the Atmospheric Sciences*, 52, 2041–2057, 1995a.
- Evans, K. F. and G. L. Stephens, Microwave radiative transfer through clouds composed of realistically shaped ice crystals. Part II: Remote sensing of ice clouds, *Journal of the Atmospheric Sciences*, 52, 2058–2072, 1995b.
- Evans, K. F. and J. Vivekanandan, Multiparameter radar and microwave radiative transfer modeling of nonspherical atmospheric ice particles, *IEEE Transactions on Geoscience and Remote Sensing*, 28, 423–437, 1990.
- Evans, K. F., S. J. Walter, A. J. Heymsfield, and M. N. Deeter, Modeling of submillimeter passive remote sensing of cirrus clouds, *Journal of Applied Meteorology*, 37, 184–205, 1998.
- Feist, D. G., *Analysis and simulation of atmospheric microwave spectra measured with a space borne limb-sounding instrument*, Ph.D. thesis, University of Berne, Berne, Switzerland, 1999.
- Feist, D. G. and N. Kämpfer, BEAM: A fast versatile model for atmospheric absorption coefficients from 0–1000 GHz, in *Microwave Remote Sensing of the Atmosphere and Environment*, edited by T. Hayasaka, D. L. Wu, Y.-Q. Jin, and J. shan Jiang, volume

3503 of *Proceedings of SPIE*, pages 301–312, Beijing, China, SPIE – The International Society for Optical Engineering, 1998.

Ferraro, R. R., N. C. Grody, and G. F. Marks, Effects of surface conditions on rain identification using the SSM/I, *Remote Sensing Reviews*, 11, 195–209, 1994.

Ferraro, R. R. and G. F. Marks, The development of SSM/I rainrate retrieval algorithms using ground-based radar measurements, *Journal of Atmosphere and Ocean Technology*, 12, 755–764, 1995.

Ferraro, R. R., F. Weng, N. C. Grody, and A. Basist, An eight year (1987-1994) time series of rainfall, clouds, water vapor, snow cover, and sea-ice derived from SSM/I measurements, *Bulletin of the American Meteorological Society*, 77, 891–905, 1996.

Ferriday, J. G. and S. K. Avery, Passive microwave remote sensing of rainfall with SSM/I: Algorithm development and implementation, *Journal of Applied Meteorology*, 33, 1587–1596, 1994.

Flatau, P. J., K. A. Fuller, and D. W. Mackowski, Scattering by two spheres in contact: Comparisons between discrete-dipole approximation and modal analysis, *Applied Optics*, 32, 3302–3305, 1993.

Fournier, G. R. and B. T. N. Evans, Bridging the gap between the Rayleigh and Thompson limits for spheres and spheroids, *Applied Optics*, 32, 6159–6166, 1993.

Fuhrhop, R., T. C. Grenfell, G. Heygster, K.-P. Johnson, P. Schlüssel, M. Schrader, and C. Simmer, A combined radiative transfer model for sea-ice, free ocean and atmosphere, *Radio Science*, 33, 303–316, 1998.

Fuhrhop, R. and C. Simmer, SSM/I brightness temperature corrections for incidence angle variations, *Journal of Atmosphere and Ocean Technology*, 13, 246–254, 1996.

Gloersen, P. and F. T. Barath, A scanning multichannel microwave radiometer for nimbus-g and seasat-a, *IEEE Journal of Oceanic Engineering*, OE-2, 172–178, 1977.

Grody, N. C., Classification of snow cover and precipitation using the Special Sensor Microwave Imager, *Journal of Geophysical Research*, 96, 7423–7435, 1991.

Haferman, J. L., Microwave Scattering by Precipitation (Chapter 18), in *Light Scattering by Nonspherical Particles: Theory, Measurements, and Geophysical Applications*, edited by M. I. Mishchenko, J. W. Hovenier, and L. D. Travis, Academic Press, 1999, (in press).

Haferman, J. L., E. N. Anagnostou, D. Tsintikidis, W. F. Krajewski, and T. F. Smith, Physically based satellite retrieval of precipitation using a 3D passive microwave radiative transfer model, *Journal of Atmosphere and Ocean Technology*, 13, 832–850, 1996.

- Haferman, J. L., T. F. Smith, and W. F. Krajewski, A multi-dimensional discrete-ordinates method for polarized radiative transfer. Part I: Validation for randomly oriented axisymmetric particles, *Journal of Quantitative Spectroscopy and Radiative Transfer*, 58, 379–398, 1997.
- Heymsfield, G. M. and R. Fulton, Passive microwave and infrared structure of mesoscale convective systems, *Meteorology and Atmospheric Physics*, 54, 123–139, 1994.
- Hollinger, J. P. and coord., SSM/I instrument evaluation, *IEEE Transactions on Geoscience and Remote Sensing*, 28, 781–790, 1990.
- Hollinger, J. P., R. Lo, G. Poe, R. Savage, and J. Peirce, Special sensor microwave/imager user's guide, Technical report, Naval Research Laboratory, 1987.
- Hornbostel, A. and A. Schroth, Determination of propagation parameters by Olympus beacon, rain rate, radiometer, and radar measurements, *Frequenz*, 49, 224–231, 1995.
- Hornbostel, A., A. Schroth, and B. G. Kutuza, Polarimetric measurements and model calculations of downwelling rain brightness temperatures, in *Microwave Radiometry and Remote Sensing of the Environment*, edited by D. Solimini, pages 242–252, Zeist, The Netherlands, VSP Press, 1995.
- Jaquinet-Husson, N., N. A. Scott, A. Chedin, B. Bonnet, A. Barbe, V. G. Tyuterev, J. P. Champion, M. Winnewisser, L. R. Brown, R. Gamache, V. F. Golovko, and A. Chursin, The GEISA system in 1996: Toward an operational tool for the second generation vertical sounders radiance simulation, *Journal of Quantitative Spectroscopy and Radiative Transfer*, 59, 511–527, 1998.
- Karstens, U., C. Simmer, and E. Ruprecht, Remote sensing of cloud liquid water content, *Meteorology and Atmospheric Physics*, 54, 157–171, 1994.
- Liebe, H. J., Modelling attenuation and phase of radio waves in air at frequencies below 1000 GHz, *Radio Science*, 16, 1183–1199, 1981.
- Liebe, H. J., An updated model for millimeter wave propagation in moist air, *Radio Science*, 20, 1069–1089, 1985.
- Liebe, H. J., G. A. Hufford, and M. G. Cotton, Propagation modeling of moist air and suspended water/ice particles at frequencies below 1000 GHz., in *AGARD 52nd Specialists Meeting of the Electromagnetic Wave Propagation Panel, Palma de Mallorca, Spain*, 1993.
- Liebe, H. J. and D. H. Layton, Millimeter-wave properties of the atmosphere: Laboratory studies and propagation modelling, Technical Report 87224, U.S. Dept. of Commerce, National Telecommunications and Information Administration, Institute for Communication Sciences, 1987, 80p.
- Liou, K.-N., *An Introduction to Atmospheric Radiation*, Academic Press, 1980, 392p.

- Liu, Q. and C. Simmer, Polarisation and intensity in microwave radiative transfer, *Beiträge zur Physik der Atmosphäre*, 69, 535–545, 1996.
- Liu, Q., C. Simmer, and E. Ruprecht, A general analytical expression of the radiation source function for emitting and scattering media within the matrix operator method, *Beiträge zur Physik der Atmosphäre*, 64, 73–82, 1991.
- Liu, Q., C. Simmer, and E. Ruprecht, Three-dimensional radiative transfer effects of clouds in the microwave spectral range, *Journal of Geophysical Research*, 101, 4289–4298, 1996.
- Liu, Q., C. Simmer, and E. Ruprecht, Monte Carlo simulations of the microwave emissivity of the sea surface, *Journal of Geophysical Research*, 103, 24983–24989, 1998.
- Löhnert, U., S. Crewell, and C. Simmer, Combining a cloud radar, a passive microwave radiometer and a cloud model to obtain cloud liquid water, in *Remote sensing of cloud parameters: retrieval and validation*, Symposium Proceedings, pages 101–106, Delft University of Technology, P.O. Box 5031, 2600 GA Delft, The Netherlands, International Research Centre of Telecommunications-Transmission and Radar (IRCTR), 1999.
- Macke, A., J. Mueller, and E. Raschke, Single scattering properties of atmospheric ice crystals, *Journal of the Atmospheric Sciences*, 53, 2813–2825, 1996.
- Marshall, J. S. and W. Palmer, The distribution of raindrops with size, *J. Meteorol.*, 5, 165–166, 1948.
- Matsumura, M. and M. Seki, Extinction and polarization by ellipsoidal particles in the infrared, *Astrophysical Journal*, 456, 557–565, 1996.
- Mätzler, C., editor, *Development of Radiative Transfer Models*, Institute of Applied Physics, University of Bern, Sidlerstr. 5, CH-3012 Bern, Switzerland, COST 712: Application of Microwave Radiometry to Atmospheric Research and Monitoring, 1999, 154p.
- Mie, G., Beiträge zur Optik trüber Medien, speziell kolloidaler Metallösungen, *Annalen der Physik*, 25, 377–445, 1908.
- Mishchenko, M. I., Light scattering by size-shape distributions of randomly oriented axially symmetric particles of a size comparable to a wavelength, *Applied Optics*, 32, 4652–4666, 1993.
- Mishchenko, M. I. and L. D. Travis, Light scattering by polydisperse, rotationally symmetric nonspherical particles: Linear polarisation, *Journal of Quantitative Spectroscopy and Radiative Transfer*, 51, 579–778, 1994.
- Mishchenko, M. I., L. D. Travis, and A. Macke, Scattering of light by polydisperse, randomly oriented, finite circular cylinders, *Applied Optics*, 35, 4927–4940, 1996a.

- Mishchenko, M. I., L. D. Travis, and D. W. Mackowski, T-matrix computations of light scattering by nonspherical particles: A review, *Journal of Quantitative Spectroscopy and Radiative Transfer*, 55, 535–575, 1996b.
- Mugnai, A. and W. J. Wiscombe, Scattering from nonspherical chebyshev particles. I: cross sections, single-scattering albedo, asymmetry factor, and backscattered fraction, *Applied Optics*, 25, 1235–1244, 1986.
- Müller, G., Rain detection with the SSM/I in the BALTEX area, in *International BALTEX secretariat publication no 8*, pages 69–76, 1997.
- Oguchi, T., Attenuation of electromagnetic wave due to rain with distorted raindrops, *Journal of Radio Research Laboratories*, 7, 467–485, 1960.
- Oguchi, T., Attenuation of electromagnetic wave due to rain with distorted raindrops (part II), *Journal of Radio Research Laboratories*, 11, 19–44, 1964.
- Oguchi, T. and Y. Hosoya, Scattering properties of oblate raindrops and cross-polarization of radio waves due to rain (part II): Calculations at microwave and millimeter wave regions, *Journal of the Radio Research Laboratories (Japan)*, 21, 191–259, 1974.
- Petty, G., Physical retrievals of over-ocean rain rate from multichannel microwave imagery. Part I: Theoretical characteristics of normalized polarization and scattering indices, *Meteorology and Atmospheric Physics*, 54, 79–99, 1994.
- Pol, S. L. C., C. S. Ruf, and S. J. Keihm, Improved 20- to 32 ghz atmospheric absorption model, *Radio Science*, 33, 1319–1333, 1998.
- Prabhakara, C., G. Dalu, R. Sushanisi, J. J. Nucciarone, and G. L. Liberti, Rainfall over oceans: Remote sensing from satellite microwave radiometers, *Meteorology and Atmospheric Physics*, 47, 177–199, 1992.
- Prabhakara, C., D. A. Short, W. Wiscombe, R. S. Fraser, and B. E. Vollmer, Rainfall over oceans inferred from Nimbus-7 SMMR: Application to 1982-83 El Nino, *Journal of Climate and Applied Meteorology*, 25, 1464–1474, 1986.
- Pruppacher, H. R. and K. V. Beard, A wind tunnel investigation of the internal circulation and shape of water drops falling at terminal velocity in air, *Quarterly Journal of the Royal Meteorological Society*, 96, 247–256, 1970.
- Pruppacher, H. R. and R. L. Pitter, A semi-empirical determination of the shape of cloud and rain drops, *Journal of the Atmospheric Sciences*, 28, 86–94, 1971.
- Reburn, W. J., R. Siddans, B. J. Kerridge, S. Bühler, A. von Engel, K. Künzi, J. Urban, J. Wohlgemuth, D. Feist, N. Kämpfer, and H. Czekala, Study on upper troposphere/lower stratosphere sounding: Final report., Technical report, European Space Agency, ESA-ESTEC, 1998, ESA Contract No.: 12053/97/NL/CN, 569 pp.

- Roberti, L., Monte Carlo radiative transfer in the microwave and in the visible: Biasing techniques, *Applied Optics*, 36, 7929–7938, 1997.
- Roberti, L., J. Haferman, and C. Kummerow, Microwave radiative transfer through horizontally inhomogeneous precipitating clouds, *Journal of Geophysical Research*, 99, 16707–16718, 1994.
- Roberti, L. and C. Kummerow, Monte Carlo calculations of polarized microwave radiation emerging from cloud structures, *Journal of Geophysical Research*, 104, 2093–2104, 1999.
- Rodgers, C. D., Characterization and error analysis of profiles retrieved from remote sounding measurements, *Journal of Geophysical Research*, 95, 5587–5595, 1990.
- Rodgers, E., H. Siddalingaiah, A. T. C. Chang, and T. T. Wilheit, A statistical technique for determining rainfall over land employing Nimbus-6 ESMR measurements, *Journal of Applied Meteorology*, 18, 978–991, 1979.
- Rosenkranz, P. W., Water vapour microwave continuum absorption: A comparison of measurements and models, *Radio Science*, 33, 919–928, 1998.
- Rother, T., Generalization of the separation of variables method for nonspherical scattering on dielectric objects, *Journal of Quantitative Spectroscopy and Radiative Transfer*, 60, 335–353, 1998.
- Rother, T. and K. Schmidt, The discrete Mie-formalism for plane-wave scattering on axisymmetric particles, *Journal of Electromagnetic Waves and Applications*, 10, 273–297, 1996.
- Rother, T. and K. Schmidt, The discretized Mie-formalism for electromagnetic scattering, in *Progress in Electromagnetic Research, PIER 17*, edited by J. Kong, pages 91–183, EMV Publishing, Cambridge, Massachusetts, USA, 1997.
- Schrader, M., Ein Dreiskalenmodell zur Berechnung der Reflektivität der Ozeanoberfläche im Mikrowellenfrequenzbereich, *Berichte aus dem Institut für Meereskunde, Kiel*, 274, 1995, 118p.
- Simmer, C., *Satellitenfernerkundung hydrologischer Parameter der Atmosphäre mit Mikrowellen*, Verlag Dr. Kovac, 1994, 314p.
- Solheim, F., J. R. Godwin, E. R. Westwater, Y. Han, S. J. Keihm, K. Marsh, and R. Ware, Radiometric profiling of temperature, water vapor and cloud liquid water using various inversion methods, *Radio Science*, 33, 393–404, 1998.
- Spencer, R. W., H. M. Goodman, and R. E. Hood, Precipitation retrieval over land and ocean with SSM/I: Identification and characteristics of the scattering signal, *Journal of Atmosphere and Ocean Technology*, 6, 254–273, 1989.



- Spencer, R. W., B. B. Hinton, and W. S. Olson, Nimbus-7 37 GHz radiances correlated with radar rain rates over the Gulf of Mexico, *Journal of Climate and Applied Meteorology*, 22, 2095–2099, 1983a.
- Spencer, R. W., W. S. Olson, R. Wu, D. W. Martin, J. A. Weinman, and D. A. Santek, Heavy thunderstorms observed over land by the Nimbus-7 scanning multichannel microwave radiometer, *Journal of Climate and Applied Meteorology*, 22, 1041–1046, 1983b.
- Stogryn, A. P., C. T. Butler, and T. J. Bartolac, Ocean surface wind retrievals from special sensor microwave imager data with neural networks, *Journal of Geophysical Research*, 99, 981–984, 1994.
- Tsang, L., J. A. Kong, and R. T. Shin, *Theory of Microwave Remote Sensing*, John Wiley & Sons, 1985, 613p.
- Turk, J. and J. Vivekanandan, Effects of hydrometeor shape and orientation upon passive microwave brightness temperature measurements, in *Microwave Radiometry and Remote Sensing of the Environment*, edited by D. Solimini, pages 187–196, Zeist, The Netherlands, VSP Press, 1995.
- Ulaby, F. T., R. K. Moore, and A. K. Fung, *Microwave Remote Sensing, Active and Passive*, volume 1, Addison-Wesley, 1981, 456p.
- Ulaby, F. T., R. K. Moore, and A. K. Fung, *Microwave Remote Sensing, Active and Passive*, volume 3, Addison-Wesley, 1986, 1098p.
- van de Hulst, H. C., *Light Scattering by Small Particles*, Dover Publications, 1981, 470p.
- Waterman, P. C., Symmetry, unitarity, and geometry in electromagnetic scattering, *Physical Review D*, 3, 825–839, 1971.
- Westwater, E. R., The accuracy of water vapor and cloud liquid water determination by dual-frequency ground-based microwave radiometry., *Radio Science*, 13, 677–685, 1978.
- Wilheit, T. T. and A. T. C. Chang, An algorithm for retrieval of ocean surface and atmospheric parameters from the observations of the scanning multichannel microwave radiometer, *Radio Science*, 15, 525–544, 1980.
- Wilheit, T. T., A. T. C. Chang, M. S. V. Rao, E. B. Rodgers, and J. S. Theon, A satellite technique for quantitatively mapping rainfall rates over the oceans, *Journal of Applied Meteorology*, 16, 551–560, 1977.
- Wu, R. and J. A. Weinman, Microwave radiances from precipitating clouds containing aspherical ice, combined phase, and liquid hydrometeors, *Journal of Geophysical Research*, 89, 7170–7178, 1984.



# Curriculum Vitae

Name : Harald Czekala  
Date of Birth : February 3, 1969 in Hamburg, Germany  
Nationality : German  
Marital status : unmarried

## Education:

1975 – 1979 Elementary school, Kiel  
1979 – 1988 Secondary school, Kiel  
06/1988 Graduation of secondary school (Abitur), Kiel  
07/1988 – 09/1989 Military service in the German Navy on board a minesweeping vessel  
10/1989 – 08/1995 Study of Physics, Christian-Albrechts-Universität zu Kiel  
08/1995 Physicist (Diplom Physiker, German equivalent to M.Sc.)

## Employment record:

03/1992 – 08/1995 Student Research Assistant  
Institute for Marine Research (IfM), University of Kiel  
12/1995 – 03/1996 Assistent Research Scientist, IfM Kiel  
04/1996 – present Assistent Research Scientist,  
Meteorological Institute, University of Bonn

# Lebenslauf

Name : Harald Czekala  
Geburtstag : 03.02. 1969 in Hamburg  
Nationalität : Deutsch  
Familienstand : unverheiratet

## Ausbildung:

1975 – 1979 Grundschule Fritz-Reuter-Schule, Kiel  
1979 – 1988 Gymnasium Hebbelschule, Kiel  
06/1988 Abitur  
07/1988 – 09/1989 Grundwehrdienst an Bord eines Minensuchbootes bei der Marine  
10/1989 – 08/1995 Studium der Physik, Christian-Albrechts-Universität zu Kiel  
08/1995 Diplom Physiker

## Tätigkeiten:

03/1992 – 08/1995 Studentische Hilfskraft am  
Institut für Meereskunde (IfM), Universität Kiel  
12/1995 – 03/1996 Wissenschaftlicher Mitarbeiter, IfM Kiel  
seit 04/1996 Wissenschaftlicher Mitarbeiter,  
Meteorologisches Institut der Universität Bonn

